STRUCTURE AND PROPERTY RELATIONSHIPS OF AMORPHOUS POROUS MATERIALS

A Dissertation

by

GREGORY STEVEN DAY

Submitted to the Office of Graduate Studies of
Texas A&M University
In partial fulfillment of the requirements for the degree of

DOCTOR OF PHILOSOPHY

Chair of Committee	Hong-Cai Joe Zhou
Committee Members,	Michael Nippe
	Donald J. Darensbourg
	Melissa A. Grunlan
Head of Department,	Simon W. North

August 2020

Major Subject: Chemistry

ABSTRACT

While highly crystalline porous materials, such as metal-organic frameworks (MOFs), have been heavily studied, their amorphous counterparts have not. This is mainly due to the controllable structures and ease of characterization for crystalline materials, neither of which are typically available for amorphous material. However, despite their difficult characterization, amorphous materials have many potential benefits, particularly related to their combination of high potential stability and tunability. In this work, I focused in on two families of amorphous materials, porous polymer networks (PPNs), and MOF-derived carbons (MOFdCs). I attempted to elucidate ways in which these materials can be analyzed, and how, despite their amorphous nature, they can be tuned for different properties. In the first project, I describe a method of improving the CO_2 cycling performance of an amorphous PPN based material through the incorporation of functionalized dopant molecules. In particular, I found that through the incorporation of the hydroxyl-containing cyanuric acid, which can engage in hydrogen bonding interactions with the loaded active amine species, I could achieve improved CO_2 cycling capacity (<4% loss in uptake performance) over 30 cycles. In addition, through *in situ* IR spectroscopy, it was shown that this PPN, PPN-151-DETA, engages in a stronger chemisorptive mechanism relative to the non-cyanuric acid doped material. In the second project, I investigated the effect of the gas environment on the calcination of an iron-based MOF, PCN-250, to produce a MOFdC. I showed that the resulting iron oxide phase and level of porosity are both dependent on the particular gas environment during calcination.

In addition, I showed it was possible to investigate the structure of the porous carbon through neutron total scattering and pair distribution (PDF) methodologies, indicating that the residual carbon exists in the graphitic phase. This work was continued in the final project, wherein I investigated both a Zn (Zn-MOF-74) and Zr (UiO-66) based MOF under variable temperature calcination. Neutron total scattering again showed the presence of graphitic carbon, with the degree of structural order in the graphitic phase being dependent on the temperature of calcination. Finally, I showed that the cubic zirconium cluster in UiO-66 was able to act as a template for the formation of higher-order zirconia phases in the resulting carbon. These projects all show the potential that amorphous materials have for unique properties and gives insight into some of the structural features of this often-neglected class of materials.

DEDICATION

This thesis is dedicated to all the future graduate students who worry that they are not good enough, never give up, never surrender.

ACKNOWLEDGMENTS

First and foremost, I would like to acknowledge my fiancé Xuan Ye, as without her support, I doubt I would be in the position to write this thesis. I would also like to acknowledge my parents, Steven and Jean Day, my sister and brother-in-law, Katherine and Brewster Thackeray, and all of my extended friends and family, you all always asked "so, when do you graduate?" I am glad to say I finally have an answer for you.

None of the work here would be possible without the support of my academic and research advisors, Professor Hong-Cai Joe Zhou of Texas A&M University, Dr. Matthew R. Ryder of Oak Ridge National Laboratory, as well as Professor Katharine Page of the University of Tennessee at Knoxville. Their support and guidance were instrumental in conducting my research and achieving the successes that I have. In addition, I would like to thank Professors Michael Nippe, Donald Darensbourg, and Melissa Grunlan for their assistance in guiding my progress through the academic system.

There are a number of collaborators who have been a great influence on both my academic work as well as my growth as a person. I would like to specifically thank Zac Perry for all of his guidance in research, and all of the strange philosophical conversations we would get into, Hannah F. Drake, Elizabeth A. Joseph, Christina T. Lollar, and Zhifeng "Sean" Xiao for being great sounding boards for ideas and putting up with my awful jokes, and Aida Contreras-Ramirez for being a great post-doc and perhaps the most Lawful Good person I've ever met. Carrie Frederiksen has been the glue that holds our research group together, none of this would be possible without her help. I would also like to thank Dr.

Edward Lee and all of the staff of the chemistry first year program, I taught CHEM 117 for several years, and they always tried to make the experience worthwhile while keeping the demands on the graduate students as low as possible. That support has enabled many a graduate student to successfully juggle the teaching/research balance, and I am forever grateful for that.

A number of collaborators and funding agencies need to be acknowledged. Thank you to Jason Ornstein, Ray Ozdemir, Anne Boehme, and Carlos Hurriel Ybanez Jr. of *framergy*, we worked together on several projects, and I thank you for all the help you gave. I would additionally like to thank Professor Simon Billinge and his student Songsheng Tao for getting me interested in pair distribution function analysis, which I was able to really jump into at Oak Ridge National Laboratory. I would also like to give a massive thanks to the Department of Energy Office of Science for their SCGSR fellowship program, which gave me the opportunity to work with Oak Ridge National Laboratory. I've had the pleasure to work with a number of organizations on campus on various projects, and while naming everyone would fill up several pages I'd like to at least mention: Professors Barbara Gastel, Jonathan Coopersmith, Dr. Jorja Kimball, and Krisa Camargo and all the members of A-STEP (Aggies in Science Technology and Engineering Policy) who instilled in me an interest in not just doing good science, but to try and reach out beyond the lab and inform the public about science and try to make the world a better place. I would like to thank Dr. Marty Lail and Dr. Mustapha Soukri of RTI International for helping us out on a number of project proposals, hopefully we'll have better luck next time. Professor Charlie Culp for telling me more than I ever thought I'd learn about air

conditioning, and Professor Xiaofeng Qian for giving me and Zac Perry that 2 hour lecture on non-linear optics in your office, let's keep working on that NLO MOF.

I would be remiss if I did not name the following people for their help: Liang Feng, Kunyu Wang, Mathieu Bosch, Sayan Banerjee, Jialuo Li, Jeremy Willman, and all of the countless other members of the Zhou group for their help, the talented group of undergraduates I've had the pleasure of working with: Valentin Carretier, Haley Baker, Connor McNellis, Liam McCormick, Hanwen Cui, Eric Imhoff, and Dillon Richards of TAMU, as well as Rochelle Stilles and Thomas Siggillino at ORNL, my outside collaborators Kui Tan (UT Dallas), Haiyan Mao (UC Berkeley), Peter Metz (ORNL), Stephen Purdy (ORNL), Bo Jiang (ORNL), and Michelle Everett (ORNL), and finally some of the TAMU user facilities, particularly Dr. Yordanos Bisrat (MCF), Dr. Vladimir Bakhmutov (Chemistry department NMR lab), and Dr. Nat Bhuvanesh (Chemistry department X-ray lab).

Finally, I would like to thank whoever you are for taking the time to read this, I hope you enjoy my thesis!

CONTRIBUTORS AND FUNDING SOURCES

Contributors

This work was supervised by a dissertation committee consisting of Professor Joe Zhou of the Department of Chemistry, Dr. Matthew R. Ryder of Oak Ridge National Laboratory, Professors Donald Darensbourg, and Michael Nippe of the Department of Chemistry, and Professor Melissa Grunlan of the Department of Mechanical Engineering.

The work in Chapter 2 was conducted as part of a team consisting of Hannah F. Drake, Elizabeth A. Joseph, Mathieu Bosch, Jeremy A. Willman, Valentin Carretier, Zachary Perry, William Burtner, and Sayan Banerjee from Texas A&M University under the supervision of Professor Hong-Cai Zhou, as well as Dr. Kui Tan of the University of Texas at Dallas and O. Koray Ozdemir of *framergy*. The student was lead author on this published manuscript and was involved in the collection and analysis of the data shown herein.

The work in Chapter 3 was conducted with the assistance of Jialuo Li (SEM/TEM), Elizabeth A. Joseph (collection of air-free samples), Zachary Perry (project design) of Texas A&M, Peter Metz (PDF and mPDF guidance) from Oak Ridge National Laboratory under the supervision of Dr. Matthew R. Ryder (Oak Ridge National Laboratory) Professor Katharine Page (Oak Ridge National Laboratory and the University of Tennessee at Knoxville) and Professor Hong-Cai Zhou (Texas A&M).

The work in Chapter 4 was conducted with the assistance of Hannah F. Drake (sample collection and analysis) Dr. Aida Contreras-Ramirez (TEM) at Texas A&M

University under the supervision of Professor Hong-Cai Zhou. The author (Gregory S. Day) was co-supervised on this project by Dr. Matthew R. Ryder, Professor Katharine Page, and Professor Hong-Cai Zhou.

Funding Sources

Graduate study was supported in part by a teaching assistantship from Texas A&M University. This work was supported as part of the Center for Gas Separations, an Energy Frontier Research Center funded by the U.S. Department of Energy, Office of Science, Basic Energy Sciences under Award # DESC0001015 (CO_2 separation, Chapter 2) by the Department of Energy Office of Fossil Energy, National Energy Technology Laboratory Award #DE-FE0026472 (CO_2 separation, Chapter 2). Additional support was provided by the Welch Foundation under grant A0030 (additional supplies and salary support). The author was additionally supported by the Department of Energy, Office of Science Graduate Student Research (SCGSR) Fellowship for work conducted at Oak Ridge National Laboratory (Chapter 3 and 4).

The contents of this document are solely the responsibility of the authors and do not necessarily represent the official views of the Department of Energy, or the Welch Foundation.

TABLE OF CONTENTS

Page

LIST OF FIGURES

Page

LIST OF TABLES

Page

CHAPTER I

INTRODUCTION AND LITERATURE REVIEW

Porous Carbons and the Early Days of Adsorption Science

The development of porous materials has long been of interest to the chemistry community, as the pores within these materials, whether micro, meso, or macropores, can be utilized for the adsorption and capture of molecular species. Some of the earliest uses of materials for their porous properties date back to circa 1500 BC, where medical practices in ancient Egypt used charcoal as described in the Ebers papyrus.[1] Early accounts of charcoal usage were mainly focused on treatments for indigestion. The practices described the consumption of mixtures containing Egpytian ink,[1] which in itself was typically formed from charcoal suspended gum arabic slurry.[2] The practical use of charcoal for its absorptive properties continued throughout antiquity and into the early modern era. Early Greek sources demonstrated the continued use of charcoal in medicinal applications, and documents from Hindu sources describe the use of charcoal for the purification of drinking water.[3] Even as late as the age of European exploration, there are descriptions of charring the interior of wooden barrels to improve the shelf life of potable water.[4] Indeed, the consumption of charcoal has even been observed in the animal kingdom, with theories suggesting that it is utilized for the adsorption of phenolic compounds, such as in the case of red Zanzibar Red Colobus Monkeys.[5] However, while there was significant practical knowledge related to the adsorptive effects of charcoal, these early applications showed little in the way of a fundamental understanding of the adsorptive properties inherent in the materials. The earliest scientific observation and

testing of the adsorption properties in porous materials, specifically gas adsorption, was described by Carl Scheele, an 18th century Swedish pharmacist, and chemist. Scheele observed that charcoal, upon heating in a vessel attached to a rubbery bladder, could expel adsorbed gasses, causing an expansion of the bladder to an amount much greater than that observed in the heating of a typical sealed vessel.[6] Upon subsequent cooling, Scheele observed the subsequent loss in volume of the bladder due to readsorption of the gas to the charcoal, with this process being heavily repeatable. While many of Scheele's conclusions are based upon outdated chemical principles such as phlogiston theory,[7] the basic observations he noted in his book do provide one of the key cornerstone experiments upon which future adsorption work was based.

While the study conducted by Scheele focused on the gas adsorption properties of this porous material, much of the subsequent work on activated charcoal focused on its abilities to act as a solid/liquid phase adsorbent. These charcoal adsorbents were characterized by their ability to remove impurities or pollutants from liquid streams, in processes highly similar to the ancient use of charcoal as a filtering agent. As the industrial age continued through the 18th and 19th centuries, there became a new need for advanced filtration and purification systems. In particular, the abundant availability of sugar from Caribbean plantations required excess refinement. This excess refinement was particularly necessary to eliminate the dark discoloration of the sugar caused by residual molasses.[8]

The initial breakthrough in the sugar decolorization processes came in 1785 when Tobias Lowitz succeeded in decolorizing tartaric acid through the use of charcoal.[9] As a result, by 1794, there were reportedly sugar refineries which were utilizing wood-based

charcoals for the decolorization of sugar.[10] However, the process was kept as a trade secret at the time. Even though this was widely used in this industry, early patents and publicized processes for sugar decolorization only appeared nearly two decades later, in 1812.[11] At the same time, there was also an increasing interest in the use of porous carbons for medical applications, specifically for the adsorption of ingested poisons.[12] Several oft-repeated, but poorly documented, anecdotes, describe attempts to showcase the anti-poison efficacy of charcoal, such as the ingestion of arsenic trioxide by Michel Bertrand in 1813 and the ingestion of strychnine by a Professor by the name of Touéry in either 1830[12] or 1852,[13] followed by charcoal. However, while these stunts provided much in the way of interesting stories to be shared, they did not provide much in the way of experimental data regarding the adsorption affinities or capacities of charcoal. By the late 19th century, the growing scientific knowledge of germ theory resulted in an increasing interest in the development of new methods and materials for the removal of pathogens from drinking water.[14] With pioneering work by Frederick Lipscombe showing that charcoal had applications in the adsorption and purification of drinking water,[15] there was a rush to commercialize carbon-based adsorptive materials for this application. However, not all of these materials were ideally suited for microbacterial separation.[14] This water purification data also paved the way for the study of charcoal as a general poison control system during the early 20th century.[12] Charcoal eventually made its way into the gas masks of World War I due to its improved adsorption capacity over the traditional cotton or fiber adsorbents used previously.[16] The efficacy of porous materials for the adsorption of gas and liquid phase poisons resulted in an increasing interest in charcoal for medical

applications. Due to its generally low cost and low toxicity, charcoal was highly prized over other adsorbents in the medical community.[17]

Zeolites

While porous charcoal had a long practical history of study, the limited avenues available to study adsorptive behavior, compounded by the poor structural characterization techniques available at the time, limited the use of charcoal in scientific pursuits beyond application-focused research. During the mid-18th century, while the initial scientific insights into the adsorptive properties of charcoal were still being investigated, a new class of porous minerals, the zeolites, were beginning to be studied. The word for Zeolites comes from a combination of the Greek words *zeo* (to boil) and *lithos* (stone).[18] The original zeolite materials, sometimes referred to as "natural zeolites" were aluminosilicate mineral derivatives that had highly ordered pores. These materials were discovered by Axel Fredrick Cronstedt, a Swedish mineralogist who also discovered elemental nickel.[19] In 1756, Cronstedt based his claims on two example specimens, one from a mine in Sweden, the other from an unknown source in Iceland.[20] During his analysis of these materials, Cronstedt observed that upon heating, the material seemed to produce steam. This sign we now recognize as the desorption of water from the zeolitic pores.[20] The materials investigated by Cronstedt have been traditionally thought to have been solely stilbite, although later analyses of samples from the same Swedish mine Cronstedt reported have suggested that the material used in his experiments mainly the zeolite stellerite with a small amount of stilbite.[21]

The discovery of these zeolite materials was somewhat fortuitous, as the synthesis of natural zeolites often requires very specific conditions. It is suspected that natural synthesis requires the use of volcanic glasses under sedimentary conditions and highly basic (>8.5, but often as high as 10) pHs, as well as high temperatures.[22-23] Poor control over this pH can readily result in the formation of clay materials, another class of aluminosilicates comprised of layered structures. While there are several reports of naturally synthesized zeolites, approximately 63 natural sources are known, only a handful of those are large enough deposits to be commercially viable. Most reported deposits are comprised of microscopic-sized crystals.[23-24] Despite their relative scarcity, the mineralogists from the 18th through the early 20th centuries produced a wide body of research regarding the potential applications of natural zeolites. The inherent porosity of zeolites were initially gleamed through scientific experiments related to their ability to act as molecular sieves. In this sense, a molecular sieve is any material that can preferentially adsorb molecular scale species through size selectivity.[18] Around this same time, the Bragg father and son duo (William Henry and William Lawrence) were developing their laws of X-ray diffraction as a means to investigate crystalline materials. Their initial structural determination experiments were conducted with a diamond in 1913.[25] Within 20 years of this discovery, there were already reports using this new structural determination technique to analyze zeolites. One of the earliest structural conformations of a porous material was conducted by Linus Pauling in 1930 when he investigated the single crystal diffraction of sodalite.[26]

While the formation mechanisms for certain zeolite derivatives and other silicates had been known for some time,[27] levyne or levynite zeolites were first synthesized in 1862 by Henri Sainte-Claire-Deville.[28] The work revolving around zeolites is fairly recent in comparison to charcoal porous materials as there was no major push for the large scale synthesis of zeolites before the 20th century. By the 1940s, there was enough data regarding both the adsorption properties,[29] as well as the synthesis of zeolites[30-31] to warrant interest form industrial research groups for the use of these materials as molecular sieves. In 1948 the Union Carbide company began their initial studies into zeolite synthesis under the direction of Robert M. Milton.[32] Many of the zeolite species that had been synthesized prior to this work were those typically described as "anhydrous" zeolites or species with low interstitial water content. These materials often had low porosity, which meant they were typically not seen as commercially viable. At the time, there was a general understanding in the geological community that natural anhydrous zeolites are formed at high temperatures (200-300 °C). In contrast, the more porous or "hydrated" zeolites were expected to be formed at lower temperatures. However, many of the zeolite syntheses that had been performed prior to the Union Carbide research had been synthesized at high temperatures due to the utilization of insoluble silica or alumina precursors.[30-31] Perhaps one of Milton's most important contributions to the synthesis of hydrous zeolites was the use of soluble precursor species, such sodium silicate and aluminate or alumina trihydrate, to produce the starting gel that could then easily crystalize at 100 °C.[32] These new procedures revolutionized the synthesis of zeolites. When these procedures were combined with the recent adaptation of powder X-ray diffraction (PXRD)

techniques, a new quick and easy characterization and screening procedure was established to study these materials.[32-33] These efforts resulted in the widespread adoption of zeolite derivatives, such as zeolite A[33] and zeolite Y,[34] in industrial processes for sieving and catalysis. Many of the applications for zeolite materials established by Milton's team continue in industrial processes to this day.[35]

Porous Silicas

Around the same time zeolites were first being synthesized at industrial scales, two other types of porous material were beginning to enter the chemical lexicon: porous silica and porous polymers. Porous silica mainly consists of two major species. The first being aerogels, which are characterized as having highly amorphous meso to macroporous solids with ultra-low bulk densities.[36] The second major species being mesoporous silicas which characteristically consist of an amorphous silica chemical system, but which oftentimes has a highly ordered pore environment.[37] The initial reports of silica aerogel formation actual predate the widespread adoption of synthetic zeolites,[38] with the oft-repeated story that Samuel Stevens Kistler developed the first aerogels as part of a bet with Charles Learned.[39] Aerogels, made from silica or other simple element oxides,[40] despite their early start, did not take off for academic research efforts until the 1970s. This may mainly have been due to the difficult synthetic requirements of aerogels. These materials have low bulk density frameworks and typically require supercritical drying to avoid pore collapse during solvent removal. Like amorphous charcoals before it, the lack of large-scale structural order in these materials has generally limited their use in fundamental studies, with much of the research in aerogels focusing on their practical application. Some of the

earliest work reported for silica aerogels was for their use as Cherenkov radiators due to their low and tunable refractive index.[41] Aerogel science did not truly take off until its introduction as potential insulating materials. Their low bulk densities, combined with their air filled pores that are typically smaller than the mean free path of air, resulted in a severe loss of thermal conductivity.[42] Unfortunately, due to the difficult synthesis required to produce these materials, aerogels are still mainly utilized in niche applications. In particular, space exploration, where the limiting factor for cost is typically the mass of the material being sent to space, has seen extensive use of aerogel materials due to their very low bulk density.[43] In NASA's Stardust mission, a probe containing gradient density silica aerogel blocks was used to collect residue from a comet.[44] The outer layer of the aerogel was of a low density, thus allowing the probe to slow down the incoming comet dust. The dust collection was further isolated and stored by a denser inner aerogel layer. Silica aerogels have also found uses in space exploration insulation, with many of the Mars rovers containing silica aerogel insulation to deal with the ~100 °C temperature gradients common on the Martian surface.[43, 45] While silica aerogels have found strong potentials in niche applications such as space exploration, their poorly defined structures and difficult syntheses have generally resulted in limited terrestrial applications or study.

In contrast to aerogels, mesoporous silicas have been utilized in industrial applications for many years, in particular as catalyst supports.[46] The amorphous nature of these materials has oftentimes precluded them from all but the most basic of sieving or separation testing, such as in column chromatography. Ordered mesoporous materials such as MCM-41 (MCM = Mobile Composition of Matter)[47] or SBA-15 (SBA = Santa

Barbara Amorphous)[48] were initially developed in the 1990s with the main goal in mind: produce materials that can break through the traditional pore size limits of zeolites (~2 nm) while taking advantage of the robust chemical benefits of silica materials for chemical support and separation processes.[49] Both of these materials are mainly known for their ordered pore structures, with well-defined hexagonal channels arranged in an ordered manner. In many ways, the generation of these ordered channels and pores takes advantage of similar formation mechanisms to that of zeolites: using a templated approach. This template approach utilizes interstitial either cations and water, for zeolites and micelles (MCM-41), or soluble polymers (SBA-15), to produce ordered mesoporous silica structure. These materials have thus been shown to have many similar applications as those of zeolites, but they utilize their larger pore sizes to work with specific specialized systems, such as in biomolecule capture[50] or catalytic oligomer formation.[51] Many applications for mesoporous silicas are those that cannot be readily performed with zeolites. The larger pores, combined with their improved structural ordering as compared to standard silica gel materials, have made mesoporous silicas of particular interest for the study of the confinement effects in mesoporous materials. The features that make mesoporous silicas so effective for this approach is that they eliminate potential data broadening from disordered systems.[52-53]

These three classic materials, porous carbons or charcoals, zeolites, and silicas, are all noteworthy due to either being based on naturally occurring materials (carbons, zeolites), or by being synthesized from common materials, with a focus on simple, atom economically efficient processes (carbons, zeolites, and silicas). In general, the local

chemical environments of these materials are fairly homogeneous, being either simple mono or di-elemental frameworks. These features, which typically make these materials relatively simple to design or synthesize, often result in a limited chemical tunability of the framework. In the quest for enhanced tunability within porous materials, there has thus been a push towards more advanced, chemically distinct, and functional advantageous porous materials. These efforts, which, although they can trace their roots to the rapid expansion in chemical and materials research in the latter half of the 20th century, have only really started taking off in the last 20 to 30 years.[54-55] These new classes of functionalized porous materials consist of species such as porous polymer networks (PPNs), metal-organic frameworks (MOFs), covalent-organic frameworks (COFs), hydrogen-bonded organic Frameworks (HOFs), metal-organic cages (MOCs), organic cages, and many other new and up-and-coming materials represent a distinct paradigm shift in the design of porous materials towards functionality and tunability of scaffold structures.

Porous Polymer Networks

Porous polymers, also called porous polymer networks (PPNs)[56] or porous organic polymers (POPs)[57] to distinguish them from other repeating unit based porous materials, are typically characterized by their high structural stability due to their covalent framework nature. However, these materials have low thermal stability due to the ease of oxidation of the carbon based framework. Porous polymers have been known since at least the late 1940s.[58] Some of the earliest examples of PPNs were based on non-intrinsically porous polymeric systems such as polystyrenes or sulfonated polystyrenes.[59] These initial

materials typically had limited structural ordering as they were typically made porous through their processing steps, not through inherent porosity.[60] While some samples could be produced with relatively ordered levels of porosity, typically through the use of templating materials known as porogens,[61] both the structural components and the porosity tended to be amorphous. As such, these materials were mainly studied in application-oriented research and were relatively quickly commercialized for processes such as ion exchange and various kinds of chromatography, such as gel permeation chromatography.

One area where porous polymers have traditionally found uses is in the field of membrane systems.[62] One of the earliest practical uses of polymer membranes was in the development of the reverse osmosis process in the 1950s.[63] Reverse osmosis is a process wherein water passes through a membrane while dissolved species in the water, such as organic molecules, cations, or anions, do not. The process is called "reverse" osmosis because there is a transport of water from an area of high solute concentration to an area of low solute concentration, which is the reverse of standard biological osmosis.[64] Reverse osmosis was first formalized in the 1950s by Gerald Hassler, although not published until 1960.[63, 65] Hassler's initial designs, made of mixed ceramic and polymeric (typically cellulose-based) membranes, had relatively low water fluxes, making them limited in regard for practical water purification. It was not until a few years later when Sydney Loeb and Srinivasa Sourirajan developed their magnesium perchlorate treated cellulose acetate membrane, that practical membrane-based reverse osmosis systems became viable. Since then, these materials have been heavily commercialized, and are used in everything from water purification to beer brewing, to kidney dialysis. Despite the significant amount of

time since Loeb and Sourirajan's development of the first commercially viable reverse osmosis system, modern reverse osmosis systems still operate in much the same manner. The polymer membranes are now mostly polyamide-based,[66] but cellulose acetate is still widely utilized in the field.[67] With the success of polymeric materials for water purification, many porous polymer membranes are now being investigated for gas separation.[68] In particular, one area that has seen a great deal of interest in recent years is the development of mixed-matrix membranes,[69] wherein selectivity is added to the polymer through the incorporation of a gas selective porous agent. Many of these materials take advantage of other porous materials, most notably zeolites[70] and MOFs,[71] to achieve ultrahigh selectivity. Indeed, some researchers are already starting to look at more modern versions of porous polymers are potential additives for mixed-matrix membrane systems.[72]

While porous polymer membranes have been heavily utilized in water purification, the broader interest in non-membrane porous polymers was limited for a number of years. The study of porous polymers in academic settings started to take off in the mid to late 2000s. It was primarily initiated by the interest in other porous materials, particularly metal-organic frameworks (MOFs) (**Figure 1**). The increasing interest in MOFs resulted in a growing interest in general framework material design, with materials like porous polymers being designed to work around the traditional weaknesses of MOFs.[73] One of the weaknesses of MOFs is typically understood to be poor long term stability due to the relative weakness of the coordination bonds that make up the structures.

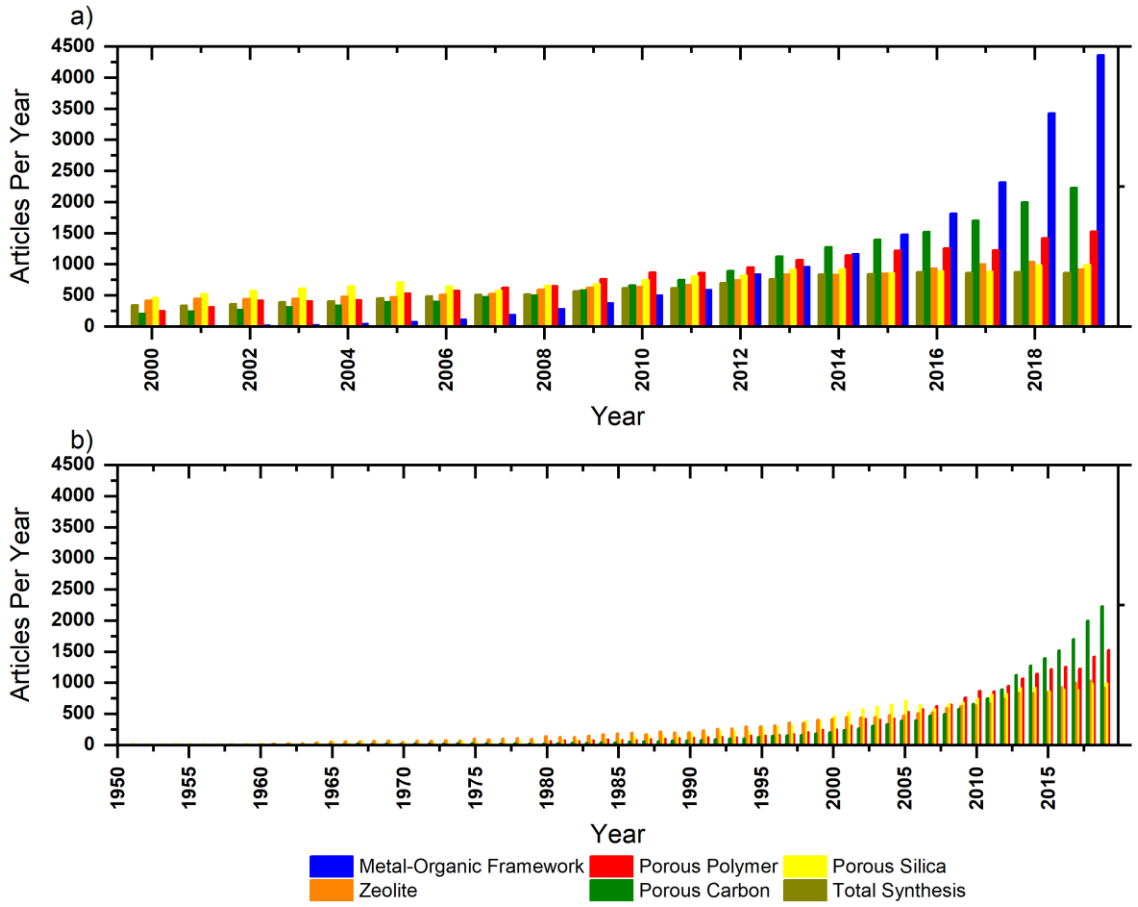

Figure 1. a) Number of citations for different topic areas organized by year. The increasing interest in porous polymers shows some correlation with the rising interest in MOFs. Total Synthesis is used as a general comparison. b) Four of the topics: zeolites, porous carbon, porous silica, and porous polymer, extended to 1950.

Modern research into porous polymers has focused on their differentiation from materials such as MOFs or activated carbons. In particular, porous polymers have often been compared against MOFs, typically because they both take advantage of organic chemistry to incorporate unique functional groups for advanced applications, but they utilize different chemical strategies for framework synthesis.[73-74] There are two major differences between MOFs and porous polymers. Porous polymers are typically much

more stable, particularly towards water. They are generally amorphous materials, with broad pore size distributions and slight batch to batch differences in structure.[73] This first point, improved water stability, has resulted in porous polymers being heavily studied for aqueous separations, in particular for organic dye[75] or for transition metal ion capture;[76] both of which are common aqueous pollutants. The second feature, their amorphous structures, and the hierarchical porosity that is typically a consequence of this have been proposed as reasons for their advantageous substrate diffusion in catalytic processes.[77]

In addition to solution-phase processes, PPNs are also known for their gas adsorption properties. One of the earliest pioneers in this area was Neil McKeown, who first dubbed the term, polymers of intrinsic microporosity (PIMs).[78-79] These materials take advantage of rigid functional groups within organic moieties, as well as the well-known geometries of organic carbon species, to generate materials with known pore sizes. Indeed, through careful tuning of organic connectivities and geometries, materials with ultrahigh surface areas can be readily made, with many PPNs, such as PAF-1 (PAF = Porous Aromatic Framework),[80] also known as PPN-6,[81] having surface areas greater than 7000 m^2/g.[80] In addition, these materials can take advantage of the ease of functionalization of these organic moieties to install selective functional groups for improved gas capture.[82] In particular, this functional group control has been heavily utilized for CO_2 capture. Basic functional groups incorporated within PPNs are designed to take advantage of the acidity of the CO_2 molecule for selective capture.[83] One of the most common functionalization techniques is through the post-synthetic modification of PPNs with amines through either tethering or loading.[84-85] Post-synthetic modification

refers to a series of techniques wherein a material is chemically altered, typically at their organic units, after generation of the heterogeneous material, as opposed to modification on the monomer or starting material.[86-87] Post-synthetic modification was traditionally utilized to describe modifications in MOF based systems.[86] However, the same methods can also be utilized in porous polymers, typically to a greater degree due to their higher stability.[81] Despite CO_2 being a fairly small molecule, there is some benefit in performing CO_2 adsorption in mesoporous materials. For one, the selective capture of CO_2 is highly dependent on the affinity of the sorbent towards CO_2, which in these cases is typically performed via amine incorporation. However, the post-synthetic addition of amines typically requires the use of relatively large reagents. As a result, the use of microporous materials in situations such as these can result in poor diffusion within the material, resulting in non-uniform material modification and thus poor CO_2 capture. Another issue is that the addition of these amine groups typically results in a reduction in available surface area and pore volume, caused by the space filling of the amine moieties.[88] As such, having a degree of mesoporosity in these materials allows for a higher degree of substrate diffusion while still allowing for high capacity capture. Additionally, CO_2 has a relatively high boiling point (-78 °C) and can readily undergo condensation within mesopores, even at relatively high temperatures.[89] The chemisorption of CO_2 on basic moieties tend to drop off dramatically with increased uptake coverage, due to the amines becoming saturated with CO_2. Because of this, the ability of these material to capture CO_2 after amine saturation is reduced considerably. Due to this, having a secondary method of capturing CO_2, through condensation, can be highly desirable.

Metal-Organic Frameworks

Metal-organic frameworks (MOFs) have been heavily studied in recent years, mainly for their use in areas such as gas storage and separation,[90] catalysis,[91] and biomedical applications.[92] MOFs have been heavily studied for many reasons, chief amongst them is their high degree of crystallinity, and their relative ease of modification. This ease of modification is due to the inherent structural features of MOFs, namely that they are formed using fairly straightforward coordination chemistry between metal clusters or nodes and organic linkers.

Coordination chemistry is the study of ligated metal systems, which can vary anywhere from the simple water ligands of aquo complexes, all the way to the permanent geometries of MOF frameworks. Coordination complexes have been utilized for centuries, particularly in the realm of dye molecules, as many transition metal complexes are highly colored.[93] However, many of the early uses, while perhaps understanding that the color required some sort of metal species to be present, did not have a strong understanding of what these compounds were. One of the most famous inorganic dye compounds, Prussian Blue, or iron(III) hexacyanoferrate(II),[93] was first discovered in 1704 and is considered a hallmark material in coordination chemistry. Prussian Blue is not only a simple coordination salt, formed from central hexacyanoferrate anions, but, due to the coordinating capabilities of both ends of the cyanide ligands, the material is also one of the earliest examples of an extended framework materials.[94]

From approximately the 17th century to the late 19th century, during the early days of modern chemistry, most coordination chemistry research focused on the preparation

and characterization of relatively simple complexes containing halide or amine ligands. For the most part, these compounds were simple laboratory curiosities or were potentially used in the dye or pigment industries.[93] At the time, there was little understanding of how these complexes were formed, and there was even less understanding regarding the nature of the metal-ligand interaction. It was not until 1893 when Alfred Werner published his seminal work on coordination chemistry "Contribution to the Constitution of Inorganic Compounds"[95] that we can readily trace the background and origins of modern coordination chemistry.[96] Werner's major contribution to coordination chemistry lies in expanding our understanding of the term valence. Werner differentiated between charge valence, which is balancing the positive charge of a metal cation with negatively charged anions, and coordination valence, which is related to ensuring a saturated geometry for that particular metal complex.[96] Werner understood that coordination geometries can be fulfilled not only by charged species such as halides but by neutral ligands, such as amines. Additionally, Werner identified that charge balance ions do not necessarily have to be directly bound to the metal center, identifying the concept we now call the outer coordination sphere as an ionogenic interaction.[93] Werner's theories provided the basis for our modern understanding of metal-ligand interactions, and in particular, the importance of how the geometry around different metal centers are formed and how they influence the complex properties. Werner's background as an organic chemist, and chiefly in molecular chirality, allowed him to be one of the first to recognize metal-centered chirality.[96] Understanding the specific interactions between different ligands later resulted in other breakthrough theories such as the trans-effect theory which was postulated and

studied by Il'ya Chernyaev in 1926.[97-98] Chernyaey is credited with the trans-effect theory although it is widely accepted that his conclusions built upon the earlier work of Wener.[99] For the foundations of MOF design theory, the work of Ralph Pearson on Hard-Soft-Acid-Base (HSAB) theory is only second to Werner's coordination chemistry contribution.[100] HSAB is a qualitative theory attempting to explain the observations regarding reaction rates and equilibrium constants for metal-ligand interactions. The theory is based on the work of Gilbert Lewis, wherein he defined acids as atoms and molecules that act as a non-covalent two-electron acceptors when forming an adduct[101] and Lewis bases as atoms and molecules that act as two-electron donors when forming adducts.[101] In Pearson's work, a hard acid or base is small in size, has a high charge (generally positive for acids and negative for bases), or is non-polarizable.[100] Meanwhile, acids and bases that are large in size, have low charges, and are highly polarizable are considered soft.[100] Based on experimental observations, it was shown that hard acids tend to more strongly and quickly bind to hard bases. The same could be determined between soft acids to soft bases. In addition, in Pearson's initial work, he analyzed not only the effect of HSAB on adduct formation but also how this theory related to acid and base solvation.[100] He described solvation as essentially the formation of weak acid/base interactions, oftentimes through coordination of the solvent molecule to a metal center. The HSAB concept is perhaps one of the most singularly important coordination chemistry theories when it comes to the synthesis of robust coordination materials. In particular, this theory provides a framework for evaluating the relative strength of metal-ligand interactions.

In the mid 20th century, the field of coordination chemistry began to take off and form the foundation of modern inorganic chemistry. This "golden age" of inorganic chemistry focused on metal complexes and built upon the HSAB theory and complexation theories established by Pearson and Werner. Around this time, a number of researchers started becoming prominent in U.S. academic circles, most notably John C. Bailar Jr., Geoffrey Wilkinson, Henry Taube, Jack Halpern, F. Gordon Stone, and James Collman. These six are particularly notable for being the fathers of modern inorganic chemistry. As of 1983, as much as 50% of the total inorganic chemistry faculty can trace their academic lineage (Ph.D. or post-doctoral work) through these six faculty.[102] While the landmark moment in mid 20th century inorganic chemistry is oftentimes seen as the development of ferrocene by Wilkinson and the subsequent birth of organometallic chemistry,[103] another major development that occurred in the 1950s was the development of coordination polymers.[104] The terminology of coordination polymers are typically considered to have been developed by Bailar. Bailar was an organic chemist by training who developed an intense interest in coordination chemistry after starting his independent career.[105] Bailar's work focused on the development of three main types of coordination polymers, polymers containing pendant metal chelate sites,[106] polymers produced through the organic polymerization of functional groups containing metal complexes,[107] and perhaps most importantly for the development of the coordination polymer field, polymers made through coordination between metals and bifunctional monomers.[108] These initial coordination polymer materials, comprised of simple polymer chains, would later be referred to as 1D coordination polymers.[109] They are, in many ways, simple expansions

on the concepts of polymer chemistry. Essentially, a 1D coordination polymer is a copolymer in which one of the components contains a metal center. This initial class of coordination polymers was typically treated as a specific type of thermoplastic material, one with unique thermal and mechanical properties due to the coordination bonds within the material. As a result, these materials have largely been studied for applications in self-healing polymers.[110] Despite their limited use as permanently porous materials, the central feature of these materials, namely their reversible coordination bonds, is an essential characteristic for the formation of the higher dimensional, 2D and 3D, coordination polymers. This is particularly true when looking at the crystalline versions of these materials: MOFs.[111]

By the late 1980s, it was clear that certain types of coordination polymers could be made crystalline, with some of the earliest work coming from the Robson group at the University of Melbourne, wherein he developed crystalline versions of 2D[112] and 3D[112] copper-based coordination polymers. These early materials were constructed from weakly coordinating pyridine units and transition metals that would be considered soft to intermediate by HSAB theory, Zn, Cu, and Cd. The 3D materials were grown out of solvents with reasonable metal coordination ability, such as acetonitrile or ethanol, which most likely aided in the growth of the crystalline materials. However, while there was some success in utilizing these materials for practical applications, including a report by Fujita of catalytic activity in a 2D Cd material,[113] these materials were mainly received as curiosities by the wider scientific community. While Robson was historically placed on

the sidelines in terms of MOF discovery, more and more people are starting to recognize his seminal contribution to the field.[114]

Perhaps one of the most recognizable contributions of the early work in this filed is that these initial studies of crystalline coordination polymers paved the way for the development of modern-day MOFs. The major difference between MOFs and coordination polymers is the presence of high levels of crystallinity in MOF materials.[111] This crystallinity is due to the self-correction of the material, essentially the ligand, metals, and crystallites can reversibly coordinate to each other due to the lability of the metal-ligand interaction, with this continuing until the material corrects to the highest ordered stability structure.[115] This self-correction process typically requires enough energy to cause decoordination of the metal-ligand bond, traditionally through solvothermal methods. In solvothermal synthetic conditions, the material self-corrects using thermal energy provided by elevated temperatures.[116] This solvothermal process is, in many ways, an evolution of the hydrothermal processes used to synthesize new zeolite materials. In many ways, this comparison to zeolitic materials is apt, as both are permanently porous, crystalline materials whose structures are guided by topology, essentially their regular repeating geometries.[117-119]

In many ways, the development of MOFs comes from two sides of material science: the development of zeolites and the development of coordination polymers. The field of MOFs started to take shape around the close of the 20th century, in the latter half of the 1990s. It was mainly spearheaded by two figures, both from different chemistry backgrounds: Omar Yaghi and Susumu Kitagawa. The backgrounds of these two chemists

very much resulted in their respective investigations into these materials coming from very different angles. Omar Yaghi's background was in the synthesis and characterization of oxometallate type species, mainly molecular type species.[120-121] These materials are typically synthesized using hydrothermal or solvothermal conditions, with a high degree of self-correction necessary to produce the thermodynamic crystalline products. This is very similar in many ways to how zeolite materials are made. This work paved the way towards his contributions to the start of the MOF field in two ways. First, it brought in the description of structural topology to MOFs,[118] with a focus on comparing them to zeolites,[122] and second it resulted in methods of producing robust and stable single-crystal materials using hydro and solvothermal methods.[123]

Kitagawa, on the other hand, had already developed a career in coordination chemistry[124] by the time he started his investigation into porous metal-organic species.[125] In fact, Kitagawa's early work with MOFs was, in many ways, a continuation of his coordination chemistry work and the work of predecessors in the field such as Robson[126] and Fujita.[113] Kitagawa's early work primarily focusing on the later transition metals, and particularly copper, in coordination chemistry. Throughout the 1980s and 90s a clear trend could be observed in Kitagawa's work: moving from zero-dimensional molecular complexes,[124] to one-dimensional coordination polymers,[127] to two[128] and three[125] dimensional coordination materials, culminating in his interest in crystalline porous metal-organic materials.[129] Many of the early materials developed by Kitagawa focused on the use of copper as the central metallic unit. In keeping with the general principles of HSAB

theory, these materials tended to form stable structures using soft base ligands, such as pyridines.

Many of the early MOFs suffered from poor stability, particularly in the absence of guest molecules, and many of these early structures would collapse upon the evacuation of the framework.[130] A major breakthrough in the synthesis of permanently porous MOFs came about when Yaghi and co-workers developed MOF-5, a zinc-based MOF that could maintain structural stability upon solvent removal.[131] While the stability of MOF-5 is considered quite low by today's standards and is highly susceptible to dissolution under aqueous conditions, it is still considered to be one of the earliest examples of a true MOF. After the development of MOF-5, MOF research exploded in the academic community, with the initial research focusing on other zinc and carboxylate based MOFs such as the Isoretilcular MOF series (IRMOFs).[132] However, the stability of these early MOFs is somewhat lacking. This was mainly due to the zinc cation used to make the metal nodes being considered on the borderline between hard and soft acids, while carboxylates are hard bases.[100] Thus, the HSAB theory, as applied to MOFs, had not been fully utilized. Improvements in the stability of MOFs only started to occur when researchers started using higher valent metals, such as Cr(III),[133] Al(III),[134] or Zr(IV),[135] in conjunction with carboxylate ligands. Other alternate ligand varieties, particularly azolate based ligands,[136] such as imidazole,[122] with softer metals, became popular options. The metal azolate frameworks (MAF) or zeolitic imidazolate framework (ZIF) style MOFs are made from these types of materials, using the nitrogen-containing azole-based ligands and tetrahedrally coordinated zinc ions. These materials were first developed in the early to

mid-2000s in the research groups of Xiao-Ming Chen[137] and Xiao-Zeng You[138] in China. However, a subsequent report by Yaghi in 2006,[122] resulted in the ultimate introduction of the term for these materials being referred to as ZIFs rather than MAFs. These materials are unique not only due to their water-stable properties but also due to their structural similarities to zeolites. In ZIF structures, the Zn(II) ions behave similarly to the Si(IV) centers in zeolites. At the same time, the imidazole linkers function similarly to the oxygen atoms in zeolites. In ZIF structures, this produces an M-Ligand-M angle of ~145° and allows for the generation of the same topologies as those seen in zeolites.[139]

This comparison with zeolites extends towards the common applications of MOFs. Some of the earliest interest in these porous framework materials revolved around their use as tunable scaffolds, allowing adsorption of different guest molecules inside their pores.[125] Early research into stable MOFs focused specifically on gas adsorption, focusing on methane[132] and hydrogen.[140] Methane and hydrogen storage is still an area of interest due to the growing need to store large quantities of both gases for energy generation applications. These gases are both light, non-polar molecules, and as such, they tend not to liquefy easily. Thus, storing these gases typically requires the use of high pressures and large tank volumes. However, smaller-scale uses, such as vehicular applications,[141] require higher quantities of stored gas in smaller tank volumes to achieve usable distance requirements. Adsorption in high surface area materials allows for a higher volumetric storage capacity of these gases in tanks than simply the gas inside the tank by itself at the same temperature. This is because these non-polar gases can interact with more material, even though they are only doing so through weak Van der Waals interactions. As such,

early work in this area of MOF research focused on the generation of ultra-high surface areas in gas-stable frameworks.[142] However, in recent years, it has become apparent that surface area alone is not enough to achieve high working capacity for methane and hydrogen storage.[143] The major hurdle that still exists in this field is that most processes that utilize methane, such as using methane in a car, do not operate effectively at pressures under 5 bar.[142] In many high surface area MOFs, a significant portion of the total gas uptake occurs in the 0-5 bar range. Due to this, the past decade or so has seen a push towards adding functionalities to framework scaffolds that can improve adsorption through dynamic, flexible structures or improving working capacities, through open metal sites,[144-145] or stimuli-responsive behavior.[146] There has been some success in using MOFs for commodity gas storage, including the Eco Fuel Asia Tour 2007 that utilized a car powered by methane adsorbed in Basolite C300.[147] Despite this, there is currently little in the way of commercial MOF methane storage. The current MOF derived gas storage techniques tend to be in more niche areas of study, such as in the low-pressure storage of semi-conductor grade gases,[148] where the high cost of the framework material is outweighed by the improved safety and storage capabilities of the MOF materials.

The other main feature of MOFs, their highly tunable functionalities, has also helped to pave the way towards the utilization of MOFs in catalytic applications. MOFs for catalytic applications first started to appear in the early days of MOF research,[113] with many of these early results focusing on the metal centers or nodes of the MOF. These early structures utilized the positively charged metal cation that made up the framework as a Lewis acid catalyst.[149-150] However, even in the early days of MOF catalysis, there was an

understanding that the constrained pore sizes and functional organic groups of MOFs could be utilized for more advanced catalytic applications. One of the earlier examples of MOF catalysis from Kimoon Kim showed that not only could a MOF be generated from a chiral ligand, but that this material could then be utilized for enantioselective catalysis in the trans-esterification of 2,4-dinitrophenylacetate.[151] While the enantiomeric excess of POST-1 was only 8%, the observation of enantiomeric excess, as well as size selectivity observed upon altering the alcohol substrate, did show the potential for MOFs as catalyst beds.[151]

While metal-centered reactivity studies have been quite prevalent in the study of MOFs as catalyst supports, there continues to be a growing interest in utilizing the ligand functionality within frameworks as catalyst supports. In many ways, this came about through the use of post-synthetic modification (PSM) that was developed and codified by Seth Cohen in the mid-2000s .[152-153] Cohen's work is very much the culmination of what Robson had predicted as a possibility in his work in the early 1990s.[126] Post-synthetic modification is a tool used to describe various methods of altering the functionality of a MOF after it has already formed a fully crystalline system. The utilization of post-synthetic modification for MOFs can function in a number of ways ranging from simple ion exchange[154] to coordination of new functional groups at the metal centers[155] to covalent bond formation on the ligand centers.[153] Since some of the earliest examples of post-synthetic modification have been utilized for the development of MOF-based catalysts, typically through the addition of binding pockets for more catalytically active metal centers.[156] This general method of MOF catalyst development, the incorporation of

known catalytically active species within a framework solid, is one that is still widely utilized by modern researchers. In particular, MOFs are often thought to be advantageous as these materials are theoretically capable of achieving the rates and selectivities of homogeneous catalysts, while at the same time having a higher degree of recyclability due to their heterogeneous nature.[157] Another potential advantage of MOFs is that they can potentially achieve the spatial separation of catalytically active moieties, having the potential for tandem catalysis. This area of research is still ongoing, with many unique approaches to syntheses that utilize MOFs as catalysts. While, as of this moment, no MOF based catalysts have seen widespread utilization, work in the synthesis of specialty chemicals such as the tandem semisynthesis of artemisinin,[91] takes advantage of the spatial control of MOFs to introduce multiple functionalities in a designer chemical. To date, this represents a new approach to a highly intriguing area of research for the multistep synthesis of specialty chemicals.

Thermolysis of MOFs and Their Resulting Products

Characterizing the thermal decomposition of MOFs has been a part of the field since the development of some of the earliest MOFs. Most MOFs have been characterized by thermogravimetric analysis (TGA), partially as a means to characterize the thermal stability of the materials,[131] but also to characterize the activation and loss of guest solvents.[55] One of the earliest stable MOFs, MOF-5, was initially characterized by TGA, first, to quantify the desorption of guest solvent. In their initial report, Yaghi and coworkers described two initial, non-decomposition mass loss events, one at 65 °C, a mass loss of 5.6% corresponding to the loss of one water molecule per formula unit, and a

second event at 160 °C of 22.5% corresponding to the loss of one DMF molecule per formula unit.[55] In their subsequent report, they described the final decomposition of MOF-5 as occurring at ~410 °C. However, notably, they do not show the TGA curve for the material.

Following this example, many other MOF reports included TGA decomposition data, including HKUST-1,[158] MIL-100,[159] UiO-66,[160] and ZIF-8.[122] The ultimate thermal decomposition of most MOFs comes from the instability of the organic linkers, particularly the fact that they can be thermally labilized from the metal centers. TGA analysis of common linkers, such as terephthalic acid, generally shown mass loss events starting around 275 °C[161] this corresponds well with the initial decomposition temperature of certain terephthalate based MOFs such as MIL-101(Cr).[133] However, this mass loss event is mainly due to the sublimation of terephthalic acid, while given as 400 °C under sealed tube conditions,[162] tends to occur around 300 °C under the open atmospheric conditions common to TGA measurements.[163] Actual thermal decomposition of terephthalic acid, and other larger aromatic carboxylic acids, under sealed conditions, tends to occur closer to 500 °C, with decomposition beginning due to decarboxylation.[161] This labilization based decomposition can be readily observed when comparing the decomposition temperatures of terephthalate based MOFs, with MIL-53(Cr)[164] and MIL-53(Al)[165] decompose at 450 °C, while the less stable Zn based MOF-5 decomposes at only 400 °C.[131] However, while metal-ligand decoordinaiton is often the root cause of MOF decomposition, other factors come into play. In the related MIL-101 system, which uses terephthalic acid and a trinuclear Cr or Fe center, as opposed to the 1D chains of octahedral

M^{3+} centers of MIL-53, decomposition instead occurs at 300 °C for the Cr[133] and Fe[166] versions. The decomposition, in this case, is due to a reduction at the metal centers caused by decarboxylation of the ligand, which can occur due to the redox-active nature of Cr^{3+} and Fe^{3+}.[167] This decarboxylation results in a one-electron reduction of at the metal centers, aided by the resulting $M^{3+}{}_2M^{2+}$ system being electronically neutral.[168] Zhou and coworkers showed that this decarboxylation can occur at relatively low temperatures (~225 °C) in the triiron acetate cluster-based PCN-250.[169] In this case, the decarboxylation does not go to completion at first. Instead, it occurs in stages, with the only monodecarboxylation on the tetracarboxylate occurring initially. This staged decarboxylation allows the material to maintain crystallinity during the early stages of ligand decomposition, giving PCN-250 a decomposition of nearly 400 °C.

The thermal decomposition of azole based MOFs, such as ZIFs[122] and MAFs,[138] are noted to have both a ligand decomposition as well as a delegation component. The thermal stability of imidazole species are generally thought to be relatively high, with imidazole based ionic liquids generally seen as having decomposition temperatures around 450 °C[170] and molecular imidazole metal complexes shown to degrade from 150 to 300 °C, depending on the metal complex.[171-172] Placing the imidazole within a framework material typically results in a decomposition temperature range of 200-400 °C,[136] which would suggest that the decomposition is mainly decoordination based. However, this is highly dependent on the functionality of the azole species, as high nitrogen content, such as in certain functionalized azoles,[173] are known for their structural instability and use as high energy materials.[174] Within MOFs, these materials show decomposition temperatures

similar to their parent ligands, suggesting that this decomposition is primarily ligand-based.[175] Interestingly, results in the literature suggest that the thermal decomposition of many ZIFs is highly dependent on the thermolysis atmosphere, with ZIF-8 having a noticeably lower decomposition temperature under air as compared to N2.[176] Work by Jerry Lin at Arizona State University suggests that this change in decomposition profile is related to ligand-based decompositions.[177] ZIF-8, despite only showing decomposition around 400 °C in standard ramp TGA experiments, will actually decompose at appreciable rates if kept isothermally at temperatures as low 250 °C.[177] They also observed an atmospheric dependence on the degradation rate, with the order going Air > Ar > N_2 > H_2/CO_2 at 300 °C, they hypothesize the oxidative effects are responsible for the higher air degradation rate, and that the saturation of the atmosphere with N_2 impedes the degradation of the imidazole ligands, as the degradation involves the loss of N_2.

The subsequent total thermal decomposition of MOFs can also be utilized to obtain novel materials. Complete thermolysis of MOFs results in the formation of metal oxide species from the residual non-volatile metals.[178] These metal oxide species tend to have some degree of meso or microporosity due to the loss of the carbon skeleton, producing porous metal or metal oxide particles that maintain the rough size and shape of the parent MOF.[179] These materials can then subsequently be used for many of the same applications as bulk metal oxides, such as gas sensing,[179] or photocatalysis.[180] The thermolysis process can also be utilized to obtain unique bulk structures for certain materials, such as a result from Ruifeng Li and Binbin Fan, where they pyrolyzed UiO-66 crystals containing sulfate

ions.[181] The resulting zirconium sulfates were templated by the MOF crystals, producing nanosheets embedded in bulk MOF, resulting in a flower-like morphology.

The thermolysis of MOFs under non-oxidative conditions leads to residual amounts of the ligand skeleton remaining as elemental carbon.[182] This carbon skeleton can be useful in its own right for applications such as battery electrodes,[178, 183] due to the high electrical conductivity of the predominantly graphitic phase carbon scaffold.[184] Some reports have developed methods of removing the metal species from the carbon, either through washing out the metal oxides with acid[182] or through the direct evaporation of volatile metals such as Zn.[185] The resulting carbon structures have significantly higher surface areas, due to the removal of non-porous metal oxide nanoparticles, which has been used to produce materials for Gas storage applications.[186] In addition to the added surface area from the MOF itself, some researchers have shown that the addition of organic guest species can be used to improve the surface area upon pyrolysis. One of the earliest examples of MOF-derived carbons (MOFdCs) by Qiang Xu and co-workers, showed that by loading MOF-5 pores with furfuryl alcohol they could achieve a surface area of 2872 m2/g upon calcination at 1000 °C.[182]

The thermolysis behavior of MOFs is highly dependent on the both the material conditions as well as the identity of the MOF. Work by Zhou, Page, and Ryder showed that both the pore structure, as well as the metal oxide phase generated during thermolysis can be altered through changing the gas environment of the iron-based PCN-250.[184] Meanwhile, Ben Xu, working on the thermolysis of isostructural MOFs, ZIF-8 ((2-methylimidazole)$_2$Zn^{2+}) and ZIF-67 ((2-methylimidazole)$_2$Co^{2+}), showed using in situ

FTIR and PXRD that the two MOFs behave differently during calcination.[187] In this work, Xu, and co-workers observed that ZIF-8 had a higher decomposition temperature due to the saturated coordination around the Zn^{2+}, with this higher temperature resulting in deformations before pyrolysis. Meanwhile, ZIF-67, due to the unsaturated valence of its Co^{2+} centers, is more susceptible to decomposition at lower temperatures, preventing the structural deformation observed in ZIF-8. Additionally, MOFs are known for their poor thermal conductivity, which has also been utilized in the case of MIL-53, where researchers were able to make a composite Fe_2O_3/MIL-53(Fe) composite by performing a slow, low temperature (450 °C) calcination.[188] This produced an outer layer of Fe_2O_3 while the interior maintained the MOF phase.

MOFdCs have also taken advantage of their embedded metal oxide nanoparticles to engage in catalysis. There are two advantages to using MOF-derived metal-oxide catalysts. First, they are more stable to hydrolytic conditions compared to the coordination bond containing parent MOFs, and second, they can readily be used for the fabrication of highly dispersed nanoparticles that can achieve high catalytic activities.[189] In particular, there has been a strong push for using MOFdC methodologies to develop both atomically precise and single-atom catalysts.[190] In one notable example Yadong Li and co-workers utilized the host-guest behavior of ZIF-8 to load the pores with the molecular species $Ru_3(CO)_{12}$. The small pores of ZIF-8 ensured the isolation of the individual guest molecules, which, upon calcination at 800 °C under a 5% H_2/Ar atmosphere, resulted in the generation of embedded Ru_3 metal particles.[191] These nanoclusters could then be utilized for the highly active oxidation of 2-aminebenzyl alcohol to the corresponding

aldehyde. In a related report, Li Du and Shijun Liao achieved highly dispersed single Fe atom carbons by using a gaseous doping approach, wherein ferrocene was allowed to disperse through ZIF-8 due to gas flow at elevated temperatures. The subsequent carbonization resulted in highly dispersed Fe centers which could then be used as an oxygen reduction reaction catalyst.[192]

The development of porous materials, like much of chemistry and science in general, was based on both our initial observations of nature, such as charcoal consumption in animals,[5] as well as the experiments and folk remedies of our ancestors.[1] While in many ways, these early applications of porous materials seem a far cry from our modern systems built with atomic precision, many of the same thought processes and procedures remain from antiquity. Modern porous materials now focus on not just the capture of gastrointestinal pollutants, but on capturing gases, separating out pollutants, and acting as nanoreactors for advanced syntheses. These new techniques take advantage of our growing understanding of how porous materials are formed and how they interact with adsorbates, as well as our improved ability to design novel and tunable materials. Indeed, as our ability to generate and characterize new adsorbents expand, we find that many of the processes can even be used to improve the creation and characterization of older materials like porous carbon.[193] Indeed, even while new materials such as MOFs are coming to the forefront of science, there is still new research being developed on activated carbon materials. Despite the age of this field, it still appears as if we have a long way to go to fully understand this unique class of porous materials.

Porous Material Theory and Characterization

While some porous materials, such as the crystalline zeolites or MOFs, can be structurally characterized via X-ray diffraction techniques, for the most part, characterization of pore structures needs to be conducted using physical measurements. Essentially the porosity needs to be analyzed through its interaction with guest species: how they transport through the material and how they fill the material's void spaces. The type of procedure utilized for the analysis of porosity typically is dependent on the size of the pores, with microporous materials (defined as materials with pores less than 2 nm) and mesoporous materials (materials with 2-50 nm pore sizes) being typically characterized via their gas adsorption ability. Meanwhile, macroporous materials (pores larger than 50 nm), as well as many mesoporous materials, are characterized via mercury intrusion porosimetry.[194-195] The use and characterization of macroporous materials are outside the scope of this body of work, but in brief, mercury intrusion porosimetry takes advantage of the non-wettability and lack of capillary action of liquid mercury to accurately measure the surface coverage of the material by the amount of mercury that is loaded into a porous material at a given pressure.[196]

When talking about gas adsorption, surface interaction is typically divided into two types of adsorption: physical and chemical. Physical adsorption, or physisorption, refers to the interaction between the adsorbent and the adsorbate via physical forces.[197] These physical forces take the form of non-covalent interactions, particularly Van der Waals interactions. Meanwhile, chemical adsorption, or chemisorption, refers to adsorption that results from chemical bond formation between the adsorbent and the

adsorbate.[197] The key feature of physisorption is the reversible interaction between the surface and the adsorbed material, whereas in chemisorption, the interaction, while typically not irreversible, requires additional energy input to achieve desorption.

The history of adsorption theory has been covered elsewhere,[198] but in brief, the major contributing theories to modern porous material characterization are two-fold. One of the initial codified adsorption theories was developed by Irving Langmuir in the 1910s,[199-201] wherein he developed the initial models to describe monolayer adsorption. Adsorption, which had been initially developed as a term in the 1880s by Emil du Bois-Reymond,[202-203] is defined as the increase in density of a fluid at a surface or other phase boundary. The key feature of this process is the use of the term surface. This differentiates it from the related term absorption. Absorption simply refers to the retention of a material, typically a liquid or a gas, by another material, but does not specify any changes to the state of the absorbed matter.[197] The Langmuir model of adsorption describes how an adsorbate interacts with a surface through a monolayer. In this sense, a monolayer is essentially a thin layer of molecules interacting on a surface where this surface separates the adsorbent from the bulk adsorbate. The adsorption studies conducted by Langmuir were based on non-condensing materials, such as N_2 and CO on Mica at 90 K.[201] These materials have an adsorbent-adsorbate interaction that is significantly larger than the interactions between the adsorbed monolayer and the bulk gas. As such, a typical Langmuir adsorption isotherm follows a hyperbolic trend, with the monolayer slowly reaching an amount of maximum coverage. These isotherms can be the result of single-site adsorption, wherein the interaction between the adsorbent and the adsorbate is uniform

across the material, as well multisite adsorption, which are regions of different binding affinities between the scaffold and the gas. Multi-site adsorption is particularly common in systems containing chemisorption, as the chemical bonded gas molecules will adsorb at relatively low pressures and oftentimes cannot be readily removed. The second site then refers to subsequent physisorption, which occurs at higher pressures and is characterized but much weaker interactions. Through his studies, Langmuir developed equations to describe these isotherms in terms of adsorption affinity. Much of the body of work and equations derived from Langmuir's studies are still widely utilized in adsorption studies today.[204] The main characteristics of the Langmuir monolayer adsorption is that the surface interaction with the adsorbate has to be significantly greater than the interaction between free adsorbates. When this is not the case, such as when condensation occurs, the assumptions made by the Langmuir model begin to be less accurate in describing the system.[203]

The main limitations of the Langmuir equations are systems where there is significant adsorbate-adsorbate interaction. Subsequent theories developed by Brunauer, Emmett, and Teller, typically referred to as BET (Brunauer-Emmett-Teller) Theory, are particularly useful for studies that go beyond monolayer adsorption.[205] BET Theory assumes that once a molecule is adsorbed onto a surface, that molecule can then act as an adsorption site for an additional molecule, particularly at higher pressures. When looking at this multilayer adsorption approach, the BET model assumes that 1) the interaction between the adsorbed molecule and the surface is greater than the interaction between the first adsorbed molecule and the second (and subsequent) adsorbed molecules, and 2) that

each adsorbed molecule can act as an adsorption site for only a single additional molecule. As a consequence of this, BET theory multilayer adsorption assumes a direct layer-on-layer interaction, where the topmost adsorbed molecule is directly above the lower layer molecule.

BET theory is relevant when looking at systems where the adsorbate-adsorbate interactions are relatively similar in energy to the adsorbent-adsorbate interaction. In terms of gas-phase analysis, this mainly applies when looking at adsorption at the condensation point of a specific gas. This feature of the BET equation is utilized by N_2 adsorption analysis at 77 K (the condensation temperature for N_2), which allows for not only surface area determination but also pore volume analysis. N_2 is heavily utilized for pore size and surface area determinations for two reasons, 1) N_2 is non-polar and will generally not engage in chemisorption or other polarization-based interactions. Thus, adsorption is purely physical in nature, and 2) a liquid N_2 bath, which is necessary to achieve a controlled temperature of 77 K for condensation, is relatively inexpensive and quite common as compared to other alternatives. A typical N_2 adsorption analysis isotherm is performed by first evacuating a container containing the sample to be analyzed, then slowly dosing in N_2 gas once the sample reaches the condensation temperature of N_2 and is stabilized. At 77 K, condensation will occur once the pressure of N_2 gas in the container reaches atmospheric pressure (~1 bar). Still, significant long-term adsorption will occur at surface sites before that point, starting with the monolayer over the total surface area. As the gas is loaded into the sample and adsorbs onto the surface, the instrument measures the pressure and compares it to what the pressure should be for that amount of gas loaded

into an identical but empty tube. The difference between the sample and the reference is the amount of gas adsorbed. By knowing the cross-sectional area of the adsorbate (0.162 nm^2 for N_2),[206] once you determine the pressure range for monolayer adsorption, you can use this information to determine the surface area. At higher pressures, adsorption of N_2 at 77 K results in capillary condensation, which allows for the determination of total pore volume for micro and mesoporous materials.

Typically, when investigating porosity via N_2 adsorption, the desorption process is also performed. This is done by slowly opening the sample to vacuum and viewing how the pressure changes in regard to the loss of gas. In porous materials containing capillary condensation, the desorption often occurs at different pressures compared to the adsorption pressure. The hysteresis loop that is generated from this difference allows for an accurate determination of the pore size distribution in the sample. This combination of information, both the shape of the adsorption isotherm, as well as that of the pressure range and size of the hysteresis loop, can be described by one of the six isotherm types as codified by IUPAC.[207] These isotherm types which are based upon countless examples in the literature, describe what type of adsorption is occurring in a material. By studying the monolayer formation, micropore and mesopore filling, and capillary condensation using BET theory, it is easy to gain a rough idea of the pore structure and shape of the porous material (**Figure 2**).

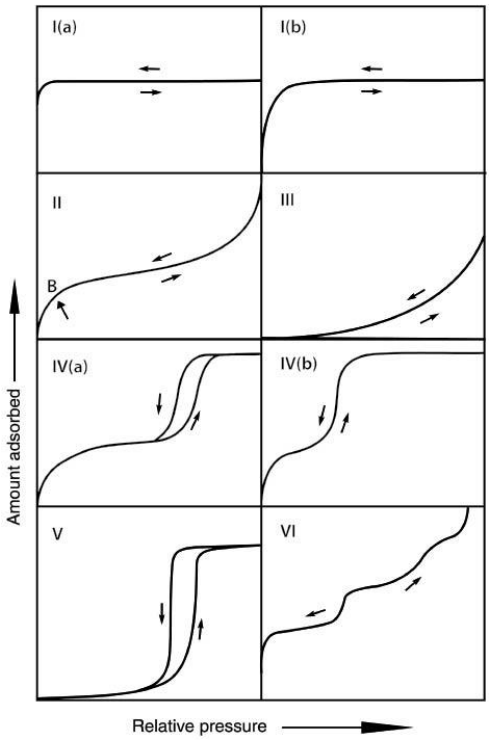

Figure 2. The main adsorption isotherm types: I) Purely microporous material with narrow pore size distribution Ib) microporous material with a broader pore size distribution, II) Macroporous material, B represents the completion of a monolayer, III) macroporous material with weak interactions with adsorbate, IVa) Mesoporous material with capillary condensation in narrow pores IVb) Mesoporous material with open or cylindrical pores, V) Mesoporous material with pore-filling by weakly interacting adsorbate, VI) Layer-by-layer adsorption on uniform surfaces. Reprinted from *Pure and Applied Chemistry*.[207]

Pair Distribution Function Analysis and Neutron Total Scattering

While X-ray diffraction methods have been utilized for over 100 years to solve the structures of crystalline materials, the characterization of semi-amorphous or nano-crystalline materials has remained challenging. A nano-crystalline material is one in which there is structural order, but it only occurs on the nanoscale, typically less than 100 nm. For these materials, some structural characterization can be performed via powder diffraction data, followed by analysis using methods such as Rietveld refinement.[208] In a

typical Rietveld refinement, a known crystal structure is fitted to a one-dimensional diffraction pattern through the systematic fitting of different phase and instrument parameters.[208-209] While this can give information regarding structural changes or dynamics compared to a structural model, this process is hampered by the effect of nano-crystallinity on the diffraction pattern. Due to the small scale of these materials, they are prone to peak broadening in diffraction experiments. This peak broadening can be used to characterize the size of the crystallite using the Scherrer equation,[210-211] but it is often difficult to get other structural information due to the low statistics for diffraction peaks, particularly as peak overlap becomes an issue with nanoscale materials. In addition, nanoscale features are often distinct from bulk structures due to the structures often being more closely related to the edges of the material, as opposed to most structural models, which assumes that the atoms being investigated are part of a bulk sample. These edge features can result in perturbations of the atomic structure that is not typically captured in the diffraction data.

While the information gathered from x-ray diffraction data can be useful for the investigation of the average structure of materials, understanding the local behavior of these materials, particularly how this behavior varies from a pure crystalline material, requires a different set of methodologies to obtain. Pair Distribution Function (PDF) analysis, is a technique based upon the total scattering of X-rays, neutrons, or electrons, from a material.[212-215] In this theory, the total scattering is comprised of both the Bragg scattering (typical diffraction peaks) as well as the diffuse scattering, which is comprised of atomic scattering when the conditions of the Bragg equation: $n\lambda = 2d\sin(\theta)$, are not met.

In PDF data, the G(r) value, is a one-dimensional curve representing a probability of another atom being at a distance, r, from any other atom.[214] As a consequence, this data gives an account of the real space atomic distances within a material. As diffraction data is collected in terms of reciprocal spaces (given in terms of either 2θ or the magnitude of the momentum transfer vector Q ($Q = 4\pi\sin(\theta)/\lambda$), PDF data must be produced from the sine Fourier transform of this reciprocal space data.

Since the early 20th century, there has been an understanding that the data generated from utilizing PDF methods contains potentially useful real space information regarding materials. However, two factors severely limited the usefulness of this procedure. The first of these limitations was the time-consuming calculations that needed to be conducted to convert the reciprocal space data into real space. Additionally, once the real space data was generated, it was typically of poor quality with many artifacts and noise related to the quality of the total scattering data.[213-214] The first problem could be solved by the increase in scientific computing power that started in the 50s and 60s. Along with this increase in computing power came an increased ability to solve x-ray diffraction data on crystalline materials.[208] The new ease of solving crystalline systems resulted in a reduced interest in PDF results as the low data quality was of limited usefulness for the majority of structure determinations.[214] The errors associated with data quality come predominantly from two sources: the Q resolution and the Q_{max}. Q resolution refers to the value of ΔQ and is generally related to the maximum real space, r, value that can be achieved via PDF. At low ΔQ, the PDF begins to dampen, and the peaks become much broader at higher values of r.[216] Meanwhile, the Q_{max} effects the real space resolution of

the PDF. At sufficiently low Q_{max} values, the peaks begin to fuse together, and much of the structural information is lost.[213] The Q_{max} value is essentially the maximum available momentum transfer and is directly related to the energy of the incident beam. Because of this, high Q_{max} values only became available with the introduction of spallation neutron sources in the 1980s.[214] Spallation neutron sources operate via the release of neutrons from a target upon hitting the target with a high energy beam, typically a proton beam.[217] While spallation sources are energy-intensive, they have a benefit over traditional reactor sources in that they have large neutron fluxes. These fluxes have controllable energy, and, for PDF, they tend to have high energy "tails" of neutrons that can result in high Q_{max} values.[214, 217] For comparison, the use of X-rays for PDF analysis only really began to be utilized after the development of third-generation synchrotrons in the early 1990s, as these systems were purpose built for high beam brightness.[213, 218] As such, most raw data for PDF analysis is collected at large government-run user facilities. There are laboratory-scale instruments that are capable of achieving the X-ray energies needed for PDF. However, they are typically limited to cathode sources that can only achieve limited beam intensities. This limitation results in generally low statistics and long collection times.[213]

Neutron sources have distinctive differences in PDF diffraction analysis in comparison to X-ray sources. Most notably, neutrons, as fermions, have a nuclear spin of ½, giving them a magnetic moment. Thus, neutrons are susceptible to scattering from the magnetic moments of other materials.[219] Because of this, diffraction analysis using neutrons needs to account for not only the atomic space group but also the magnetic space group.[220] In addition, as neutral particles, neutrons do not interact with the electron cloud of an atom

like X-rays do. Instead, neutrons scatter directly off of the nucleus of an atom.[219] This has two effects. First, the statistics of neutron scattering tend to be low, with only a small number of incident neutrons resulting in a scattering event. Therefore a high degree of sample penetration can be achieved. Additionally, neutron scattering is highly susceptible to changes in the nuclear structure of an atom, particularly in the case of different atomic isotopes.[219] The intensity of the scattering from individual nuclei, determined by the scattering length (b), tends to vary significantly between atoms that neighbor each other in the periodic table.[221] In particular, it should be noted that scattering lengths tend not to differ significantly with atomic number, Z. In turn, this makes neutron scattering particularly advantageous for the study of materials with a mix of light and heavy elements. Unlike x-ray diffraction, in neutron diffraction, the light element signal is not drowned out by intensive signal from the heavy elements in the sample. It should also be noted that neutron scattering lengths can be negative, most notably in the case of protium (^{1}H, the main isotope of hydrogen). Negative scattering lengths are related to the scattered neutron phases that do not change during the scattering event. Rather, it is related to a slightly attractive force during the scattering event.[219, 221] Another factor that is mainly observed in hydrogen isotopes in incoherent scattering. This is an effect where individual components of the scattered neutron beam do not interact in a phase-coherent manner. Protium has a large incoherent scattering length, which often results in the formation of large backgrounds in neutron scattering data.[219] However, deuterium (^{2}H), has a positive scattering length and is also a coherent scatterer, which has resulted in deuteration becoming a highly useful technique for investigating hydrogenated materials.[222]

The analysis of amorphous materials has been greatly expanded by the use of methods such as PDF. In turn, this is resulting in a greater degree of interest in developing new materials with tunable properties through nanoscale interactions.[215,193] The use of scattering methodologies make an excellent complement to traditional amorphous material characterization methods. In the following chapters, I will show through examples in both porous polymer networks and porous carbons how structural information ranging from the atomic scale all the way to the bulk scale can be accomplished through the controlled use of both characterization and application data, thus gaining an improved understanding of the structure/property relationship of these materials.

CHAPTER II

IMPROVING ALKYLAMINE INCORPORATION IN POROUS POLYMER NETWORKS THROUGH DOPANT INCORPORATION*

Introduction

Global warming has become an imminent environmental threat, with climate change being considered a contributing factor for the increase in frequency and severity of inclement weather,[223] potentially resulting in negative health effects through preventing access to health services,[224] as well as hurting the global economy through expensive weather remediation.[225] One of the main gases of concern, CO_2, is mainly sourced through the burning of fossil fuels and has experienced an exponential increase in atmospheric concentration since the 1800s.[226] Fossil fuels account for 63% of the energy generated in the US.[227] With fossil fuel reserves expected to last well past 2050,[228] finding new methods of CO_2 remediation is of the utmost importance to mitigate the effects of global warming. Many approaches to CO_2 capture have focused on post-combustion capture, or capture directly downstream from fossil fuel power generation. Post-combustion flue gas is typically comprised of approximately 12-15% CO_2 and 74-80% N_2, with the remainder consisting of ppm levels of SO_x, NO_x, particulate matter, H_2O, and O_2. Currently, mature post-combustion CO_2 capture processes utilize amine solutions, most notably 30% aqueous monoethanolamine (MEA).[229]

---

*Reprinted in full with permission from Day, G. S.; Drake, H. F.; Joseph, E. A.; Bosch, M.; Tan, K.; Willman, J. A.; Carretier, V.; Perry, Z.; Burtner, W.; Banerjee, S.; Ozdemir, O. K.; Zhou, H. C., Improving Alkylamine Incorporation in Porous Polymer Networks through Dopant Incorporation. *Advanced Sustainable Systems* **2019,** *3* (12), 1900051.

However, aqueous MEA solutions tend to have regenerative energy demands of up to 185 kJ per mol CO_2. Recovering the CO_2 and regenerating the sorbent can cause a drastic increase in the parasitic load of the system, often upwards of 70%.[230]

In order to reduce the energy demand of these solution-based systems, there has been a renewed effort towards the development of solid sorbents for CO_2 capture. Solid sorbents are advantageous as they capture CO_2 through physisorption, which does not entail the generation of full sorbent-amine bonds such as in the chemisorption-based capture of aqueous amine solutions. A number of different classes of solid sorbent have been investigated, such as metal-organic frameworks (MOFs)[231-232] mesoporous silicas,[233-234] zeolites,[235-236] and porous polymers.[83, 237] Solid sorbents demonstrate a number of advantages over their amine solution counterparts. The typical heats of adsorption for amine solutions range from 80-185 kJ/mol CO_2,[230, 238] whereas solid sorbents can have both broader and lower ranges for heats of adsorption; from 30-90 kJ/mol CO_2. This variability is depending on the available functional groups within the structure.[231, 236, 239] Purely physisorptive materials are often inadequate for CO_2 capture due to their low gas selectivity. As a result, there has been a push towards improving these solid sorbents through the incorporation of chemisorption functionalities. Typically, these improvements in capture capabilities directly result from the introduction of amine functionality within the porous materials. This incorporation can be through post-synthetic covalent tethering,[231, 240] physical incorporation,[234, 241] or direct incorporation into the porous framework scaffold.[237, 242]

Physical incorporation of amines within porous materials remains one of the more feasible methods of improving their CO_2 affinity. The low cost associated with physical incorporation-based procedures typically requires little more than the short-term contact between the porous material and a suitable amine. However, the weak physisorptive tethering of the amine to the surface of the porous material limits the conditions under which the material can be used. The amine leaching that can occur during sorbent regeneration results in a loss of CO_2 uptake performance capacity and leads to concerns over equipment corrosion and environmental exposure to toxic chemicals.

As an organic species, PPNs are ideally suited for functionalization, taking advantage of multiple organic synthetic pathways,[240] while still being producible at low-cost.[84] PPNs incorporated with basic moieties, such as amines, can produce high CO_2 selectivities, necessary to separate CO_2 from flue gas.[84, 240] The incorporation of amines into a PPN system is typically achieved through either post-synthetic modification of an existing porous polymer,[240] or the incorporation of basic moieties into the polymer backbone.[237, 242] Previous results from our lab have shown high uptake capacities using both PPN-6[240] and PPN-125,[84] both being porous networks post-synthetically modified with covalent diethylenetriamine tethering. However, in both systems, the addition of covalently tethered amine adds two steps to the sorbent synthesis. With processing adding additional days to the total sorbent reaction time and adding to the number of required solvents and reagents, this increases the total cost of the synthetic process. The preparation of PPNs with basic moieties incorporated directly into the polymer backbone show CO_2

uptakes greater than 10%wt only when adsorption is conducted at sub-ambient conditions. This limitation makes these sorbents not very useful for industrial-scale capture.

To combat these issues, we have introduced dopant materials: functionalized small molecules that can be added during PPN formation. The dopants utilize hydrogen bonding and strong dipole-dipole interactions to act as non-covalent anchoring sites for the post-synthetically loaded alkylamines. This dopant system represents a distinct advantage over other physisorptive systems as it can achieve the high CO_2 cycling capacity necessary for an industrially relevant sorbent while maintaining a high degree of cyclability.

Results and Discussion

The mPMF backbone of PPN-150 was chosen as a scaffold due to its ability to form a highly porous framework using commercially available materials (melamine and formaldehyde). However, melamine-formaldehyde resins are not inherently porous, and therefore must be made porous through the precise control of the synthetic procedure. The production of PPN-150 proceeded through a condensation polymerization of melamine and formaldehyde (in the form of paraformaldehyde) at high temperatures (150-170 °C) in dimethyl sulfoxide (DMSO) solution without stirring. Upon sitting for approximately one hour, an initial polymer gel formed. This gel is a soft, pliable material that collapses in the absence of solvent. Upon being left in the sealed container under an atmosphere of formaldehyde gas for three to 7 days, the gel slowly solidified into the thermoset melamine-formaldehyde resin. The resulting polymer monolith was then crushed into useable sized pieces and washed with acetone, tetrahydrofuran, dichloromethane, and methanol successively. The three main parameters that affected the porosity in PPN-150

were: the fill volume of the container used for synthesis, the solvent used for synthesis, and the reaction time. There is a mild correlation between the first two parameters as it appears that the concentration of formaldehyde gas in the reaction solution versus in the headspace of the material can result in a change in the surface area and pore volume of the resultant sample. As a result, both the vapor pressure of the formaldehyde and the solvent play an important role in determining the degree of micro and mesoporosity as well as the surface area of the material. The results of the synthetic tests (**Tables 1-3**) show that container fill volume, defined as the volume of the container filled by the reaction solution, does have a minor effect on the overall porosity of the samples. Reaction vessels that had a higher percentage of their volume filled resulted in polymer with lower BET surface areas. The reaction vessel was only 18.3% full, resulting in a PPN that had an 18.7% higher surface area compared to a sample that was produced in an 88.4% filled vessel.

Table 1. Reactor headspace optimization for PPN-150

Reactor Volume Percent Filled	**BET Surface Area (m^2/g)**	**Pore Volume (cm^3/g)**
18.3%	857	0.685
50.0%	838	0.886
88.4%	722	0.802

Table 2. Solvent System Optimization Data for PPN-150

Solvent System	**BET Surface Area (m^2/g)**	**Pore Volume (cm^3/g)**
Ethylene Glycol	356	0.761
Dimethyl Sulfoxide	854	1.11
Ethylene Glycol/Ethanol	251	0.542
Dimethyl Sulfoxide/Water	113	0.135
Ethylene Glycol/Water	298	0.653
Ethylene Glycol/Methanol	279	0.597
Dimethyl Sulfoxide/Methanol	518	0.508

Table 3. Time Optimization for PPN-150

Synthesis Time (Days)	BET Surface Area (m2/g)	Pore Volume (cm3/g)	TGA CO_2 Uptake (wt%, DETA loaded)
3	730	0.296	9.6
5	640	0.281	9.2
7	1014	1.042	5.3

Solvent comparisons were conducted in an attempt to produce PPN-150 using greener, more environmentally friendly solvents. These solvent choices were compared to DMSO, the solvent commonly used in the literature for mPMFs.[84] Unfortunately, no other solvent or solvent pairs came close to the high surface area or porosity of the DMSO synthesized sample. Reaction time analysis shows a distinct change in sample porosity as the reaction continues. In general, there appears to be an increase in overall porosity as the reaction progresses. However, changes in the pore size distribution (**Figure 3**) suggest that the increased porosity is mainly generated in the higher mesoporous range. Unfortunately, the mesoporous range is less relevant when investigating CO_2 capture after alkylamine loading (**Table 3**).

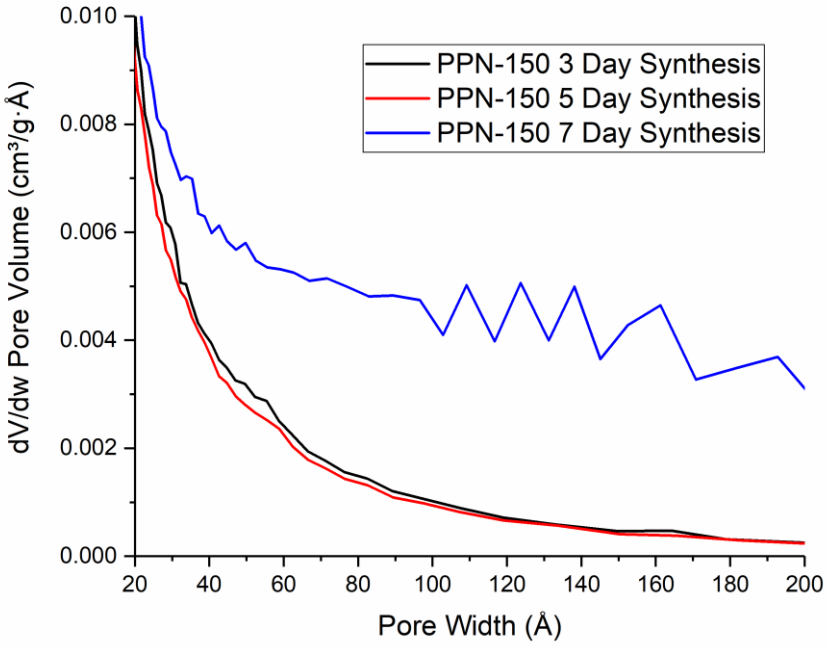

Figure 3. Pore Size Distribution Change for Time Optimization Study of PPN-150.

DMSO is known for having both a high boiling point and for decomposing near its boiling point into dimethyl sulfide, which could potentially interfere with the PPN reaction. Elemental analysis of the processed PPN-150 shows that the material is still 5.81% sulfur by mass (**Table 4**), suggesting that DMSO lingers in the sample, even after processing. However, heating the starting materials of the PPN in the absence of formaldehyde in DMSO shows no observable reaction.

Table 4. Elemental Analysis of PPN-150 Series Samples

Element	C	H	N	S
Theoretical Mass % for PPN-150	34.00	2.00	45.00	0.00
Experimental PPN-150	35.26	4.83	40.89	5.81
Experimental PPN-151	35.23	5.28	39.45	5.88
Experimental PPN-152	36.81	4.91	40.56	5.80
Experimental PPN-153	36.68	5.33	36.47	7.21
Experimental PPN-154	34.75	5.27	35.92	7.13
Experimental PPN-155	36.07	5.45	37.99	5.06
Experimental PPN-156	33.84	5.37	41.12	3.78

CO_2 uptake testing of lab-scale PPN-150 samples was conducted using thermogravimetric analysis (TGA) and showed uptake of 2.8 wt% under simulated flue gas conditions (0.15 bar CO_2, 0.85 bar N_2). Alkylamines were then incorporated into the polymer pores, taking advantage of the basic moieties in the alkylamines to engage in a weak chemisorptive interaction with CO_2. Loaded tests were performed using PPN-150 samples with a high surface area, produced in an 18.3% filled reactor using DMSO as a solvent, with a series of alkylamines. The alkylamines were doped into the polymer by mixing the solid PPN in a solvent, typically hexane, cyclohexane, or methanol, and adding the neat alkylamine to the solution. The alkylamine was allowed to penetrate the PPN with the aid of a sonication bath at 50 °C over the course of 3 hours. The PPN was then filtered, washed with a polar solvent (THF, Methanol) in an attempt to remove surface alkylamines, and then dried in a vacuum oven at 85 °C for one hour. The resulting white powder samples were then tested for CO_2 uptake under TGA conditions and run for 5 cycles (**Figure 4**). Based on the data gathered, the two highest-performing alkylamines were diethylenetriamine (DETA) and tetraethylenepentamine (TEPA). However, in an

effort to keep synthesis costs down, and due to the uptake values of the two materials being relatively close (both achieved >8% on a typical CO_2 capture experiment), we decided to focus our research efforts on the DETA loaded PPN.

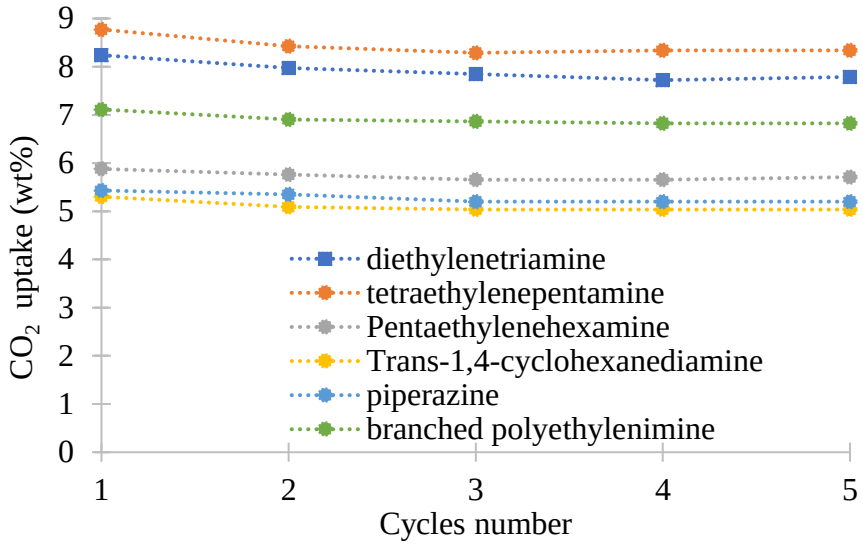

Figure 4. 5 cycle testing of different amines loaded into PPN-150. Diethylenetriamine and tetraethylenepentamine had the highest uptake totals of all the amines during every test.

During TGA cycling, it was observed that there was still a loss of uptake performance over the 5 cycle experiment. This was attributed to the loss of amine due to thermal regeneration. This loss is likely due to the main nitrogen component of the PPN, the triazine ring, only being weakly basic. This could be corroborated by the loss of sorbent mass between cycles. In order to alter the structure of the PPN, we opted to try dopant incorporation, adding functional molecules during the polymerization reaction, as a method of either altering the structure through templating and changing the porosity, or by adding secondary sites for amine tethering to occur. To that end, a series of 6 dopants were selected, with each doped material being assigned a number from 151 to 156 to

indicate that the material is a part of the PPN-15X family (**Figure 5**). The six dopants were added to the polymer before the initial gel formation, with the dopants added as a DMSO solution to a hot melamine solution prior to the addition of paraformaldehyde. The reaction temperature and conditions used were the same as for the base polymer, PPN-150.

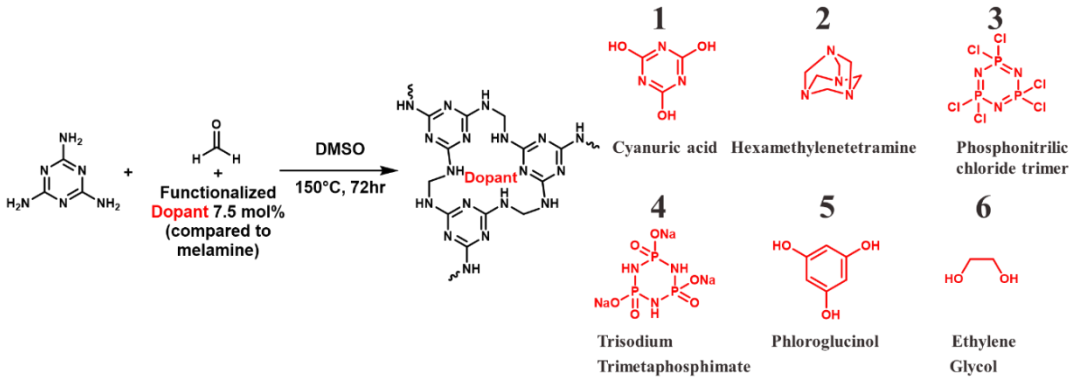

Figure 5. Procedure for producing the doped PPN-150 series polymers. The dopants, 1-6, are added to the synthesis during the polymerization. The initial reaction mixture must produce a homogeneous solution before polymerization, or else a reduction in porosity will result. Dopant 3 proved incapable of dissolving alongside melamine and paraformaldehyde, instead of reacting with both reagents, hence its overall lower surface area.

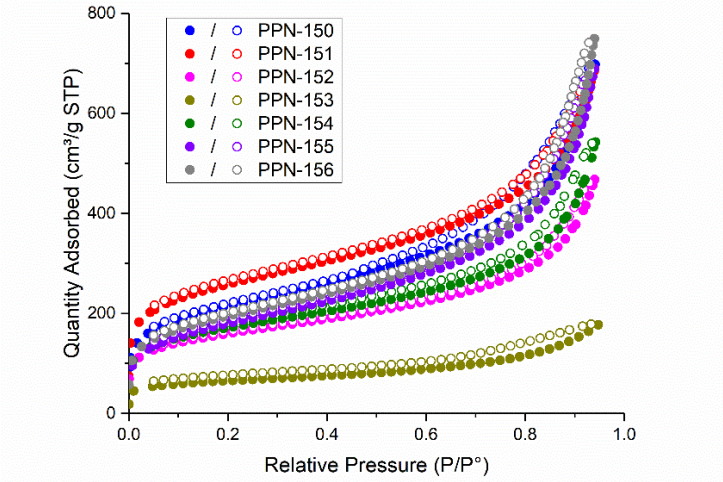

Figure 6. N_2 Adsorption isotherms for the PPN sample.

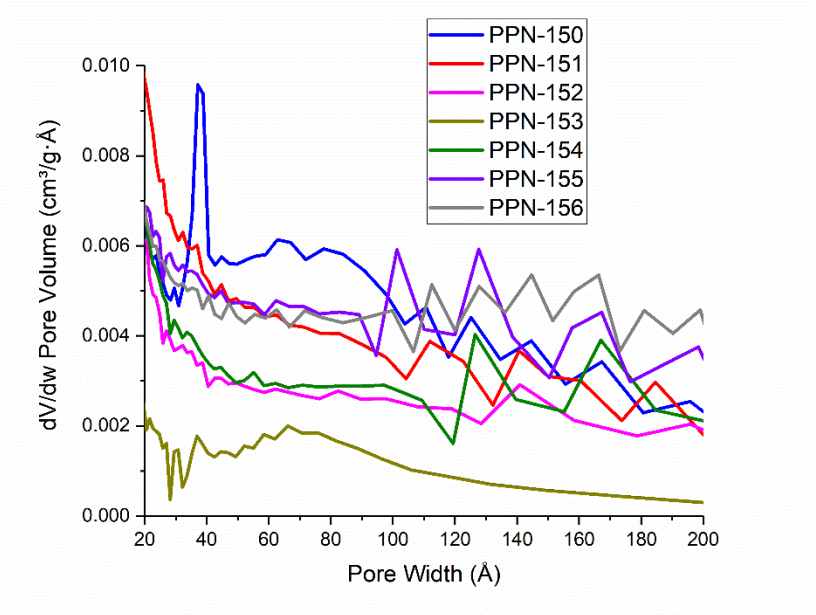

Figure 7. BJH Desorption pore size distribution of PPN samples.

The 6 doped PPNs all show a mix of both micro and mesoporosity, with a broad range of fairly large micropores, around 1.2-1.5 nm (**Figure 6-7**). The surface areas are typically consistent with that of the undoped PPN-150, except for PPN-153. The phosphonitrilic chloride trimer dopant partially collapses the porous structure. This was most likely due to the reactivity of the labile P-Cl bonds interfering with the desired polymer synthesis. The surface areas of all the doped materials except PPN-151 were lower than that of the undoped material. As the doping occurs during the polymer synthesis as opposed to post-synthetic modification, the loss in surface area was likely due to the increased mass of material added to the synthesis. However, amongst the doped samples, there appears to be a general trend of improved surface areas and total uptakes for the materials upon the incorporation of acidic functionalities in the dopants. Cyanuric acid, an acidic functionality, had the highest surface area of all the PPNs. The

phloroglucinol (slightly acidic) doped PPN and ethylene glycol (hydroxyl containing) doped PPN had the second and third highest surface areas, respectively. The trisodium trimetaphosphimate (charged species) doped sample had a surface area comparable to that of the ethylene glycol doped PPN. The hexamethylenetetramine (basic) doped PPN showed the lowest surface area of the non-reactive dopants. Condensation reactions, such as the one used to form PPN-150, can be catalyzed by acidic conditions.[243] This suggests that one of the main effects the dopants may have on the porosity of the sample is through catalyzing or impeding the condensation reaction.

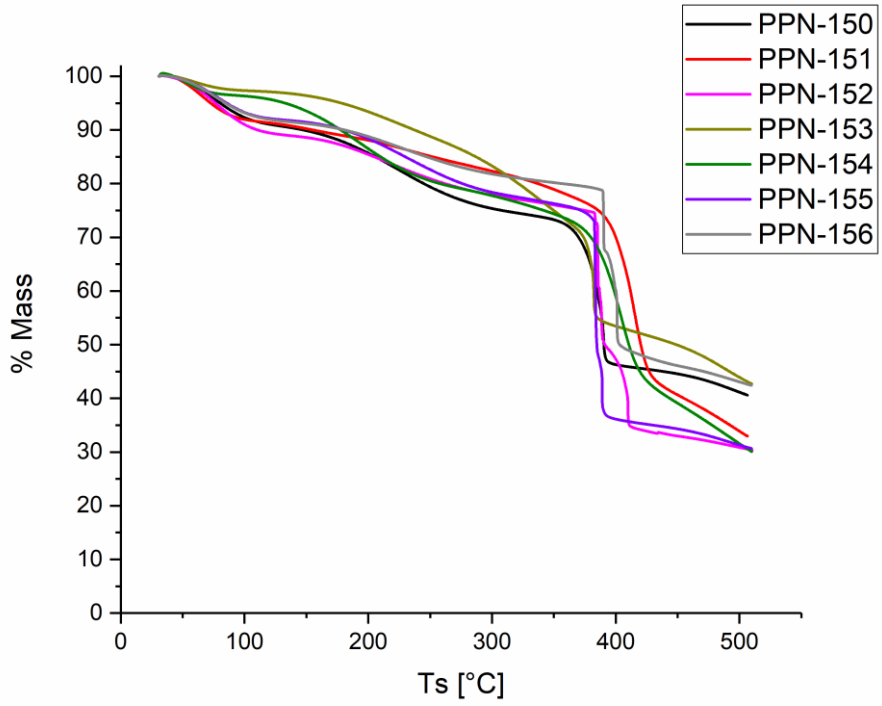

Figure 8. TGA decomposition curves for PPN-150 series polymers.

TGA decomposition analysis of the seven PPN samples shows that final decomposition for each material typically occurs around 350-375 °C (**Figure 8**). PPN-151 appears to have the highest decomposition temperature, around 390 °C. This high

decomposition temperature can be attributed to the stabilizing effects of the cyanuric acid-melamine interaction. This interaction is known to generate a highly stable melamine-cyanurate hydrogen bonding network.[244] Melamine-cyanurate has a significantly improved thermal stability compared to both melamine and cyanuric acid, decomposing at 400 °C, as opposed to the 300°C decomposition temperature of isolated melamine or cyanuric acid (**Figure 9**). It should also be noted that the same TGA curve type cannot be generated by physically mixing PPN-150 with melamine cyanurate or cyanuric acid, suggesting that this change in decomposition behavior is due to a new material phase generated during the polymerization reaction in the presence of cyanuric acid (**Figure 10**). IR spectroscopy was performed on the PPN series (**Figure 11**). Each of the PPN samples showed no noticeable difference from the baseline PPN-150. In order to probe whether the dopant molecules could be observed in the material, higher loadings of the dopants in the PPN samples were tested: 50 mol% cyanuric acid was reacted for 1, 2, and 3 days. Only the 1-day reaction appeared to show any presence of cyanuric acid in the IR spectrum of the resulting processed PPN (**Figure 12**). However, all three samples showed broadly similar porosities (**Figure 13**).

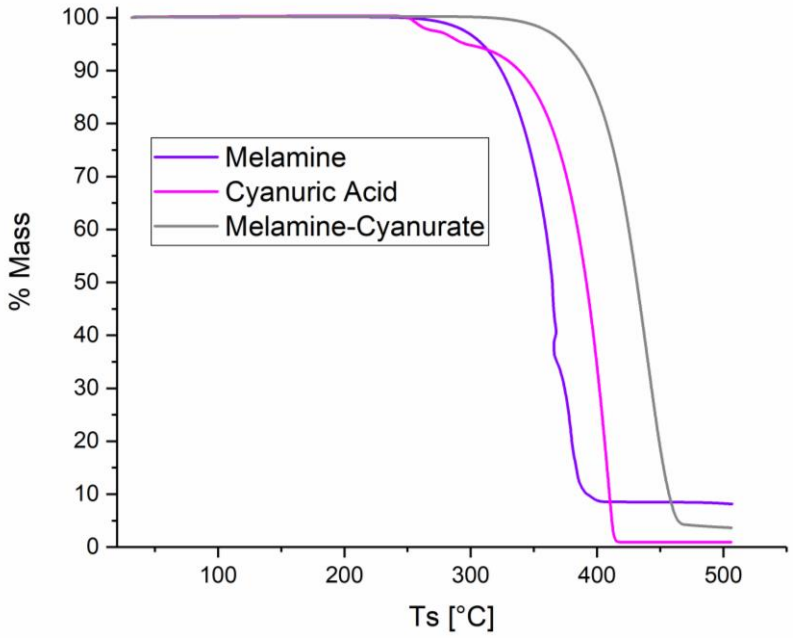

Figure 9. Decomposition of melamine-cyanurate and its components.

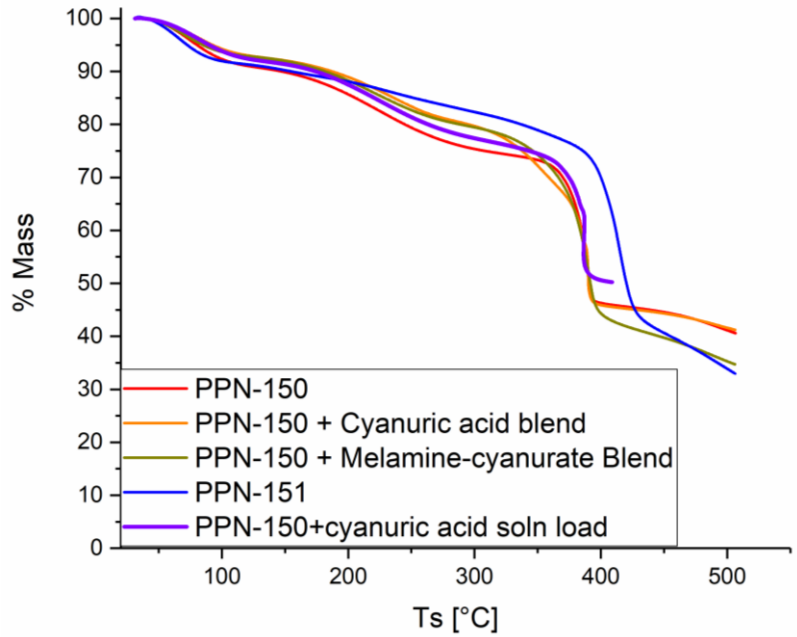

Figure 10. TGA decomposition of PPN-150 blended with melamine-cyanurate components compared with PPN-151.

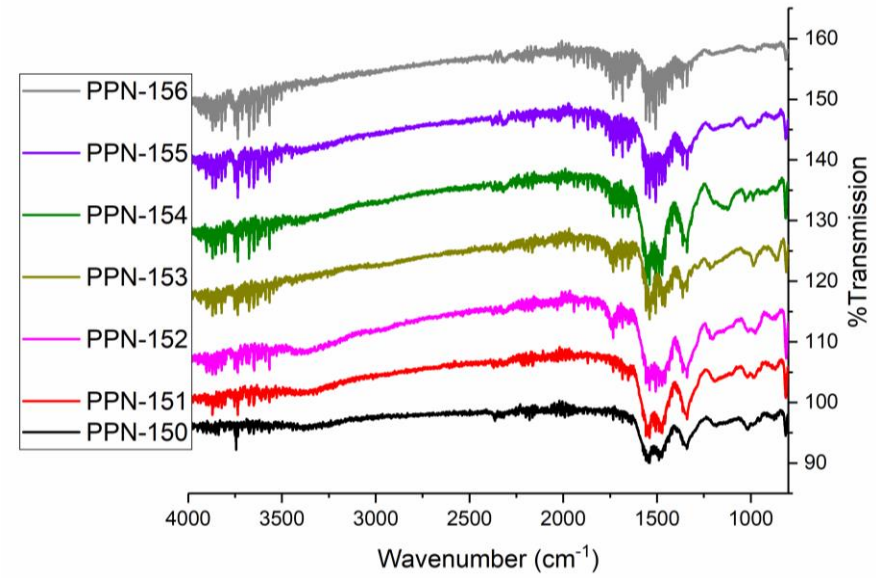

Figure 11. IR Spectra of doped PPN samples.

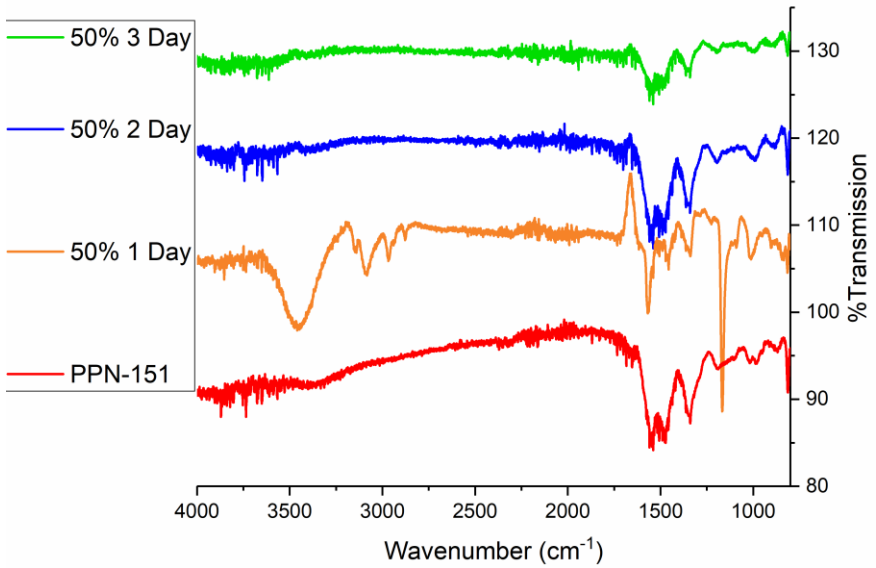

Figure 12. IR Spectra of 50 mol% cyanuric acid PPN-151 after different reaction times. After 1 day, the material shows a strong cyanuric acid peak, increasing the time to 2 or 3 days results in a similar structure to PPN-151.

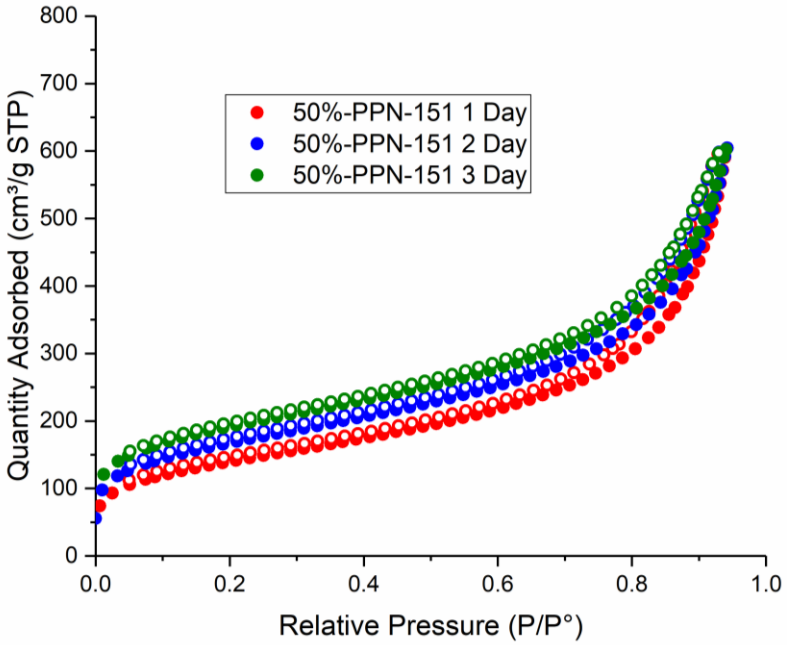

Figure 13. N_2 adsorption isotherms of 50 mol% PPN-151 samples.

Upon loading the doped PPNs with DETA, there was a marked drop in surface area, as the loaded amine pooled within the pores of the framework, limiting surface access to the N_2 during gas adsorption measurements (**Figure 14, 15**). However, there was a significant variation in the surface area drop among the different PPNs. Some PPNs (150, 152, 153) showed a drop in surface area upwards of 50%, while others show an approximate 50% drop (151, 154, 155, 156) (**Figure 16**). The PPNs with dopants that showed higher uptakes typically had dopants that contained hydrogen bond donors or acceptors as functional groups (OH, ONa). The PPNs with dopants that showed lower uptakes mainly appeared in systems that had less donating functionalities (tertiary amines, P-Cl bonds). IR Spectroscopy of the DETA loaded samples did not show any significant differences between each other (**Figure 17**).

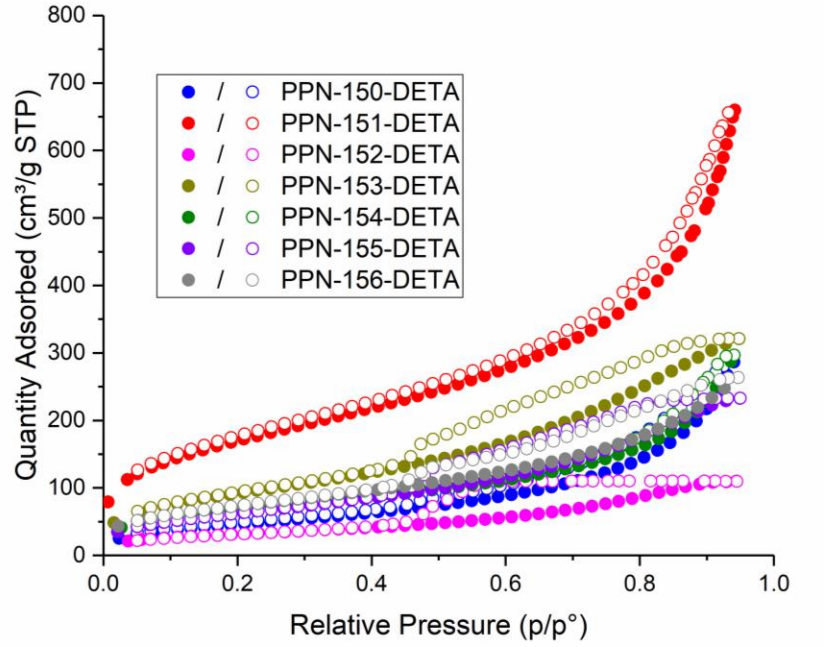

Figure 14. N_2 Adsorption isotherms for DETA loaded PPN.

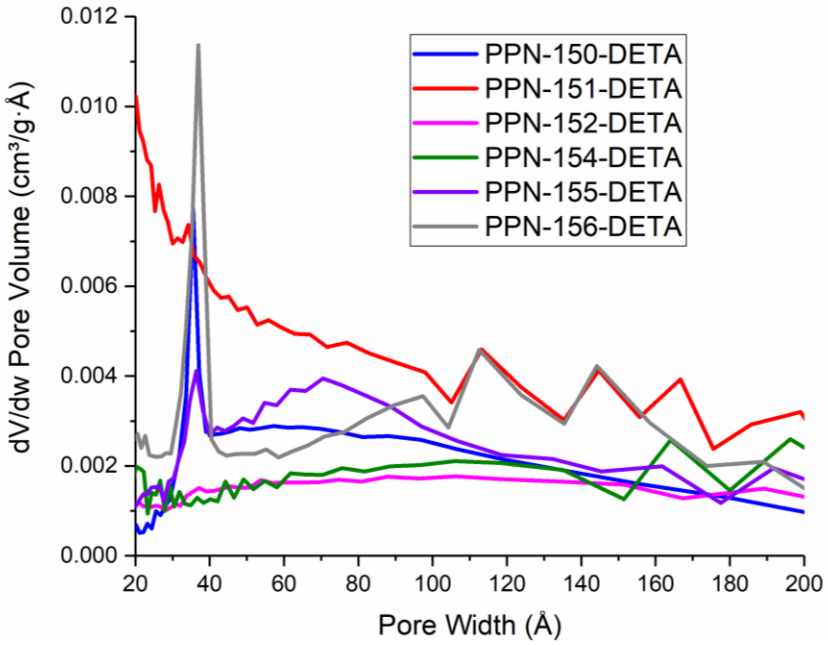

Figure 15. BJH Desorption pore size distribution for DETA loaded PPNs.

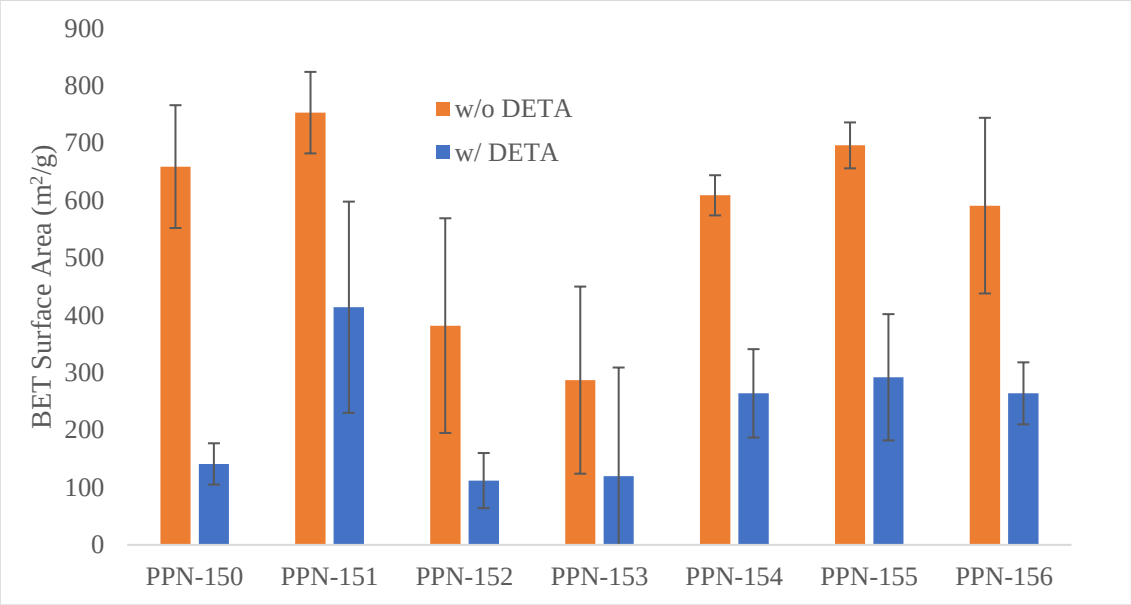

Figure 16. Comparison of BET surface areas before and after loading the polymer with DETA. PPN-150 shows a significant reduction in the surface area upon amine loading. Dopant incorporation in the PPNs does result in an alteration of this surface area drop.

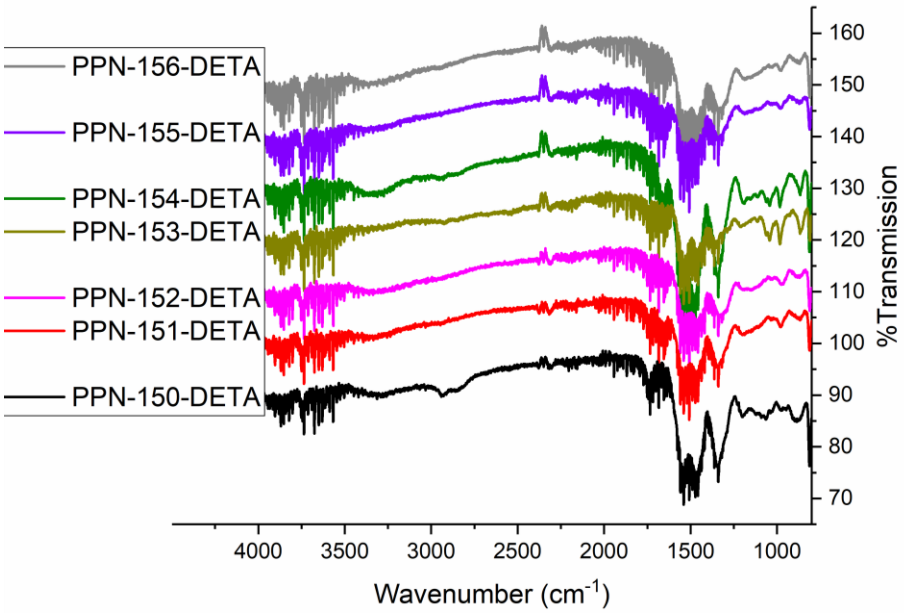

Figure 17. IR Spectra of DETA loaded PPN samples.

From these results, it was hypothesized that the samples with higher surface areas after DETA loading would be better CO_2 capture materials, due to the higher availability

of physisorption surfaces. In addition, there was interest in determining the effects of dopant inclusion on the cycling performance, namely, the loss in uptake between subsequent CO_2 adsorption runs.

The doped PPNs were investigated via a five cycle TGA experiment utilizing a 10-minute thermal activation at 85 °C between individual cycles, while adsorption was conducted at 40 °C for 40 minutes using a 15% CO_2: 85% N_2 gas mixture (**Figure 18a**). In general, there was a high degree of variation between synthesized batches, resulting in large standard deviations. Of the six doped materials, four of them showed lower CO_2 uptakes than the undoped PPN-150-DETA, with only PPN-151-DETA and PPN-154-DETA showing higher average uptakes over 5 cycles. Generally, the initial cycle of loading experiments demonstrated a higher uptake than subsequent cycles. For example, PPN-156-DETA gave an average cycle 1 uptake of 9.02%, whereas the average for cycle 2 was 6.66%. For this material, cycles 3 and 4 showed only a minor loss in uptake performance as compared to cycle 2. The loss of uptake from cycle 1 to cycle 2 was attributed to the incomplete regeneration of the sample after CO_2 adsorption, not the desorption of DETA. This was corroborated by an increase in sample mass after cycle 1, implying that it was unlikely that material was being lost as a result of the heat cycling. In one iteration of PPN-156-DETA, the baseline mass started at 14.99 mg. After cycle 1, the baseline mass increased to 15.69 mg, which was an increase of 4.7% (**Figure 19**).

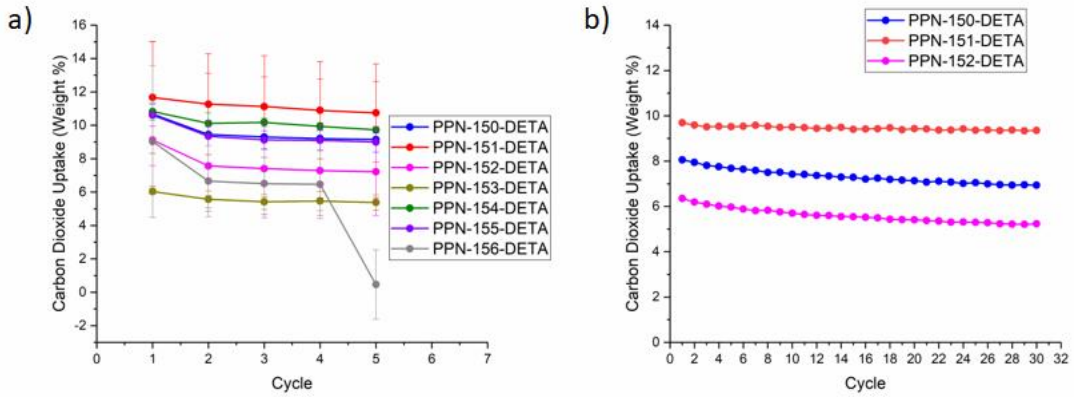

Figure 18. a) 5 cycle TGA run data using a 15% CO_2, 85% N_2 gas mixture for PPN-150 series polymers. PPN-150, 152, 155, and 156 all show noticeable drops in uptake after the first cycle due to an incomplete regeneration. b) PPN-150-DETA and PPN-152-DETA exhibit a general loss in uptake capacity as a function of cycle number over a 30 cycle experiment, losing 14% and 18% of their initial capacity, while PPN-151-DETA only loses 3.6% uptake capacity over 30 cycles.

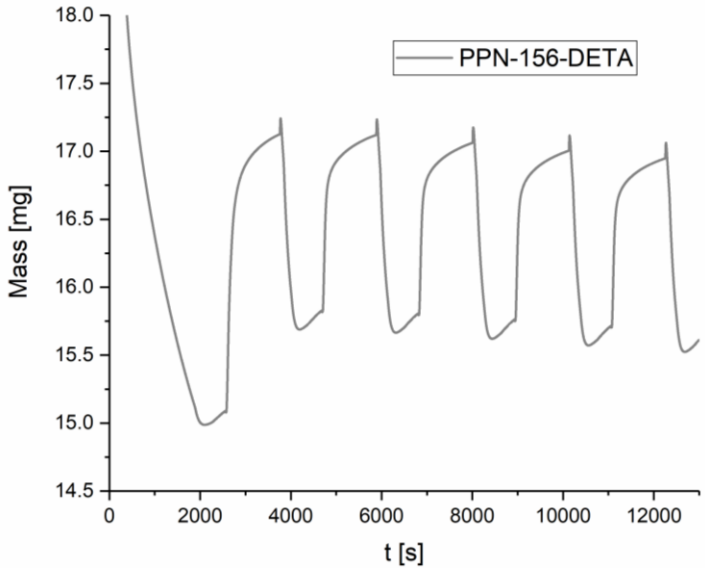

Figure 19. 5 cycle experiment with 85 °C for PPN-156-DETA, showing the increase in baseline mass between cycles 1 and 2.

Due to the low loss of cycling performance and high total uptake, further investigation of the long term cycling of PPN-151-DETA was conducted via an extension of the experiment to 30 cycles. For comparison, PPN-150-DETA and PPN-152-DETA

were also tested for long-term stability, due to PPN-150-DETA being the baseline material and PPN-152-DETA being a typical material that did not show marked improvement during short-term cycling tests. **Figure 18b**). Long-term cycling of PPN-150-DETA, as well as PPN-152-DETA, show a consistent loss in uptake with the progression of the cycles. The loss in performance averaged 14% and 18% respectively for PPN-150-DETA and PPN-152-DETA. Additionally, PPN-152-DETA showed an overall lower level of CO_2 uptake as compared to the undoped PPN-150-DETA. This was likely a result of the lowered surface area and porosity of PPN-152 in comparison with the base material.

The average uptake of PPN-151-DETA remained high relative to the other samples, averaging 9.46%. In addition, the material showed remarkably improved cycling performance over the baseline PPN, only losing 3.6% of its total performance over 30 cycles. This improved cycling performance, in conjunction with the DETA loaded surface areas, suggests that PPN-151-DETA CO_2 engages in a slightly different sorption interaction as compared to the other PPNs. This was corroborated by the variable temperature single component CO_2 isotherms and the calculated heat of adsorption values for PPN-151-DETA, which are approximately 10 $kJ \bullet mol^{-1}$ higher than that of PPN-150-DETA at similar CO_2 loadings (**Figures 20-24**).

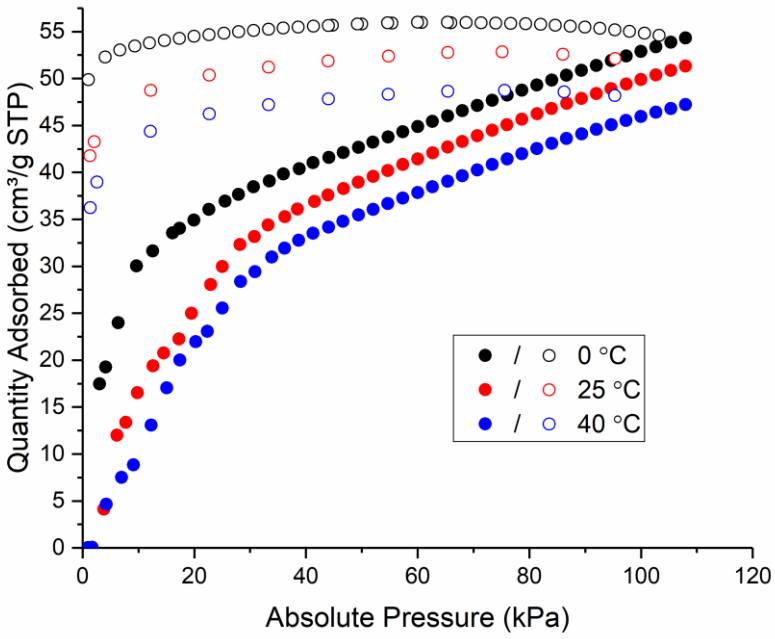

Figure 20. CO_2 adsorption isotherms for PPN-150-DETA.

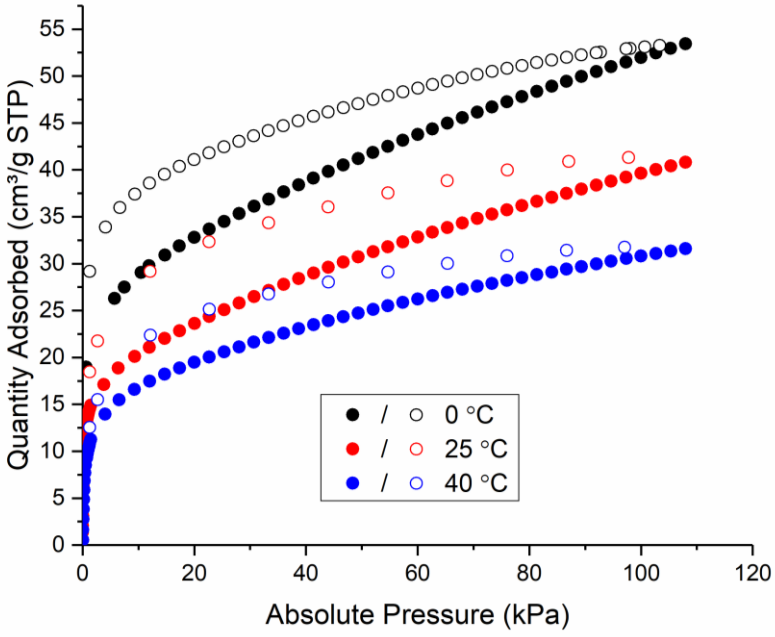

Figure 21. CO_2 Adsorption isotherms for PPN-151-DETA.

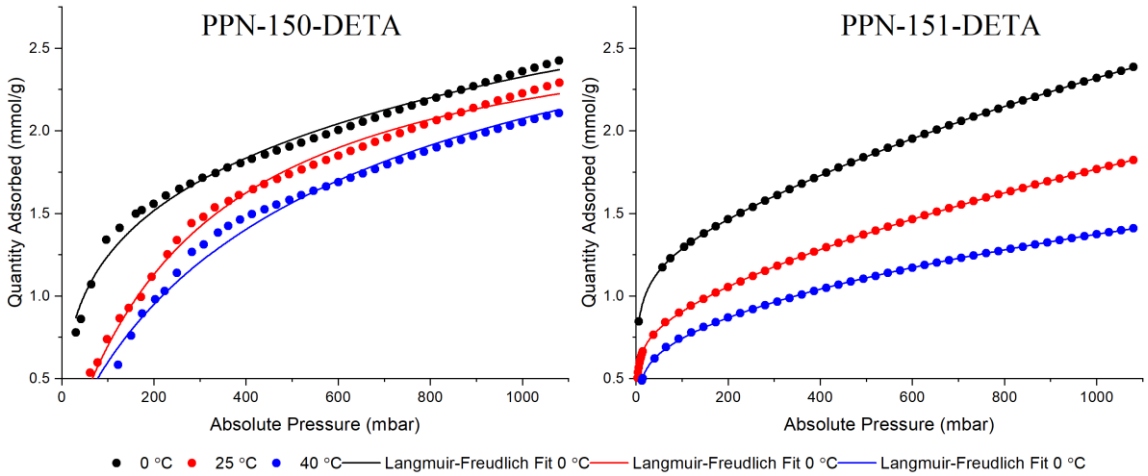

Figure 22. CO_2 isotherms of PPN-150-DETA and PPN-151-DETA fit to a dual site Langmuir Freudlich isotherm.

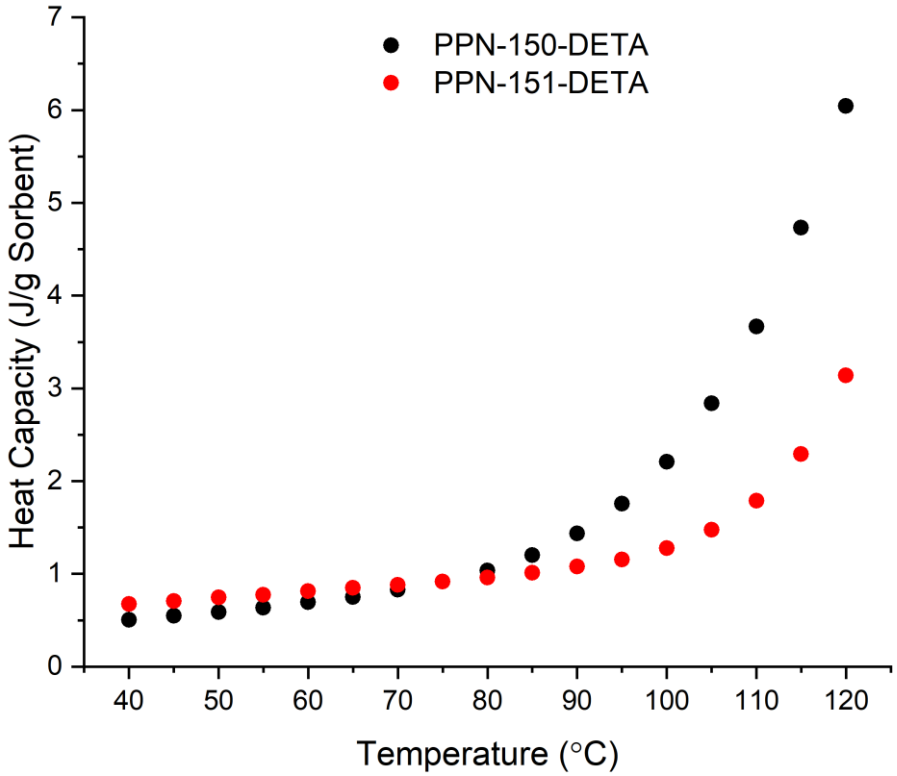

Figure 23. Heat Capacity as a function of Temperature for PPN-150-DETA and PPN-151-DETA.

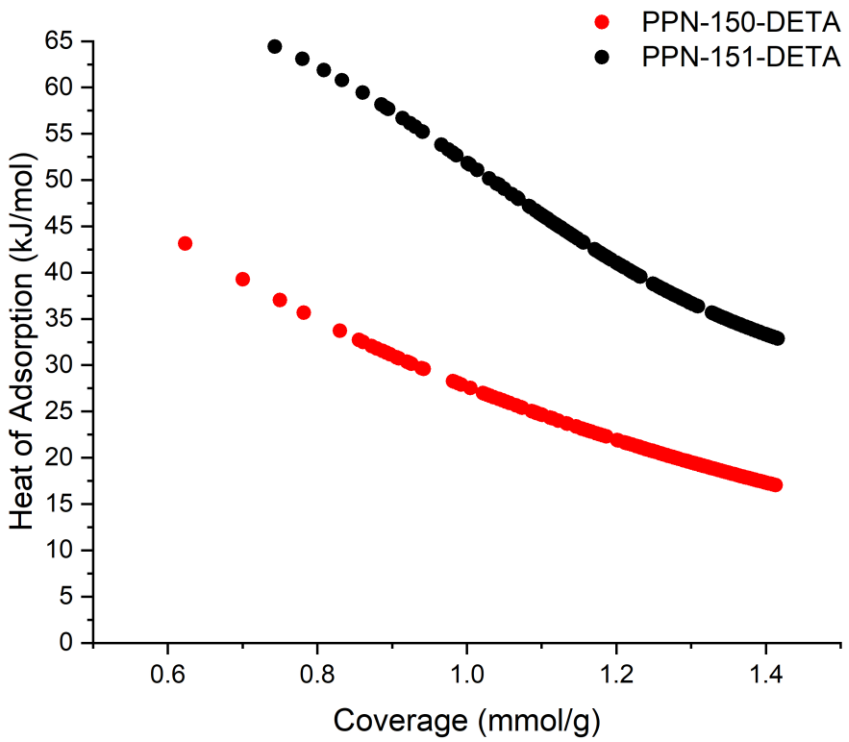

Figure 24. Heat of Adsorption as a function of coverage for PPN-150-DETA and PPN-151-DETA.

As another method of probing the effect cyanuric acid on the nature of CO_2 adsorption in PPN-151-DETA, *in situ* IR testing, during gas loading, was performed. The data for PPN-150-DETA showed a mix of phsysorptively (peak at 2334 cm^{-1}) and chemisorptively (broad shoulder at 1700 cm^{-1}) bound CO_2 in the form of carbamate (**Figure 25**). In contrast, the PPN-151-DETA results showed the dominant form of CO_2 in the sample was chemisorptively bound CO_2 (**Figure 26**). This data demonstrates that PPN-151-DETA may have a more efficient binding process for CO_2. This was correlated to the heat of adsorption data showing a much stronger initial binding of CO_2 to PPN-151-DETA as compared to PPN-150-DETA.

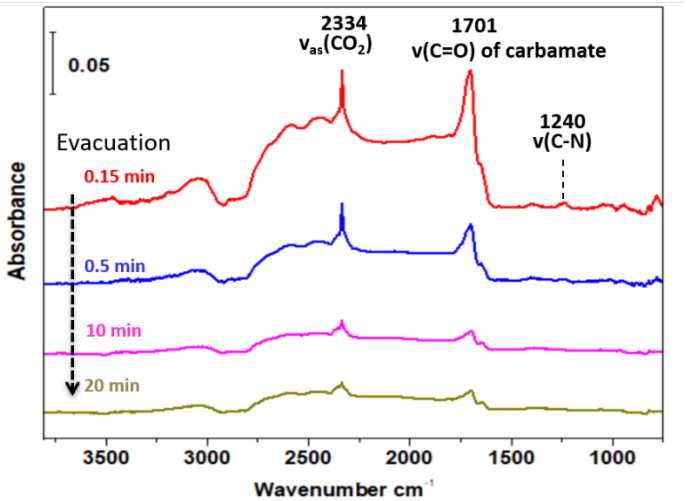

Figure 25. IR spectra of adsorbed CO_2 in PPN-150-DETA after loading CO_2 at 150 Torr and 40 ºC for ~5 min and subsequent evacuation of gas-phase CO_2. The molecularly adsorbed CO_2 at 2334 cm^{-1} can be only observed after evacuating gas-phase CO_2 since IR absorption of CO_2 gas at this pressure is prohibitively high (no signal on the detector), making it impossible to distinguish the adsorbed CO_2 from gas-phase CO_2.

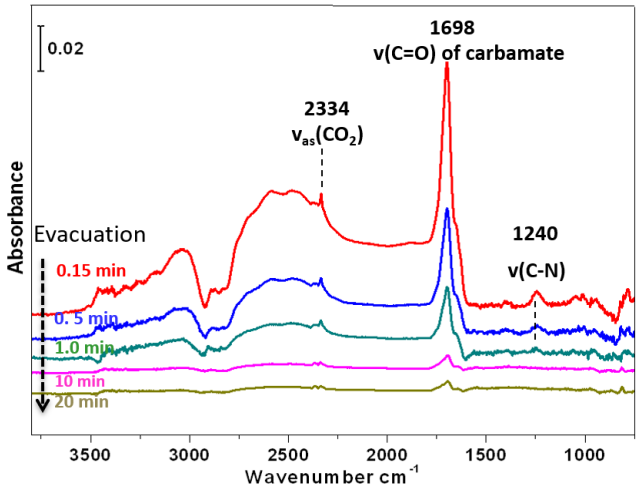

Figure 26. IR spectra of adsorbed CO_2 in PPN-151-DETA after loading CO_2 at 150 Torr and 40 ºC for ~5 min and subsequent evacuation of gas-phase CO_2.

As PPN-151-DETA was the most promising material, larger-scale fixed-bed adsorption testing was conducted using a Quantachrome DynaSorb BT in a breakthrough experiment.[245] In addition, PPN-150-DETA and PPN-152-DETA were also studied to

determine if there were any changes in adsorption behavior between TGA and breakthrough analysis (**Figure 27**). Additionally, the DynaSorb BT allowed for investigations of the cycling behavior under wet gas conditions. In this study, simulated flue gas containing 15% CO_2, 2% H_2O, and 83% N_2 was used to conduct these tests. During breakthrough testing, the sample was placed in an adsorber column, and the gas mixture was allowed to flow through the material. This flow-through set up allowed for more efficient and accurate adsorption and desorption as compared to the TGA cycling flow over setup. In the breakthrough experiment, a greater surface area of the material was available for both the adsorption gas stream and the regeneration gas stream.

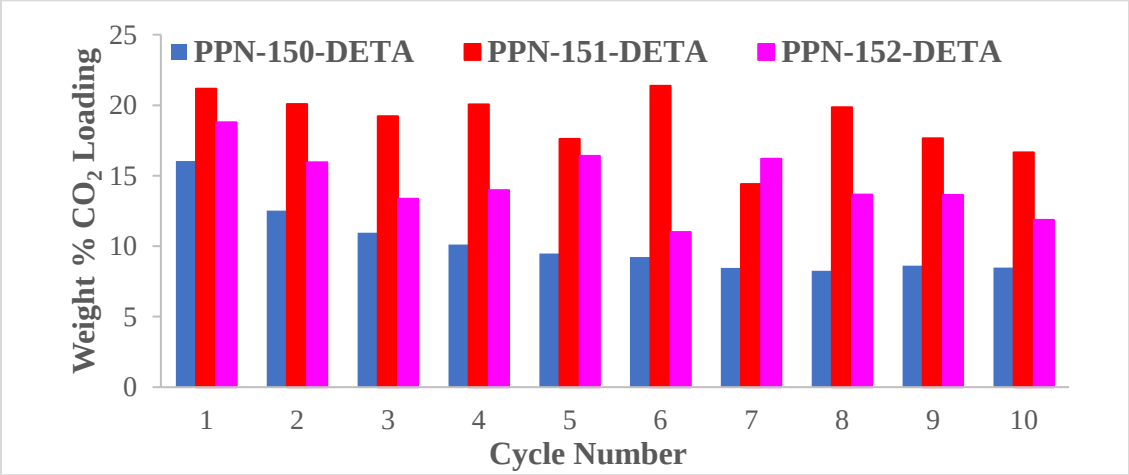

Figure 27. Breakthrough experiment for PPN-150-DETA, PPN-151-DETA, and PPN-152-DETA using a 15% CO_2, 2% H_2O, 83% N_2 gas mixture. Tests were performed using a 5 mL column containing approximately 1 g of loosely packed material.

Overall, the CO_2 uptake of the three samples increases under humid conditions compared to the dry gas adsorption tests. It is believed this occurred due to the improvements in the stoichiometry, where the amine: CO_2 ratio changes from 2:1 to 1:1, in the presence of moisture.[246] However, while this change in the material binding

stoichiometry would suggest that the material's uptake capacity should double, this does not take into account the actual working conditions of the breakthrough and TGA experiments. Specifically, they both operate under non-equilibrium conditions. Instead, they both operate under kinetically controlled conditions. As such, the material's real uptake capacity is limited by the ability of CO_2 to diffuse through the material. In particular, the presence of pools of DETA, a viscous liquid, could prevent CO_2 diffusion through the pores located deep within the material. As mentioned above, the BET surface area of the loaded PPNs tends to be significantly lowered compared to the unloaded PPNs. This reduction in surface area is likely the result of the DETA creating pools within the pores of the material. Under the N_2 sorption surface area measurement conditions (77 K), these pools create a solid layer of DETA, blocking N_2 access to the entirety of the internal surface area. Even under working conditions, 40°C, the viscosity of these DETA pools is likely to prevent CO_2 access under simple kinetic gas flow conditions.

PPN-151-DETA showed a massive improvement in performance under wet gas cycling conditions, achieving >20%wt CO_2 as compared to 9.46%wt under dry conditions. Under ideal conditions, the maximum achievable improvement in cycling performance should be 2x. The fact that the experiment resulted in a > 2x increase was indicative of either some improvement in the material efficiency going from TGA to breakthrough experimentation or an improvement in the number of available CO_2 binding sites. One possibility is that some portion of the DETA molecules cannot engage in CO_2 capture under dry conditions as they lack a second equivalent of DETA to act as a proton acceptor. This is corroborated by the heat of adsorption values for PPN-151-DETA, which were

calculated from the pure CO_2 isotherms. There was a 22 kJ•mol^{-1} (33.9%) reduction in the heat of adsorption, going from 64.8 kJ•mol^{-1} at 20 cm^3/g, to 42.8 kJ•mol^{-1} at 26.6 cm^3/g, which would suggest that there is a significantly lowered affinity towards CO_2 once the initial gas loading has occurred (**Figure 24**). For comparison, PPN-150-DETA at a broader range of coverage, 17.0 cm^3/g to 29.4 cm^3/g, only saw a reduction in the heat of adsorption of 7.6 kJ•mol^{-1}. However, the overall heats of adsorption for PPN-150-DETA are significantly lower, 28.9 and 21.3 kJ•mol^{-1} respectively, which corresponds to a 26.3% reduction in the heat of adsorption.

Breakthrough testing of PPN-150-DETA still shows a consistent loss in uptake capacity over many cycles. This was especially noticeable during the first six cycles, where PPN-150-DETA decreases from a 16.0%wt uptake to a 9.2%wt uptake. For comparison, PPN-151-DETA showed an uptake capacity of 21%wt at both cycle 1 and cycle 6. PPN-152-DETA had a highly variable uptake, going from 18.8%wt in cycle 1 down to 11.0%wt in cycle 6. Part of the issue with PPN-152-DETA was that the slow decomposition of hexamethylenetetramine (HMTA) under aqueous conditions resulted in a release of ammonia. The free ammonia could both act as an additional CO_2 chemisorptive species, and cause false-positive results for CO_2 binding in the DyanSorb BT instrument TCD.

Scale-up

In order to establish the industrial feasibility of PPN-151-DETA, we attempted to produce the material beyond the bench scale. In order to prevent precipitation of melamine-cyanurate before the initial polymer gel formation, the cyanuric acid-DMSO

solution had to be heated to the reaction temperature (150 °C for the bench-scale tests) and was added after the paraformaldehyde had desolved. Failure to properly heat the cyanuric acid solution or ensure the complete dissolution of the paraformaldehyde resulted in a loss of porosity in the final PPN. It should be noted that upon larger scale synthesis, the reaction time had to be increased. For a reaction batch at the 250 g scale, the highest PPN performance was produced after 6 days of reaction time (**Figure 28**). These results demonstrate that PPN-151-DETA can be utilized as a cost-efficient alternative for industrial post-combustion CO_2 capture.

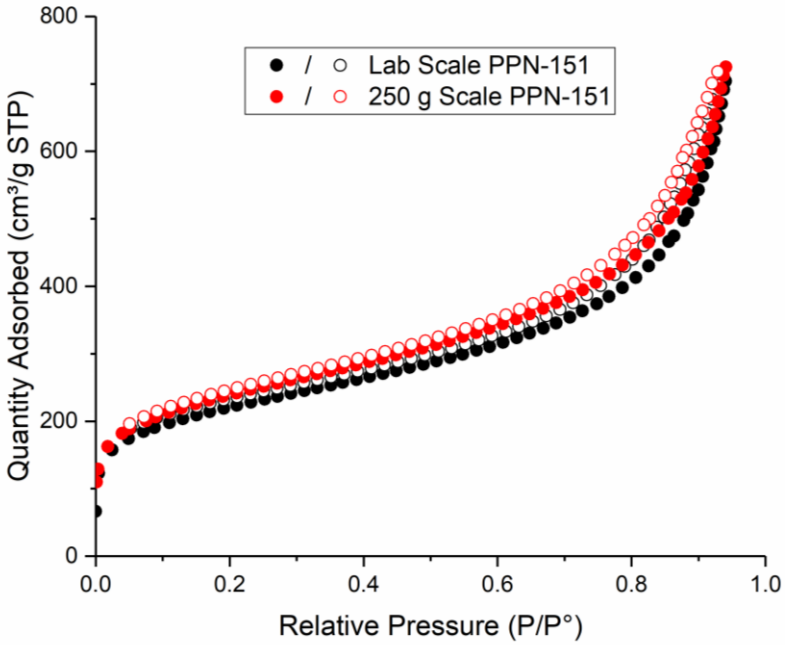

Figure 28. PPN-151 produced at the 250 g scale, giving a surface area of 853 m^2/g compared to a lab-scale sample of PPN-151, which has a surface area of 798 m^2/g.

Conclusion

Reported herein is a formulation for a family of post-combustion CO_2 capture materials, the PPN-150-DETA family. Each member of the PPN-150-DETA family is differentiated by the incorporation of a different dopant molecule within the PPN during the polymerization reaction. One dopant, in particular, cyanuric acid (PPN-151), demonstrated remarkable improvements in performance for PPN-151 as compared to the baseline PPN-150. The improvements for PPN-151 were a higher CO_2 heat of adsorption, improved cyclability, improved performance under wet gas conditions, and improved thermal stability. The post-synthetically incorporated amine, PPN-151-DETA, proved to be a promising commercially viable sorbent for post-combustion CO_2 capture.

CHAPTER III

METAL OXIDE DECORATED POROUS CARBONS FROM CONTROLLED CALCINATION OF A METAL-ORGANIC FRAMEWORK*

Introduction

Porous carbons have long been utilized for adsorption,[247] separation,[248] and catalytic applications.[249] Several different methodologies can be used for the generation of porous carbons, from the direct pyrolysis of an organic precursor such as biological waste products[250] or organic polymers,[251] to the chemical activation of a carbon precursor using a strong base.[252] In particular, metal oxide doped porous carbons have been used for many different catalytic transformations, such as alcohol oxidation,[253] the Fischer-Tropsch reaction,[254] and oxygen evolution.[255] The generation of these metal oxide doped porous carbon species has typically been achieved through post-synthetic growth or incorporation of metal nanoparticles within the carbon structure.[256] In these materials, the porosity of the carbon is either the result of a porous biological precursor, which often has a non-uniform range of porosities, or is dependent on the processing step, typically through chemical etching.[257]

*Reprinted in full with permission from Day, G. S.; Li, J.; Joseph, E.; Metz, P. C.; Perry, Z.; Ryder, M. R.; Page, K.; Zhou, H.-C., Metal Oxide Decorated Porous Carbons from Controlled Calcination of a Metal-Organic Framework. *Nanoscale Advances* **2020**. DOI:10.1039/C9NA00720B – Published by the Royal Society of Chemistry.

Metal-organic frameworks (MOFs) are a class of porous materials comprised of inorganic nodes, often referred to as secondary building units (SBUs), connected by organic linkers.[258] One of the main advantages of MOFs is that both their physical and chemical structures and functionalities can be tuned through simple ligand or metal modification. Such features are promising for many next-generation smart applications,[259] and have identified MOFs as particularly interesting materials for gas separation[90] and catalysis.[157] Additionally, the regular geometry of these compounds results in high levels of crystallinity and regularly shaped and organized pores.

Due to their tunable porosity and the presence of metal centers, there has been a growing interest in using MOFs as templates for the generation of porous carbons.[189] MOFdCs are typically produced via the direct calcination of MOFs in inert atmospheres like N_2,[260] Ar,[261] or He[262]. Carbonization offers many benefits for MOFs, the most obvious benefit being the increased hydrolytic stability compared to the parent MOF, allowing them to be utilized under aqueous conditions.[261] This improved stability, alongside their tunable structures, give MOFdCs the potential to be used as a replacement for standard porous carbons in areas such as water remediation[263] or chemical warfare agent degradation.[264] The ordered structure of MOFs also leads to the relatively facile formation of graphitic carbon, known for its electrical conductivity. This has resulted in many examples of MOFdCs being utilized in electrochemical applications such as the oxygen evolution reaction.[265] Additionally, there is an interest in dispersing metallic nanoparticles throughout a carbon scaffold to prevent sintering and maintain high chemical activity,[264] which MOFdCs excel at through their pre-dispersed metal SBUs.[266]

MOFs have long been used as gas storage materials due to their high surface areas, increasing accessible surface for the physisorption of gases.[90] The adsorption affinity and capacity are often dependent on the dimensions of the host/guest, such as the size of the gas molecule, pore window,[267] or the degree of polarizability.[268] As such, the use of different gases during calcination should result in varying degrees of gas adsorption and diffusion. While activation processes have been studied in the formation of activated carbons,[269] less research has focused on the effect of different gas environments on the formation of MOFdCs. In particular, it has been noted in the MOFdC literature that calcination conditions have an impact on the resulting pore structure.[270] However, there has yet to be a thorough systematic study of this process.

Results and Discussion

In this work, we have focused on a typical iron-containing MOF, PCN-250 (PCN = porous coordination network)[271] (also known as MIL- 127[272]), consisting of $Fe_3\mu_3O$ clusters and the ligand, 3,3',5,5'-azobenzenetetracarboxylate (ABTC), with the formula $C_{48}\ H_{28}\ Fe_6\ N_6\ O_{32}$, or $(Fe_3O)_2(ABTC)_3$. This iron-based MOF was of particular interest for carbonization due to the catalytic applications of iron oxide particles,[273-274] as well as the ease of separation afforded by the magnetic behavior of iron oxide.[261] PCN-250 has been well studied for gas storage and separation applications due to its accessible open metal sites.[271, 275] Open metal sites are utilized to improve the polarization of gas molecules within the MOF pores, improving the adsorption affinity of the gas species.[267] Improved gas adsorption affinity, results in an increased likelihood of adsorption events occurring

during calcination, which could result in variations in the pore structure of the final porous carbon.

Initial thermogravimetric analysis (TGA) of PCN-250 under air, N_2, and water-saturated N_2 determined the decomposition temperature of PCN- 250 to be between 350 to 450 °C, with partial dependence on the gas flow environment (**Figure 29**). Calcination under air results in the near-complete thermolysis of the ligand (76% of the total theoretical mass), while analysis under N_2 only results in a 25% mass loss upon decomposition at 450 °C, with a subsequent mass loss event occurring at 580-620 °C. Interestingly, when PCN-250 is decomposed in the presence of water vapor, the mass loss event at 620 °C results in what appears to be the complete pyrolysis of the ligand, with the final sample mass corresponding to that observed under air oxidation.

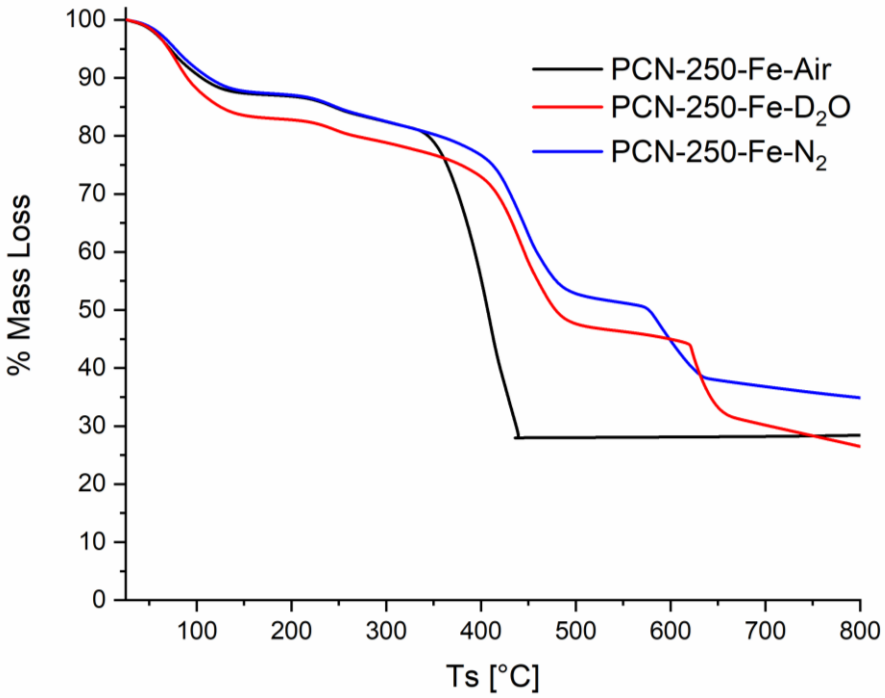

Figure 29. TGA curve of PCN-250 performed under a flow of air (black) water (D_2O) enriched N_2 (red) and N_2 (blue).

Based on the TGA results, we became interested in the gas flow-dependent decomposition of PCN-250 and decided to study the effect of gas environments on the material structure. We hypothesized that the different gas environments should result in highly differentiated pore structures when transformed into a MOFdC. To prevent complete loss of ligand-derived carbon upon carbonization, the samples were calcined at 500 °C for 4 hours under six different gas environments: air, N_2, He, water enriched N_2 (utilizing D_2O to prevent potential H incorporation for neutron diffraction experiments, 2% D_2O by volume), CO_2, and H_2 (5% in N_2).

Brunauer-Emmett-Teller (BET) adsorption analysis of each sample was conducted to confirm the effect the gas environments have on surface area (**Figure 30**). In general, the calcined samples have lower BET surface areas compared to uncalcined PCN-250

(approximately 1500 m^2/g),[271] with the air calcined samples showing the smallest BET surface area, 9 m^2/g, and the He calcined sample showing the highest BET surface area, 265 m^2/g. In agreement with our initial hypothesis, the surface area has a strong correlation with the residual carbon content in the material (**Table 5**). The surface area of the samples were found to correlate linearly with the carbon content,giving a correlation coefficient (R^2) value of 0.93129 (**Figure 31**). The R^2 value improves to 0.98115 if the data for the D_2O sample is removed as an outlier (**Figure 32**).

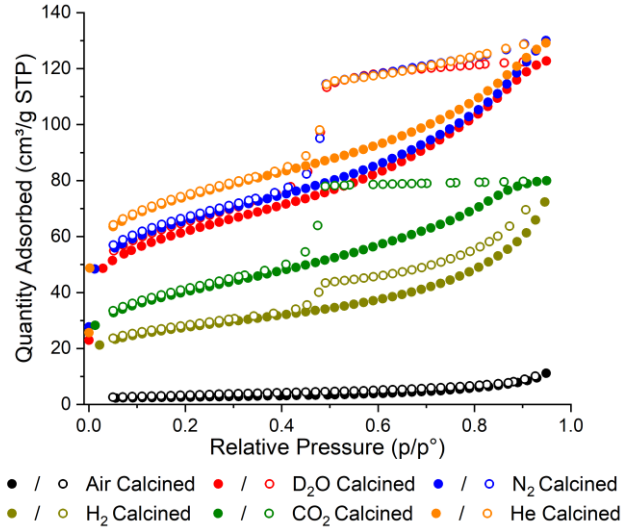

Figure 30. N_2 adsorption isotherms of the calcined PCN-250 samples showing alterations in total capacity and pore shapes via calcination gas environment.

Table 5. Elemental Analysis of PCN-250 Calcined at 500 °C Under Various Conditions.

Atmosphere	C (wt%)	H (wt%)	N (wt%)
Air	0.15	0.0	0.0
H_2	7.50	0.60	1.04
D_2O	31.61	1.91	5.28
CO_2	16.65	0.73	3.08
N_2	24.25	1.47	3.62
He	30.24	1.25	3.09

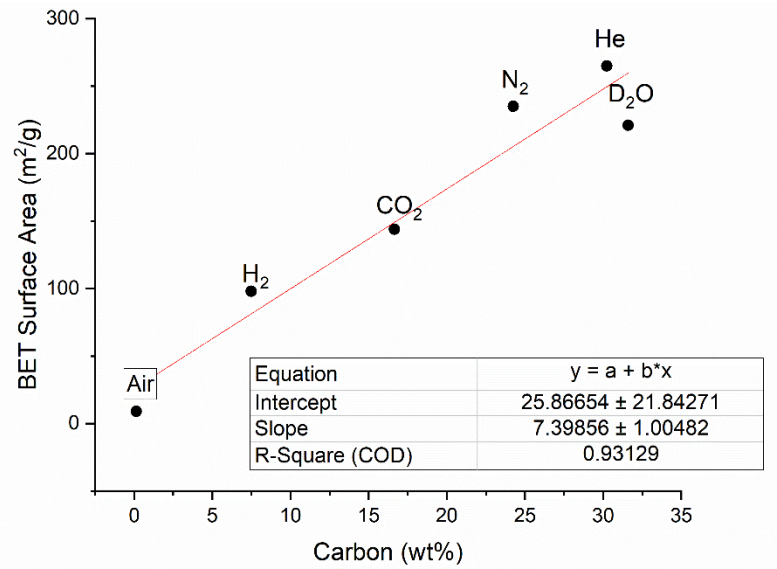

Figure 31. BET Surface area versus the residual carbon content of the MOF derived carbons, showing an excellent linear correlation between the two parameters.

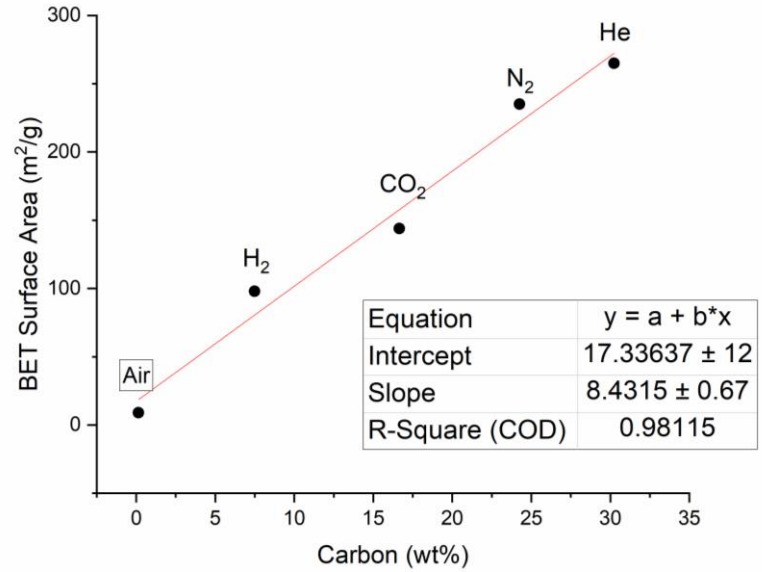

Figure 32. BET Surface area versus the residual carbon content of the MOF derived carbons with the D_2O calcined sample being excluded, exhibiting a higher degree of correlation amongst the data points.

The carbon content for the D_2O calcined sample is the highest, despite only having the third-highest surface area (221 m^2/g). This could be due to the D_2O labilizing the metal-carboxylate bonds during the heating phase of the calcination, due to a competive

ligand exchange, forming a partially amorphous MOF structure that possesses a lower surface area before carbonization. This pre-carbonization amorphization likely prevents off-gassing during carbonization, causing some of the ligand to beecome trapped within the structure. The presence of organics is corroborated by the higher hydrogen and nitrogen content in the D_2O sample (1.91 and 5.28%, respectively (**Table 5**). The nitrogen contained in the azobenzene bridge of the ligand is well known for readily eliminating N_2 well below 500 °C,[276] which suggests that the remaining nitrogen content within the MOFdCs is due to poor heat transfer within the porous structure, preventing carbonization of some of the interior ligands. To test this hypothesis, we performed additional experiments looking at the collapse of PCN-250 under water-rich streams at lower temperatures. Compared to heating under N_2, there was an increased degree of amorphization under water at 250, 275, and 300 °C (**Figure 33**). When PCN-250 was heated under water at 300 °C for 16 h there was negligible crystallinity remaining in the sample, while heating under N_2 still showed characteristic peaks for PCN-250.

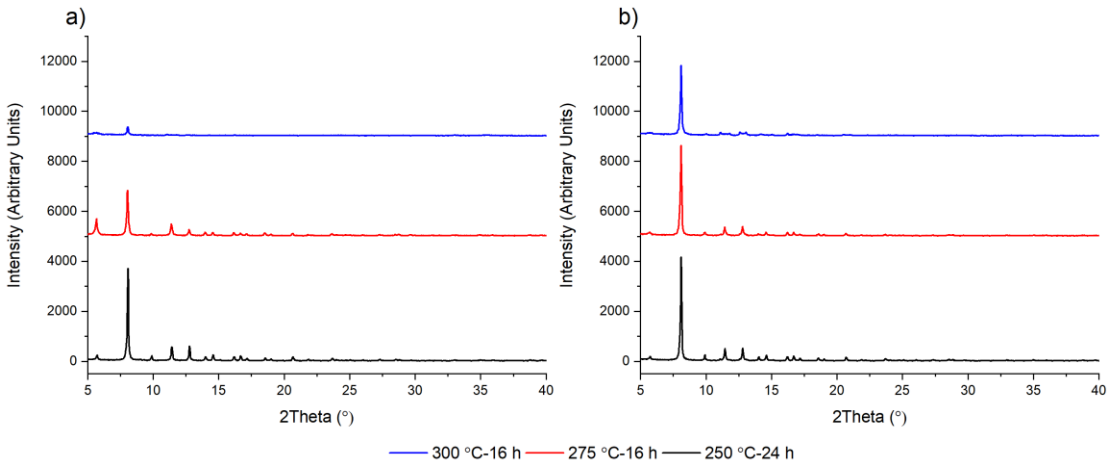

Figure 33. PXRD patterns for PCN-250 calcined at low temperatures under a) water and b) N_2. The heating temperatures and times were kept consistent between the two sets of samples.

The samples of PCN-250 exhibit a large hysteresis at when the relative pressure, p/p^0, is greater than 0.4, which is representative of mesoporous structures within the material. The generation of a 38 Å mesopore within PCN-250 has been previously reported,[275] whichmatches the pore size distribution of the calcined PCN-250 samples reported here (**Figure 34-35**). The N_2 and the He calcined samples show broadly similar isotherms, suggesting a similarity in the environments generated by these gases during calcination. Interestingly, the D_2O in N_2 calcined sample also shows a similar isotherm to that produced by N_2 and He, which suggests that the concentration of D_2O in the sample during calcination is low enough to not significantly impact the overall carbon superstructure, despite the differences in total carbon content. However, this same phenomenon is not observed with the sample calcined in the presence of 5% H_2 in N_2, which shows a significant reduction in the BET surface area, 98 m^2/g.

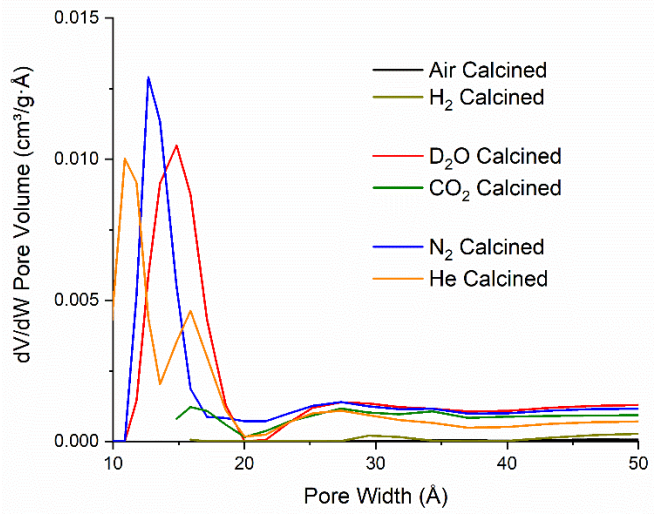

Figure 34. BJH Pore size distribution data for the PCN-250-derived carbons showing a change in the degree of mesoporosity between the different samples.

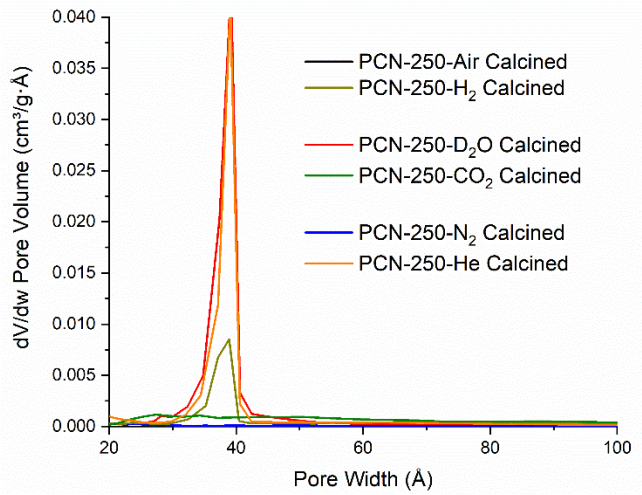

Figure 35. DFT Pore size distribution of the PCN-250-derived carbons. Only the D_2O in N_2, N_2, and He calcined samples show significant levels of microporosity remaining.

Despite the differences in sample porosity, the morphologies of the individual samples are similar, maintaining the relative shape of PCN-250 as seen through scanning electron microscopy (SEM) images (**Figures 36-38**). The air calcined sample shows the most substantial deviation from the shape of pre-treated PCN-250, with large cracks and channels observed in the material (**Figure 37**). The other samples all show similar contraction on a few of the crystal faces and corresponding concavity to the crystal edges. These strains induce the formation of a wave-like pattern on the faces of most of the crystals, with the effect being most evident for the CO_2 calcined sample (**Figure 38**).

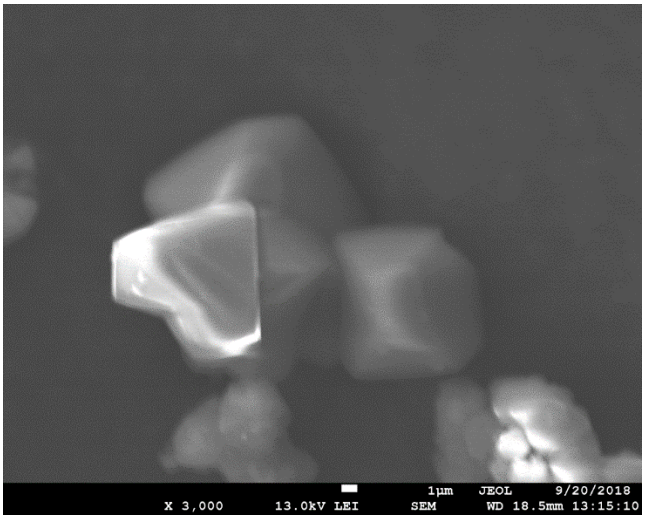

Figure 36. SEM of the as-synthesized PCN-250.

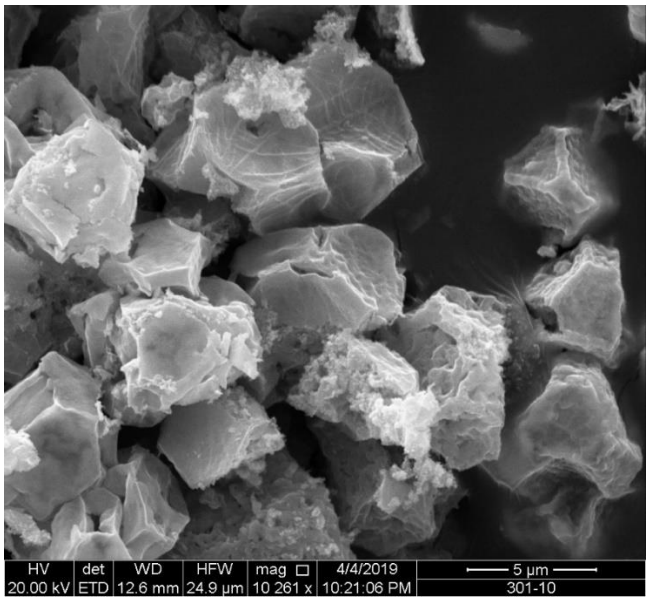

Figure 37. SEM of the air calcined PCN-250.

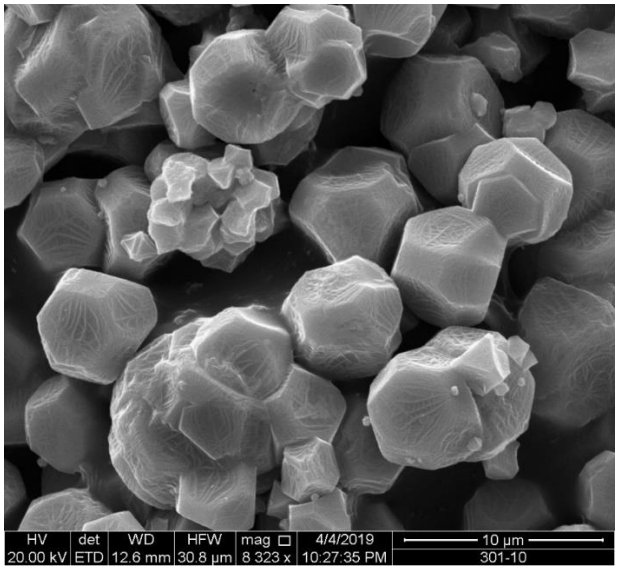

Figure 38. SEM of the CO_2 calcined PCN-250.

As PCN-250 contains iron-based SBUs, we were interested in probing the presence and phases of the resulting Fe nanoparticles within the samples. Powder X-ray diffraction (PXRD) data were collected using a Bruker D8 diffractometer equipped with Cu Kα radiation.The six samples showed that in addition to altering the porous carbon structure of the material, calcination under different gas environments resulted in the generation of various iron oxide phases and variation in crystallite domain size (**Figure 39**). Analysis of the iron oxide domains was performed via Rietveld refinement of the experimental data using known iron oxide structures, and the software package GSAS II.[277] The unit cell parameters, the atomic displacement and position parameters of the atoms, and the crystallite size of the iron oxide phases were refined. All samples were initially modeled as a mixed-phase system consisting of both iron (II,III) oxide and iron (III) oxide, with subsequent single-phase fits performed on those data showcasing zero contribution from

a second phase. As expected, calcination under air results in the complete formation of the fully oxidized iron (III) oxide, Fe_2O_3 (**Figure 39a**).

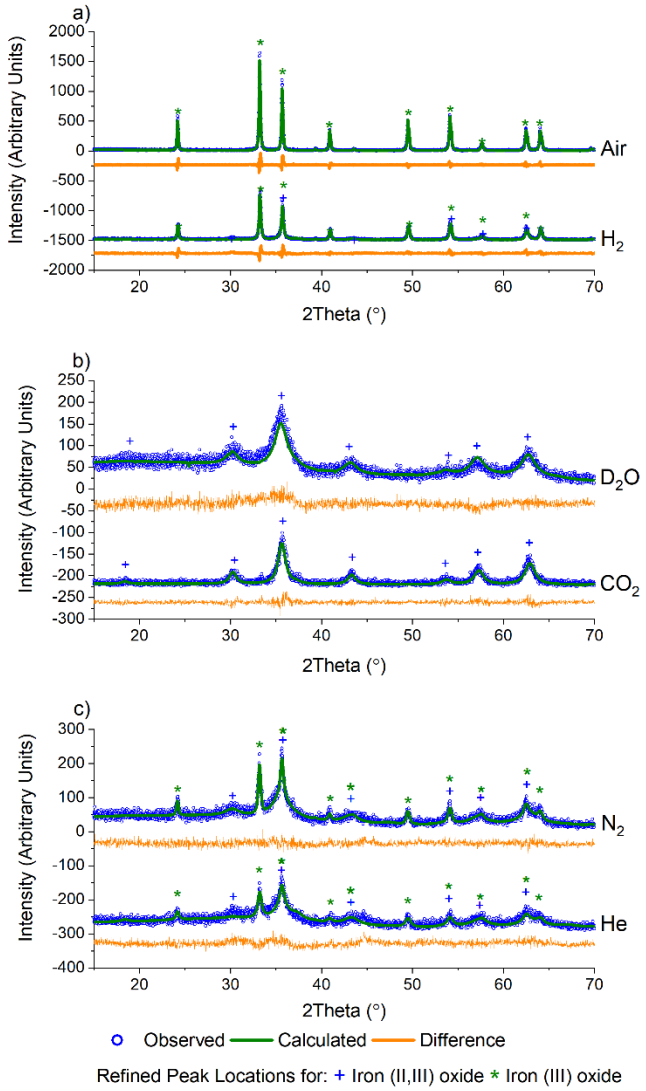

Figure 39. PXRD of PCN-250 samples calcined under different gas flow environments showcasing the formation of both iron (II,III) oxide and iron (III) oxide based on gas environment.

Interestingly, Rietveld refinement of the H_2 calcined sample (**Figure 39a**, bottom) gave an iron (III) oxide phase fraction of 81.5(7)% with a balance of 18.5(14)% being iron

(II,III) oxide by mass (**Table 6**). The sample visibly glowed as it was exposed to air after cooling to room temperature, which suggests that oxide formation does not occur during the calcination process, but only upon exposure to air.

Table 6. PCN-250 Samples Calcined at 500 °C Under Various Conditions.

Atmosphere	BET Surface Area (m^2/g)	Pore Volume (cm^3/g)	Iron (II,III) oxide fraction (%)	Iron (III) oxide fraction (%)	Iron (II,III) oxide size (nm)	Iron (III) oxide size (nm)
Air (X-ray)	9	0.017	0	100	N/A	132.9(19)
Air (Neutron)	—	—	0	100	N/A	99(9)
H_2 (X-ray)	98	0.112	10.69	89.31	25(11)	88.4(20)
D_2O (X-ray)	221	0.190	100	0	6.2(6)	N/A
D_2O (Neutron)	—	—	100	0	19.9(7)	N/A
CO_2 (X-ray)	144	0.124	100	0	13.5(11)	N/A
N_2 (X-ray)	235	0.201	55.7	44.3	5.2(6)	210(190)
N_2 (Neutron)	—	—	34.68	65.32	15.2(5)	330(200)
He (X-ray)	265	0.200	46.47	58.53	19(12)	70(40)

Exposure to oxygen atom-containing gases such as D_2O and CO_2 did not result in iron (III) oxide, but formed the mixed valent iron (II,III) oxide, as confirmed via Rietveld refinement (**Figure 39b**). This is likely due to the poorly oxidizing nature of the two molecules, which, while introducing oxygen atoms to the metal clusters of PCN-250, do not have the oxidation potential to produce iron (III) oxide. Initial refinement using standard iron (II,III) oxide resulted in a poor fit, with the intensity ratio of the (113) to (022) peaks (35.8 and 30.3° 2θ) differing significantly from that seen in the bulk material. The fit quality was substantially improved by using a model with cation deficiencies in the structure, with a iron occupancy of 0.982 in the tetrahedral site and 0.974 in the

octahedral site.[278] The refined iron (II, III) oxide crystallite sizes are less than 20 nm (**Table 6**), likely due to the conditions invoked through confinement in the MOF-derived graphitic scaffold, and with the milder oxidation preventing the sintering observed with iron (III) oxide.

Meanwhile, after calcination under an inert atmosphere, the resulting material was also observed to oxidize in air at room temperature. Interestingly, while H_2 calcined PCN-250 mainly resulted in the formation of iron (III) oxide, the N_2 and He calcined samples resulted in a more even mixture of the two iron oxide phases. The N_2 calcined sample resulted in 70.5(2)% iron (II,III) oxide and 29.5(10)% iron (III) oxide by mass (**Figure 39c**, top), while the He calcined sample resulted in 62(4)% iron (II,III) oxide and 37.7(22)% iron (III) oxide (**Figure 39c**, bottom) according to Rietveld refinement of the laboratory PXRD patterns (**Table 6**).

Rietveld refinement on the PXRD of the six samples also revealed information regarding trends in the crystallite size of the iron oxide phases. In general, the iron (III) oxide phases, when present, appeared to be larger than those of the iron (II,III) oxide. The iron (III) oxide crystallite phases range in size from 70 nm in the He calcined sample to 210 nm in the N_2 sample. Both air and N_2 calcination resulted in the formation of iron (III) oxide domains greater than 100 nm.

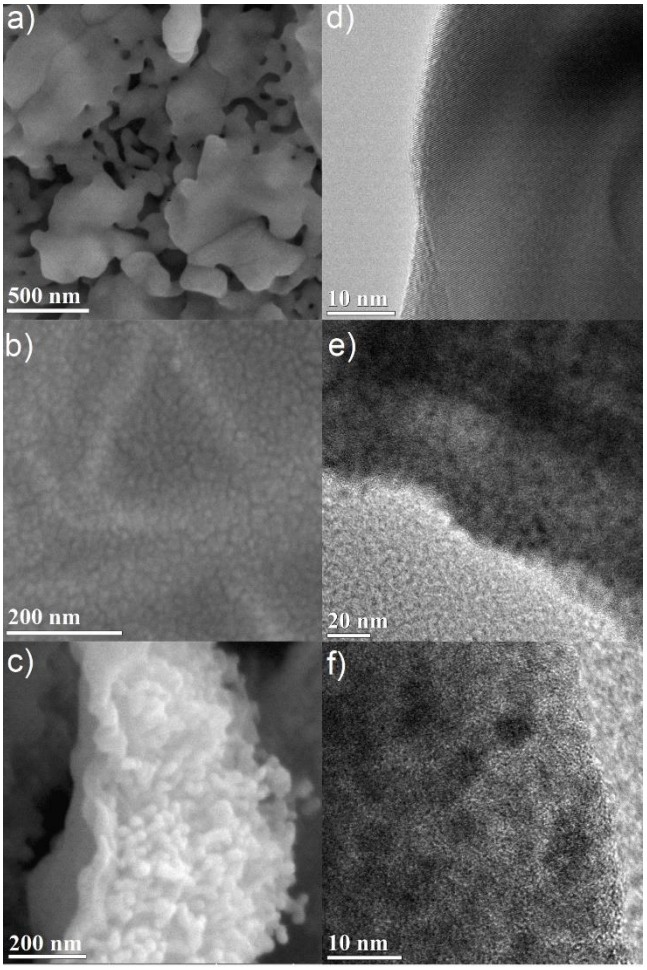

Figure 40. High-Resolution SEM of a) air, b) D_2O, and c) N_2 calcined samples. TEM images of d) air, e) D_2O, and f) N_2 calcined samples.

Transmission electron microscopy (TEM) images of both the air calcined (**Figure 40a**) and the N_2 calcined (**Figure 40**) samples both show the presence of bulk iron (III) oxide. Meanwhile, both the He calcined (**Figure 41**) and the H_2 calcined (**Figure 42**) samples have poorly discernible features, with no apparent signs of bulk iron oxides, nor nanoparticle oxides. This is suggestive of the highly mixed and intermediate ranged size of the iron oxide nanoparticles, which corresponds with the size values determined by PXRD Rietveld refinement. The iron (III) oxide particles are less than 100 nm (88.4(20)

nm and 70(40) nm for H_2 and He respectively), and the iron (II,III) oxide particles are greater than 10 nm (25(11) nm and 19(12) nm for H_2 and He respectively), corroborating the TEM images.

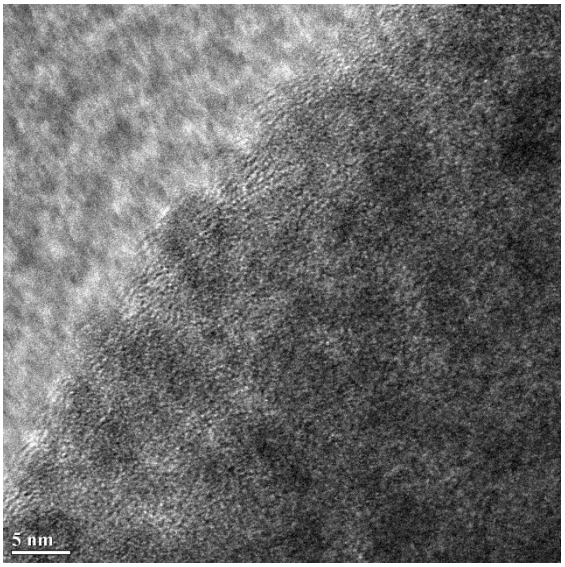

Figure 41. TEM of PCN-250 calcined under He.

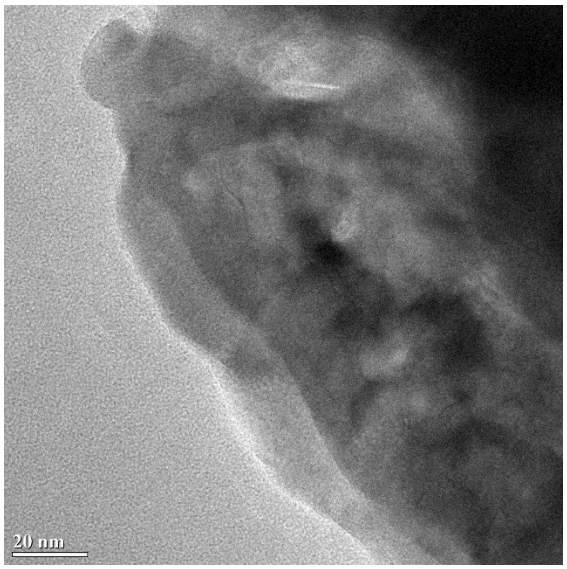

Figure 42. TEM of PCN-250 calcined under H_2.

Further insight into the bulk carbon structure of the materials was achieved via high magnification images using a high-resolution SEM. The SEM images show the

presence of nanoscale features, typically in the form of approximately 20 nm nodules (**Figure 40b-c**). The nodules are readily apparent alongside the surface wave-like pattern, suggesting that the physical strain introduced during the nodule formation is likely responsible for the bulk wave-like pattern on the surface of the material (**Figure 38**). These nodules are present in all the materials except for the air calcined sample (**Figure 40a**). As the air calcined PCN-250 has limited carbon content, these nodules are likely at least partially due to the residual carbon within the remaining samples. In the air calcined sample, there instead appear to be 20-100 nm holes formed due to the complete pyrolysis of the ligand, which correlates well with the small observed level of mesoporosity in the air calcined sample.

Samples previously calcined under air, D_2O, and N_2 were studied via neutron diffraction and total scattering at the Nanoscale Ordered Materials Diffractometer (NOMAD)[279] beamline of the Spallation Neutron Source (SNS) at Oak Ridge National Laboratory (ORNL) to enable pair distribution function (PDF) analysis. Analysis of the Bragg diffraction peaks in the three samples was performed via the same Rietveld refinement methods described for the laboratory PXRD data (Table 1). Both the air and the D_2O calcined samples still only showed the presence of a single iron oxide phase, iron (III) oxide and iron (II,III) oxide, respectively. Similar to the laboratory PXRD data, the D_2O data was also best fit to an iron (II,III) oxide structure containing cationic vacancies.[278] Both data sets show a similar trend to the lab-scale data, with the iron (III) oxide crystallites being significantly more substantial and the iron (II,III) oxide crystallites tending to be smaller, with some minor variation between the two sets of refinements.

Analysis of the Bragg diffraction of both the air and the D_2O calcined samples also showed significant magnetic diffraction peaks (**Figures 43-45**).

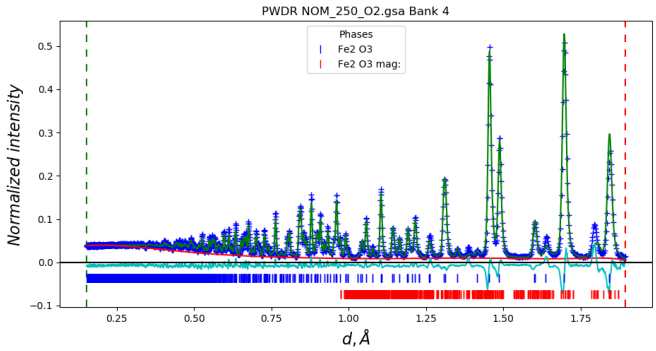

Figure 43. NOMAD bank 4 Rietveld refinement of the neutron Bragg peaks for air calcined PCN-250, containing both magnetic and nuclear components.

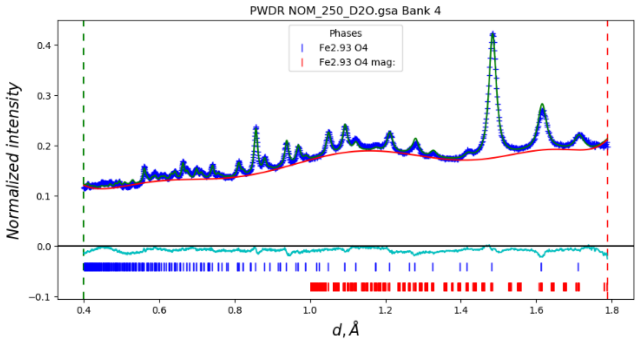

Figure 44. NOMAD bank 4 Rietveld refinement of the neutron Bragg peaks for D_2O calcined PCN-250, containing both magnetic and nuclear components.

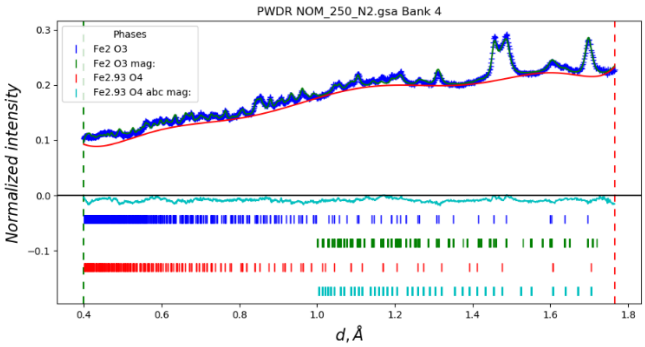

Figure 45. NOMAD bank 4 Rietveld refinement of the neutron Bragg peaks for N_2 calcined PCN-250, containing both magnetic and nuclear components.

The neutron diffraction data of the N_2 calcined sample still exhibits a mixture of iron (II,III) oxide and iron (III) oxide. However, the ratio of the two phases differs significantly, with the neutron data refining to 46.4(14)% and 53.6(16)% for iron (II,III) oxide and iron (III) oxide, respectively. Most likely, this is the result of a sampling error, with the sample not being in the same condition for both laboratory PXRD and neutron diffraction analysis. The significant estimated standard deviation in the iron (III) oxide domain size is likely due to the polydisperse distribution of crystallites within the N_2 calcined sample, with both bulk and nanoparticle domains observed in the TEM (**Figure 46-47**).

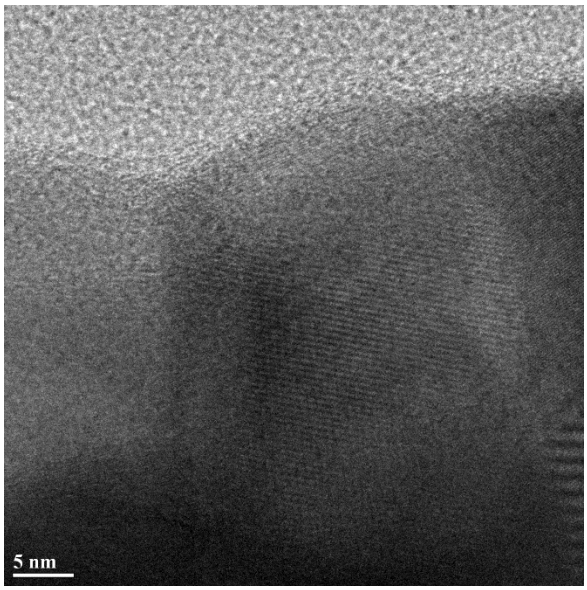

Figure 46. TEM of PCN-250 calcined under N_2 showing bulk iron oxide particles.

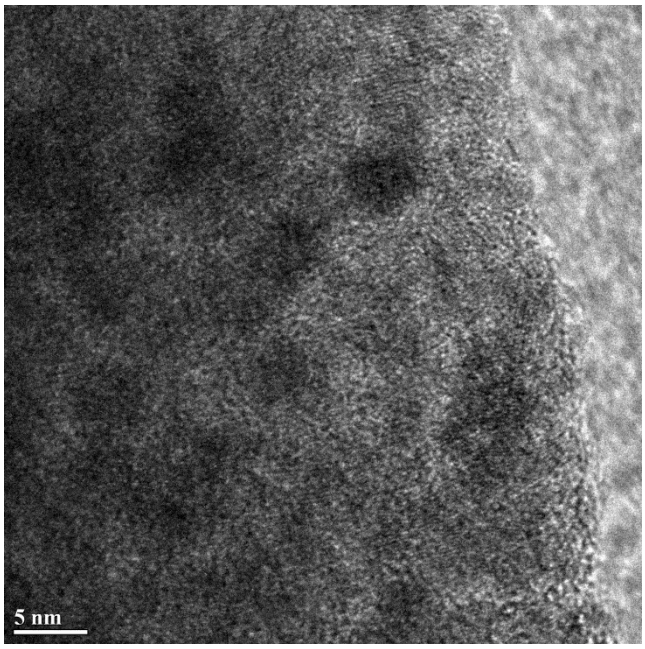

Figure 47. TEM of PCN-250 calcined under N_2 showing nanoscale iron oxide particles.

PDF fits of the three samples were performed using PDFgui.[280] Each data set (**Figure 48**) shows raw data (blue circles), the oxide fit (red line), the graphite fit (green line), the mPDF fit (orange line), with the final difference curve shown below (purple line) the noise present in the data is removed via a 100 point 3rd order polynomial Savitzky-Golay smoothing function performed on the residual curve. All three graphs are shown at different scales for clarity.

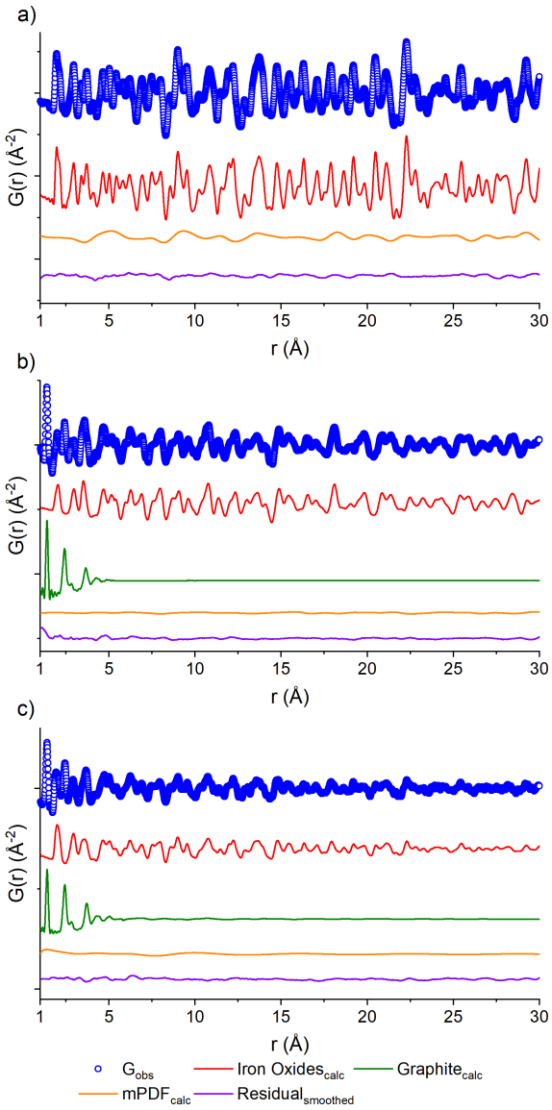

Figure 48. PDF of the neutron scattering data for PCN-250 calcined under a) air, b) D_2O, c) N_2. Each data set shows raw data (blue circles), the oxide fit (red line), the graphite fit (green line), the mPDF fit (orange line), with the final difference curve shown below (purple line) the noise present in the data is removed via a 100 point 3rd order polynomial Savitzky-Golay smoothing function performed on the residual curve. All three graphs are shown at different scales for clarity.

The nuclear component of the iron oxide PDF data for the three samples was fit with the unit cell parameters, atomic thermal parameters, the linear atomic correlation factor, and the empirical spherical particle size were refined. The air calcined sample was

in reasonable agreement with iron (III) oxide, corroborating Rietveld analysis (**Figure 48**). The main component of the difference curve of the air calcined sample appeared to be due to a broadly oscillating curve, which is characteristic of magnetic scattering. To confirm this, we fit the difference PDF using the magnetic pair distribution function (mPDF) method developed by Frandsen and Billinge[281-282] in Diffpy-CMI.[283] The mPDF was modeled using the known magnetic structure of iron (III) oxide,[284] consisting of spins ferromagnetically aligned within the plane, but antiferromagnetically aligned between adjacent planes of the iron sublattice. Both the paramagnetic scale factor and the scale factor for the overall mPDF function were refined. The difference curve after the refinement of both the nuclear and magnetic PDF is minimal (**Figure 48a**). This suggests that the residual carbon content of the air calcined sample is low, matching well with the elemental analysis data, with the air calcined sample only containing 0.15% carbon by mass (**Table 5**).

The nuclear component of the PDF for the D_2O calcined sample (**Figure 48b**) was modeled using iron (II,III) oxide and graphite. The residual after fitting the nuclear component is relatively small, but with a periodic oscillation related to the magnetic correlations of iron (II,III) oxide. The inverse spinel structure of iron (II,III) oxide consists of iron (III) in the tetrahedral positions and mixed iron (II) and iron (III) in the octahedral positions. The spins of the tetrahedral sites align antiferromagnetically with the spins of the octahedral sites. The overall imbalance in the spin magnetic moment due to the differences in site numbers and oxidation states account for the ferrimagnetic properties of iron (II,III) oxide.[285] The mPDF was again fit against the nuclear difference PDF

(**Figure 48b**) using a spin configuration determined from the literature.[285] As the iron oxide crystallite size is much reduced and the percentage of carbon is vastly increased in the D_2O sample compared to the air calcined sample (31.6% versus 0.15%), the overall contribution from magnetic scattering is less apparent.

Meanwhile, the PDF of the N_2 calcined sample data (**Figure 48c**) was fit to three-phase mixture of iron (II,III) oxide, iron (III) oxide, and graphite, with the residual consisting of the magnetic scattering from both iron (II,III) oxide as well as iron (III) oxide. The nuclear and the magnetic PDFs were modeled with a mixture of the two iron oxide phases, with the scale factors for the contributing phases refined. The initial analysis does not show any alteration to the two magnetic structures, both the iron (III) oxide and the iron (II,III) oxide spins are the best fit using the antiferromagnetic and ferrimagnetic structures mentioned previously. The current work is not focused on the exact variation between the local magnetic structure and that of the bulk phase materials, but this concept will be investigated as part of future work.

The carbon component of the D_2O and N_2 samples were both fit to graphitic carbon. Previous studies into MOF carbonization have shown that MOFdCs, especially those using aromatic ligand units, tend to have a high degree of graphitization.[286] Observation of the PDF of the D_2O and N_2 samples showed the presence of a large peak at 1.4 Å, which is indicative of the sp^2 C-C bond in graphitic carbon,[287] further supporting the identification of the carbon phase in these materials as graphitic.

The domain size of the carbon scaffold was modeled in PDFgui using an empirical spherical shape function for the graphite phase.[288] Both the D_2O and the N_2 data only show

carbon correlations out to near 5 Å. When refined through the entire range of 1-30 Å, the D_2O domain size settles on 5.28 Å while the N_2 only refines out to the slightly larger 5.76 Å. However, constraining the domain size and refining the two samples from 5.3 to 15 Å does suggest some minor contribution from the graphite phase in the N_2 sample, with the scale factor for graphite being 0.019 as opposed to 0.0023 for the D_2O sample. To accurately visualize the longer-range component as well as differences in the degree of order between the two samples, the 1-5 Å and the 5-15 Å fits of both the N_2 and the D_2O data were graphed together with the N_2 data scaled such that the intensity at the 1.4 Å peak matches that of the D_2O data (**Figure 49**). The image shows the higher relative intensities for the N_2 fit at 2.42, 3.7, 4.26, and 5.1 Å, which shows the higher degree of structural order in the N_2 sample relative to the D_2O sample, which correlates well with the difference in porosity and elemental analysis data. To best illustrate this relationship, we opted to take the difference of the D_2O graphitic curve from the scaled N_2 graphitic curve (orange line in **Figure 49**), which shows some possibility of minor features at distances greater than 5 Å visible as small humps or waves. By comparing the position of these waves to that of the peaks in a calculated bulk graphite PDF, we can observe that the waves of the N_2 do correspond in location with the graphite peaks at 7.1 8.25 and 10.8 Å, suggesting that the N_2 data does have a minor amount of larger-scale graphitic components.

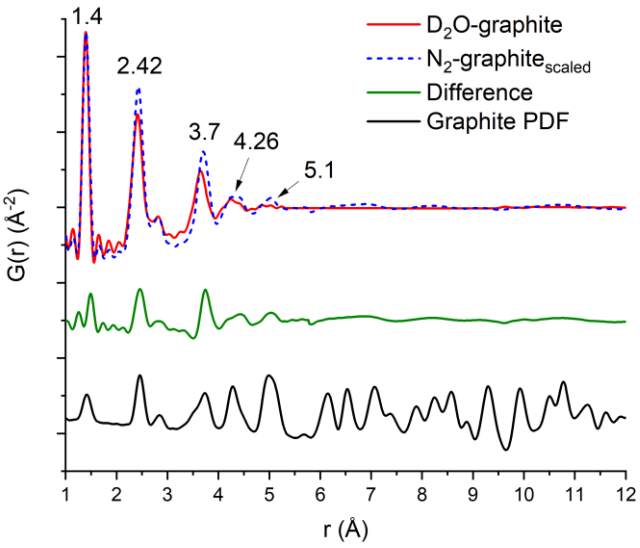

Figure 49. Overlap of the D_2O (red line) and N_2 (blue dashes) with the N_2 scaled so the first peak (1.4 Å) matches that of the D2O, a difference curve (orange) which is taken as the D_2O graphitic curve subtracted from the scaled N_2 curve is shown below. At the bottom is a calculated PDF for the graphitic carbon phase utilized for the PDF fitting.[289] The overall range of the order between the two matches well out to 4.2 Å. The N_2 calcined sample has a greater degree of order at the intermediate ranges (2.42 and 3.66 Å) and shows greater order at 5.1 Å, with minor broad features from 6 Å and beyond.

The first three C-C peaks (1.4, 2.42, and 2.84 Å) correspond to standard graphitic carbons.[287] The peak at 1.4 Å corresponds to the bond between two sp^2 hybridized carbons, the peak at 2.42 Å corresponds to the distances between meta oriented carbon atoms in hexagonal carbon moieties, and the peak at 2.84 Å corresponds to the para-para distance in graphitic carbon.[287] In keeping with the general trend of longer-range order observed in the N_2 sample, we also observed an increase in relative order in the short-range peaks of the graphitic PDF by observing the alteration in the peak intensity ratio at low r. The D_2O calcined sample has an intensity ratio of 2.05 for the 1.4 to 2.42 Å peaks, while the N_2 calcined sample has an intensity ratio of 1.57. This suggests that there is a higher degree of simple C-C sp^2 hybridized bonds in the D_2O calcined structure compared to complete

C_6 units. This can be visualized by observing the difference in the scaled N_2 compared to the D_2O at 2.42 Å (**Figure 49**), as there is a noticeable peak there, which corresponds to the higher relative number of units in the N_2 sample. This result corresponds well with the porosity and surface area of the D_2O calcined sample, which is noticeably lower than that of the N_2 calcined sample despite having a more substantial carbon content. The increased carbon content is likely due to the amorphous collapse of the carbon domains, which has limited the ability of the material to maintain a porous structure.

Meanwhile, the N_2 calcined sample has a higher degree of complete C_6 units relative to its carbon content, explaining its higher porosity and surface area. The structural collapse induced by D_2O exposure is likely due to the competition between the D_2O and the MOF ligand, ABTC, to bind to the iron centers in PCN-250. This competitive delegation could potentially cause an initial loss of order within the D_2O structure ahead of carbonization. Results from bulk testing under water vapor conditions have shown that a complete loss of crystallinity does occur before thermal decomposition, which does suggest that small scale nanoscale amorphization could be potentially occurring during standard calcination experiments (**Figure 33**). This partial collapse could also be partially insulating for the interior of the material upon calcination, as the D_2O not only has the highest carbon content (31.61% by weight) but also the highest hydrogen content at 1.91% by weight, which is significantly higher than the next highest sample, the N_2 calcined sample at 1.47%. This is likely due to incomplete carbonization of the interior structure during calcination, aided by the insulating nature of the pre-amorphized ligand under D_2O conditions.

To probe the oxide species that form under inert gas flow, we conducted in situ variable temperature PXRD analysis under He and N_2 flow (**Figure 50**). Unfortunately, due to safety concerns and instrument limitations, we were unable to conduct the same calcination in the presence of H_2. Upon heating to around 450 °C, there is a complete loss of crystallinity in the sample as it appears to lose the last remnants of MOF structural stability. After this loss of stability, the only peaks that are present are due to the alumina sample holder utilized for these experiments. However, in the N_2 calcined sample, at 550 °C, a new phase, Fe(0), starts to grow in (marked with a black rectangle in **Figure 50a**). This Fe(0) phase grows in intensity as the temperature is ramped to 700 °C. We were also able to observe the Fe(0) phase when the sample was held at 500 °C for 2 h, which is similar to the 4 h calcination condition used for the bulk sample prep (**Figure 51**). For comparison, holding the sample at 500°C under He for 4 h produced no noticeable growth of Fe(0), although eventual increase was observed once the sample reached 700 °C after having been previously held at 500 °C for 4 h and 600 °C for 2 h (**Figure 52**). As a control, we also performed the same variable temperature program under UHP Ar gas. The results show similar behavior to the He calcination, with a small growth of Fe(0), although the intensity of the phase peaks is generally quite low under Ar as well (**Figure 53**). Based on these results, we hypothesized that the formation of Fe(0) was due to the presence of N_2 and that the formation of Fe(0) under He and Ar could be the result of N_2 impurities, with the UHP cylinder utilized having 5 ppm N_2, although the UHP Ar utilized did not list any N_2 content, although it cannot be discounted at present. Interestingly, performing the same

200 °C to 700 °C in situ experiments using the isolated $Fe_3\mu_3O$ cluster under both N_2 and He did not result in the formation of any crystalline species (**Figure 54**).

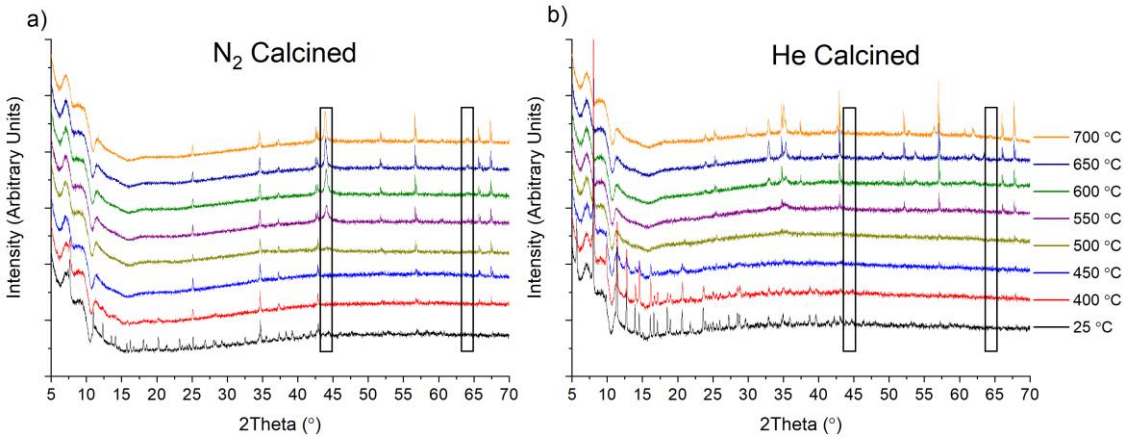

Figure 50. a) In situ variable temperature PXRD under N_2, b) in situ variable temperature PXRD under He.

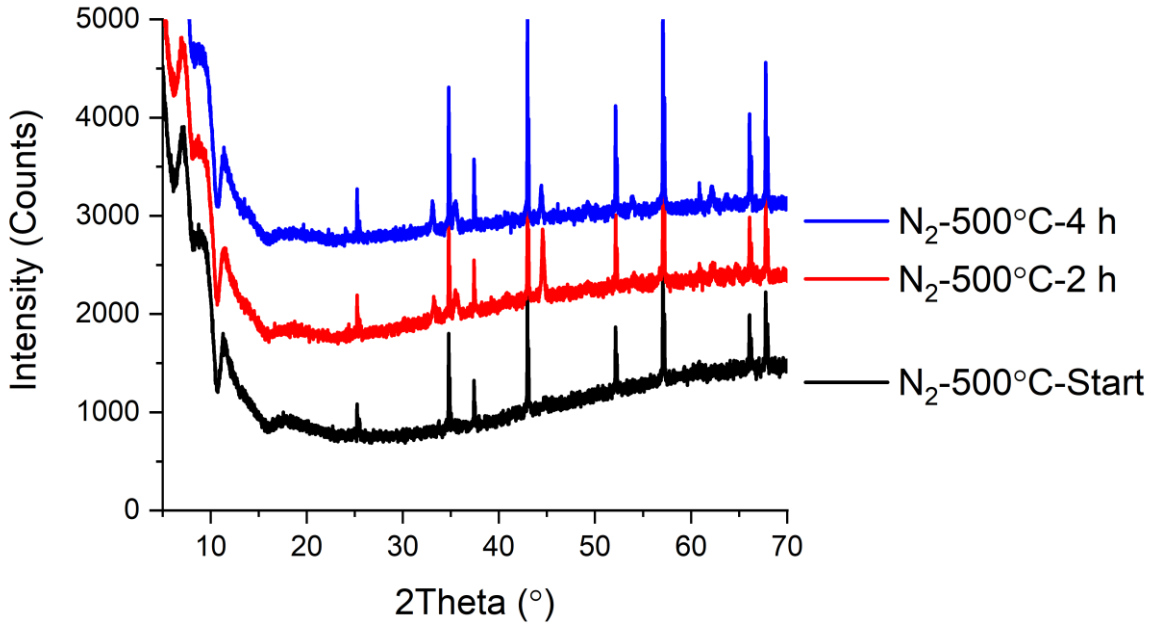

Figure 51. 4 h *in situ* PXRD of PCN-250 under N_2 held at 500 °C.

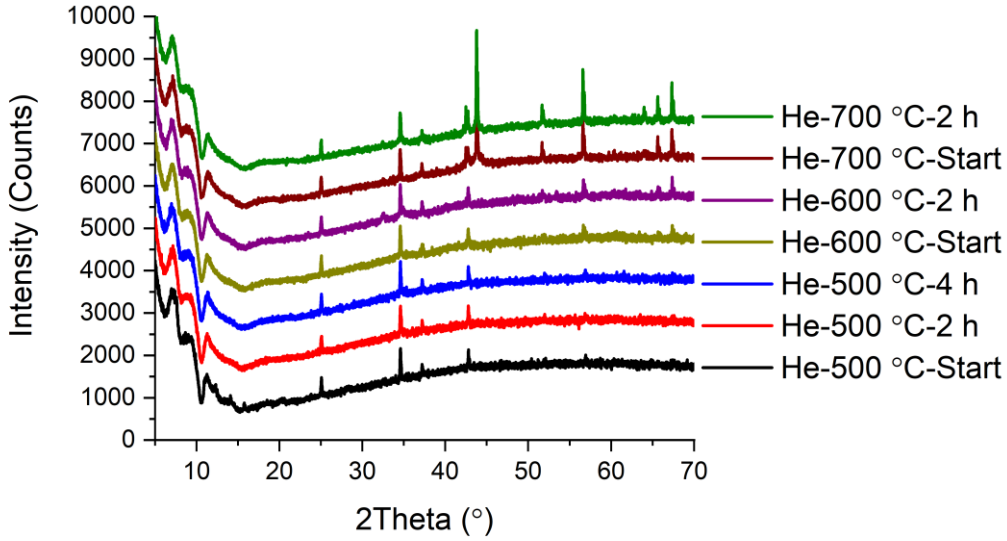

Figure 52. *In situ* PXRD of PCN-250 under He including holds at 500 °C for 4 hours, 600 °C for 2 hours, and 700 °C for 2 hours.

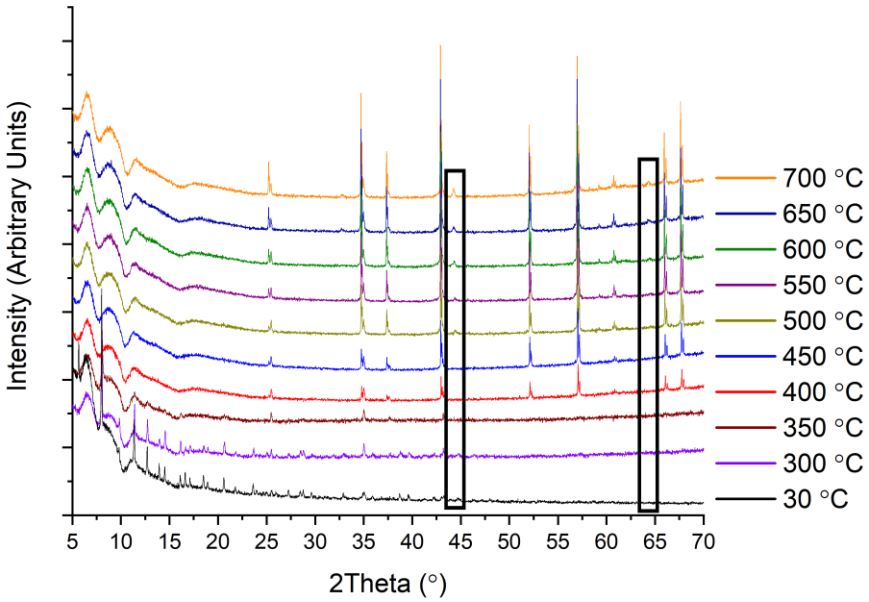

Figure 53. in situ PXRD of PCN-250 under Ar showing only small amounts of Fe(0) growth as well as peaks due to the alumina sample holder. The growth of Fe(0) appears to be less than under N_2, but higher than under He.

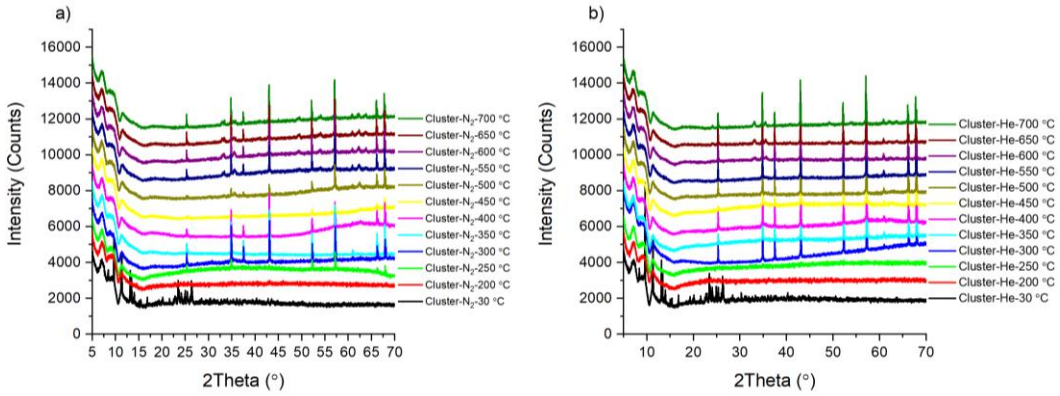

Figure 54. a) *in situ* PXRD of the calcination of the isolated $Fe_3\mu_3O$ cluster in the presence of N, b) cluster calcination in the presence of He.

To determine if Fe(0) was indeed being formed during tube furnace calcination, an air-free sample collection environment was built. Using the cell, the sample could be isolated under N_2 during and after calcination and then brought into an Ar filled glove-box. Using an air-free PXRD cell, we were able to analyze the sample, showing the presence of Fe(0) (**Figure 55**). The procedure also allowed us to calcine PCN-250 under H_2 and isolate the result, which showed the presence of Fe(0) (**Figure 56**). Rietveld refinement of these samples suggests a domain size of 13.9 nm for the N_2 sample and a size of 30 nm for the H_2 calcined sample.

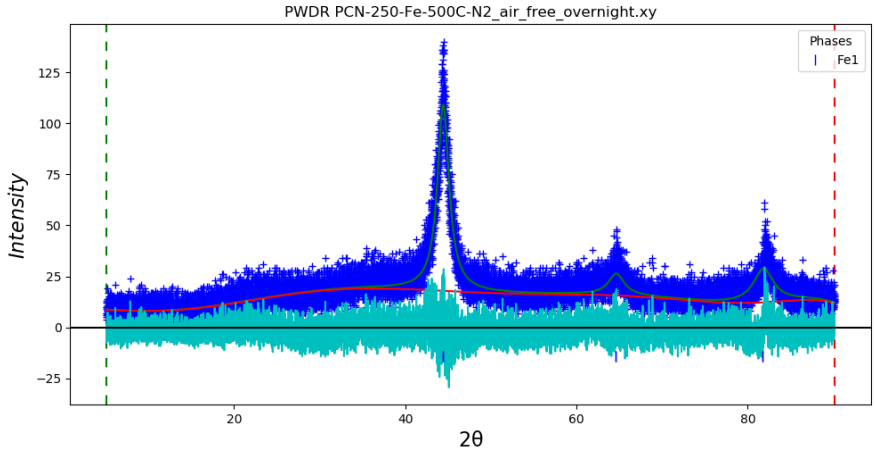

Figure 55. Air free PXRD of N_2 calcined PCN-250 collected via the air free cell and fit to zero-valent iron.

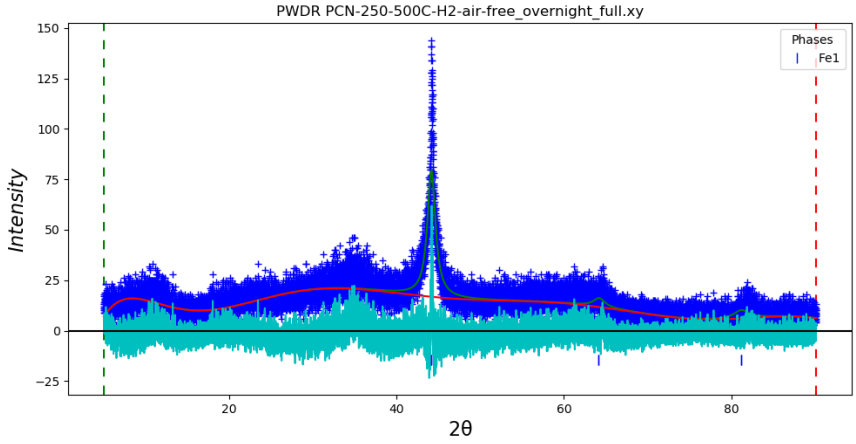

Figure 56. Air free PXRD of H_2 calcined PCN-250 collected via the air free cell and fit to zero-valent iron.

Additionally, N_2 adsorption analysis of the two samples suggests that the post calcination oxidation appears to increase the BET surface area and pore volume, as both air-free samples have lower surface areas and pore volumes compared to their air-exposed counterparts. The N_2 calcined sample exhibits a BET surface area of 220 m^2/g and a pore volume of 0.188 cm^3/g (versus 235 m^2/g and 0.201 cm^3/g for the air-exposed sample), and the H_2 calcined sample exhibits a BET surface area of 84 m^2/g and a pore volume of 0.084

cm^3/g (versus 98 m^2/g and 0.112 cm^3/g for the air-exposed sample). Also, the isotherms of the two samples are broadly similar in features to their oxidized counterparts, with some variation in the H_2 sample due to a more considerable hysteresis, suggesting a difference in the mesopore shape (**Figure 57**).

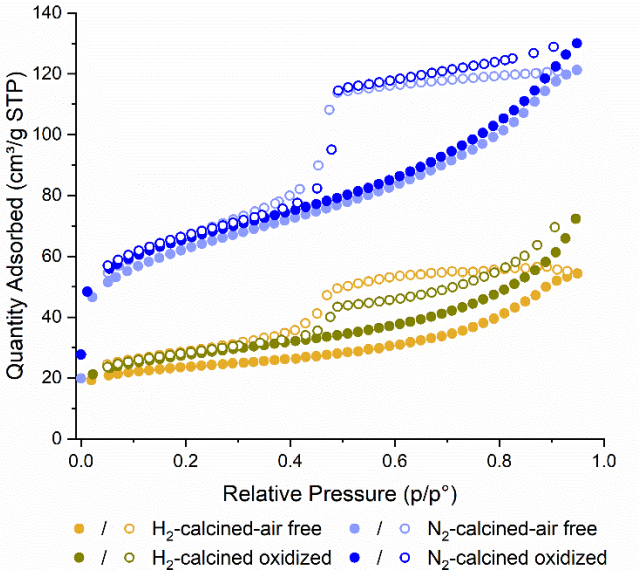

Figure 57. N_2 adsorption isotherms of the air free N_2 and H_2 calcined systems alongside samples exposed to air after calcination.

Conclusions

The work herein showcases the unique behavior of the iron-based MOF, PCN-250, during calcination under different gas flow environments. While our initial hypothesis proposed that the calcination conditions could change the porosity of the sample, we were surprised by the formation of different phases of iron during the calcination process. These results show that the nanoconfined state of the iron sites within the MOF allows for an unprecedented level of oxidation control, with the atmospheric conditions above the sample being entirely responsible for the formation of the resulting iron oxide phase. The

local structure of several of the materials was probed via neutron scattering PDF experiments, which allowed for partial investigation of the magnetic structure of the carbon scaffolded iron oxide materials, which showed that while the size range of the carbon ordering is similar between different samples, the relative ratio of ordering at the molecular level changes significantly with gas environment. A post-calcination oxidation event was observed for N_2, H_2, and He calcined samples, which resulted in the formation of mixed oxide phases within the samples. These materials were probed via in situ PXRD and air-free calcination methods, which showed that these post- calcination oxidations are at least partially due to the formation of zero-valent iron under calcination conditions. Future work will focus on elucidating the mechanism of zero-valent iron formation, as well as the effect of the local environment and nanoconfinement of the metal centers on the reduction event. The ability to control the bulk and local structure of metal oxide-containing porous carbons are of great use for potential catalytic applications, with future work focusing on the development of heterogeneous catalysts through the controlled calcination of MOFs.

CHAPTER IV

USING METAL-ORGANIC FRAMEWORKS AS TEMPLATES FOR SHAPE AND PHASE CONTROLLED CARBONS

Introduction

Metal-organic framework (MOF) derived carbons (MOFdCs) are an emerging class of porous materials that aim to utilize the advantages of MOFs, highly tunable structures and functionalities, while at the same time improving the traditional weaknesses, primarily their thermal and hydrolytic stability.[255] Due to these factors, MOFdCs have found applications in areas that MOFs are often poorly suited for: battery electrodes,[290] high temperature catalysis,[189] and waste-water remediation.[260]

The development of MOFdCs has been hindered due to difficulties in characterizing their structures as they often lack the well-ordered crystallinity of their precursor MOF scaffolds. This lack of structural ordering limits characterization techniques often employed for MOFs, such as single-crystal x-ray diffraction (SCXRD) and powder x-ray diffraction (PXRD). However, pair distribution function (PDF) analysis, a popular technique for the characterization of amorphous systems, uses a Fourier transform of the total scattering data gathered during X-ray or neutron powder diffraction experiments to transform the diffuse scattering from reciprocal space to real space. Therefore, giving information regarding the distribution of atomic pairs within the material.

By using PDF analysis, researchers can gain insight into the degree of ordering within a material. Specifically, we can obtain information regarding the short-range order,

typically on the order of angstroms to nanometers. This range of ordering is not captured from Bragg diffraction peaks.[291] Hence, PDF analysis is often used with crystalline materials to determine the level of disorder within the material, as well as with amorphous materials to gain insight into the change in ordering going from the atomic to the nanometer scale.

PDF analysis can be used with both X-ray and neutron sources, with the two methods offering complimentary insight based on the scattering power of neutrons and X-rays. In particular, neutron total scattering has shown high applicability for the analysis of carbon-based materials,[292] due to carbon atoms having a higher relative scattering factor for neutrons compared to X-rays.[219] This is an especially important factor for the investigation of the carbon scaffold in MOFdCs as X-ray PDF measurements would be heavily influenced by the scattering contribution from the metal centers, thus limiting the effectiveness of the technique.

As part of our work on MOFdCs, we have been investigating how the MOF structure changes during calcination. We have also studied the effect of the calcination conditions on both the total porous structure and the local structure. Herein, we report the effects of the gas environment and temperature of calcination on the porous carbon structure of two commonly used MOFs, Zn-MOF-74,[293] and UiO-66,[160] The work includes thermogravimetric analysis (TGA), N_2 adsorption, X-ray diffraction analysis, and neutron total scattering data to gain a better understanding of the processes that occur during MOF carbonization.

Results and Discussion

The initial hypothesis of this work was that calcination of MOFs under different gas environments should result in changes in both the porosity and the local structure of these systems. Initial thermogravimetric analysis (TGA) results of Zn-MOF-74 performed under different gas environments: air, 2% D_2O in N_2 (referred to as D_2O for clarity), N_2, CO_2, and He, using the same heating rate of 5 °C/min all show slightly different decomposition processes. There was a slight exception to this trend with air calcination samples, which showed a dramatic mass loss event around 375 °C (**Figure 58**). The other gas environments generally approach the same final mass fraction, with the exception of CO_2, with CO_2 calcination resulting in a slightly lower final mass fraction at 800 °C (35% as opposed to ~45% for D_2O, N_2, and He **Figure 59** Interestingly, in contrast to the results of Zn-MOF-74, there is no noticeable difference in the TGA curve of the UiO-66 samples under air as opposed to other gas environments (**Figure 59**). This suggests that at least under the conditions of these TGA experiments, the gas is only minimally interacting with UiO-66, as opposed to Zn-MOF-74, which appears to have a stronger interaction with air, leading to its faster decomposition.

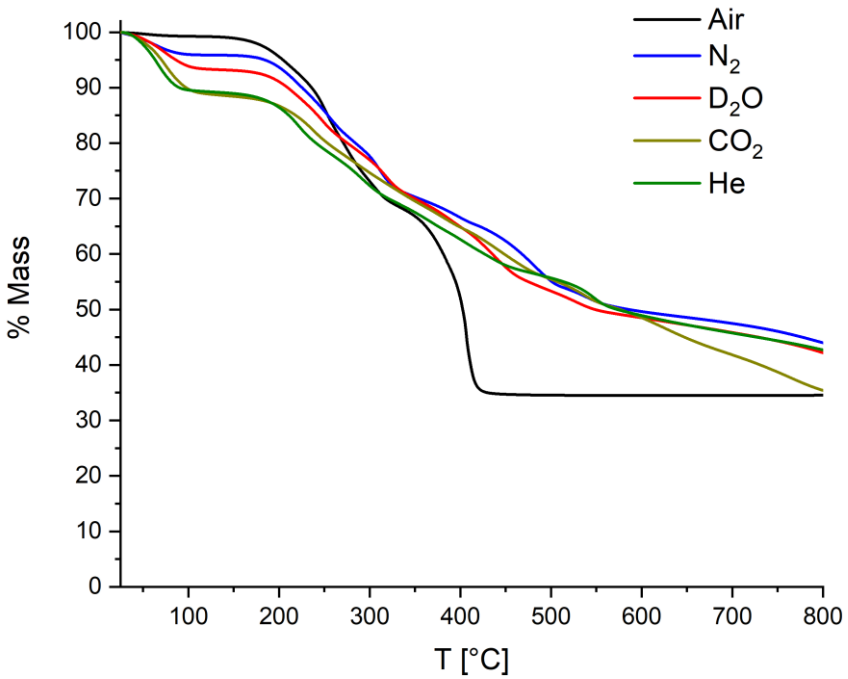

Figure 58. TGA curves for Zn-MOF-74 calcined under five different gas environments.

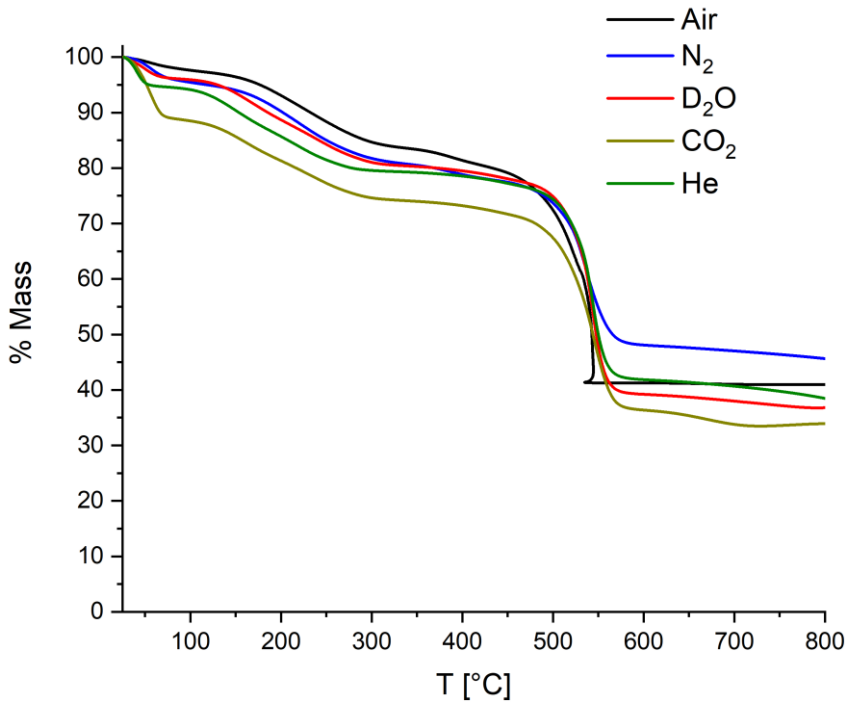

Figure 59. TGA curves for UiO-66 calcined under five different gas environments.

However, while the TGA experiments gave an idea regarding the thermodynamic stability of the MOFs, they do little to confirm either the kinetic stability under different gas environments or shed light as to the structural differences of the resulting carbonaceous materials. To that end, we performed a series of carbonization reactions on both Zn-MOF-74 and UiO-66 to determine how the presence of different gases affect the total pore structure of the materials. Initial calcinations were conducted using a tube furnace fitted with a gas flow set-up. The calcinations were performed using a ramp rate of 5 °C/min and were held at the operating temperature (500, 600, and 700 °C) for 4 h. This was followed by subsequent cooling to ambient conditions and sample collection. After collection, each sample was analyzed via N_2 adsorption analysis and powder X-ray diffraction (PXRD).

As part of the calcination process, we investigated two distinct parameters, the calcination gas: air, D_2O, N_2, 5% H_2 in N_2 (hereby referred to as H_2), CO_2, and He, as well as the hold temperature used during the calcination: 500 °C, 600 °C, and 700 °C (used for D_2O, N_2, CO_2, and He only, with air conducted at 600 °C for UiO-66 only). Air was used as a calcination gas to act as a baseline, seeing as it should result in the complete combustion of the MOFs. As such, calcining the MOFs at different temperatures under air was deemed unnecessary. Zn-MOF-74 and UiO-66 were chosen due to their differences in open metal sites within the structure. Zn-MOF-74 is known to contain open metal sites and is often used in gas adsorption applications as a result,[294] UiO-66 lacks the open metal site feature as it contains saturated zirconium oxo clusters. Both structures were chosen as

they allow for the investigation of the effect of gas adsorption at the open metal sites on the carbonization process.

The particular metal oxide phase of each calcined sample was confirmed via Rietveld refinement using the program GSAS-II.[277] Rietveld refinement of the different MOFdCs was performed with refinement on the sample displacement, the unit cell parameters, the atomic coordinates, and anisotropic thermal parameters, as well as the domain size and particle microstrain. Interestingly, UiO-66 did not completely calcine at 500 °C with several of the gases and was shown to be structurally more robust under CO_2 and He conditions. In all of the PXRD patterns except the air calcined sample, there is a noticeable amount of parent UiO-66 sample remaining. The CO_2 samples were shown to be composed entirely of UiO-66 via Rietveld refinement. Despite this, there are still some noticeable features related to ZrO_2 in the PXRD pattern for most of the 500 °C samples (**Figure 60**). Meanwhile, Zn-MOF-74 calcined at 500 °C does not show any degree of parent MOF structure remaining. This is likely due to the much lower decomposition temperature of Zn-MOF-74 relative to UiO-66. Both Zn-MOF-74 and UiO-66 did show almost complete loss of porosity upon calcination under air at 500 °C. The air-calcined Zn-MOF-74 was determined to be 0.14% carbon by weight, and the air-calcined UiO-66 was determined to be 0.60% carbon by weight (**Tables 7 and 8**). Interestingly, it was determined that the zirconium dioxide (ZrO_2) phase that matched the decomposition products of the UiO-66 calcined samples was the cubic phase,[295] This is of interest as it opposes to the more common and thermodynamically stable monoclinic phase of ZrO_2. Typically, bulk cubic phase zirconia is only stabilized through the use of additives, such

as yttrium oxide.[296] The relative stability of the different zirconia phases is known to be size-dependent, with the cubic phase being the thermodynamically stable phase at sizes less than 2 nm in diameter.[297] However, Rietveld refinement of the calcined UiO-66 samples generally determined particle sizes to be greater than 2 nm, despite the cubic structure (**Table 9**). This preference for the cubic structure is likely a result of MOF templating. The zirconium oxo clusters in UiO-66 display an octahedral symmetry, giving the clusters a geometry similar to that of the cubic phase.[298-299] Hence, this preformed high symmetry cluster, combined with nanoconfinement within the porous carbon scaffold, is likely the cause of the stabilization of the cubic phase.

Table 7. Elemental Analysis data for Zn-MOF-74-Carbon Samples

Atmosphere	Calcination Temperature (°C)	C (wt%)	H (wt%)	N (wt%)
Air	500	0.14	0.00	0.00
H_2	500	23.38	0.80	0.69
D_2O	500	22.97	1.06	0.68
D_2O	600	22.74	0.67	0.61
D_2O	700	21.34	0.48	0.41
N_2	500	27.53	1.31	2.03
N_2	600	31.96	1.26	1.89
N_2	700	45.81	2.03	2.00
CO_2	500	21.54	1.71	1.37
CO_2	600	14.12	0.52	1.63
CO_2	700	25.19	0.46	1.06
He	500	25.20	1.74	1.30
He	600	30.57	1.22	2.06
He	700	30.25	0.51	1.49

Table 8. Elemental Analysis data for UiO-66-Carbon Samples

Atmosphere	Calcination Temperature (°C)	C (wt%)	H (wt%)	N (wt%)
Air	500	0.60	0.00	0.00
Air	600	0.37	0.38	0.00
H_2	500	23.91	2.97	0.21
D_2O	500	15.73	1.73	0.00
D_2O	600	2.47	0.19	0.00
D_2O	700	2.69	0.13	0.00
N_2	500	28.06	2.30	0.14
N_2	600	26.75	1.18	0.17
N_2	700	21.17	0.99	0.14
CO_2	500	26.70	4.41	0.18
CO_2	600	7.66	0.52	0.22
CO_2	700	7.45	0.34	0.74
He	500	27.38	4.39	0.35
He	600	15.04	0.67	0.23
He	700	16.97	0.82	0.52

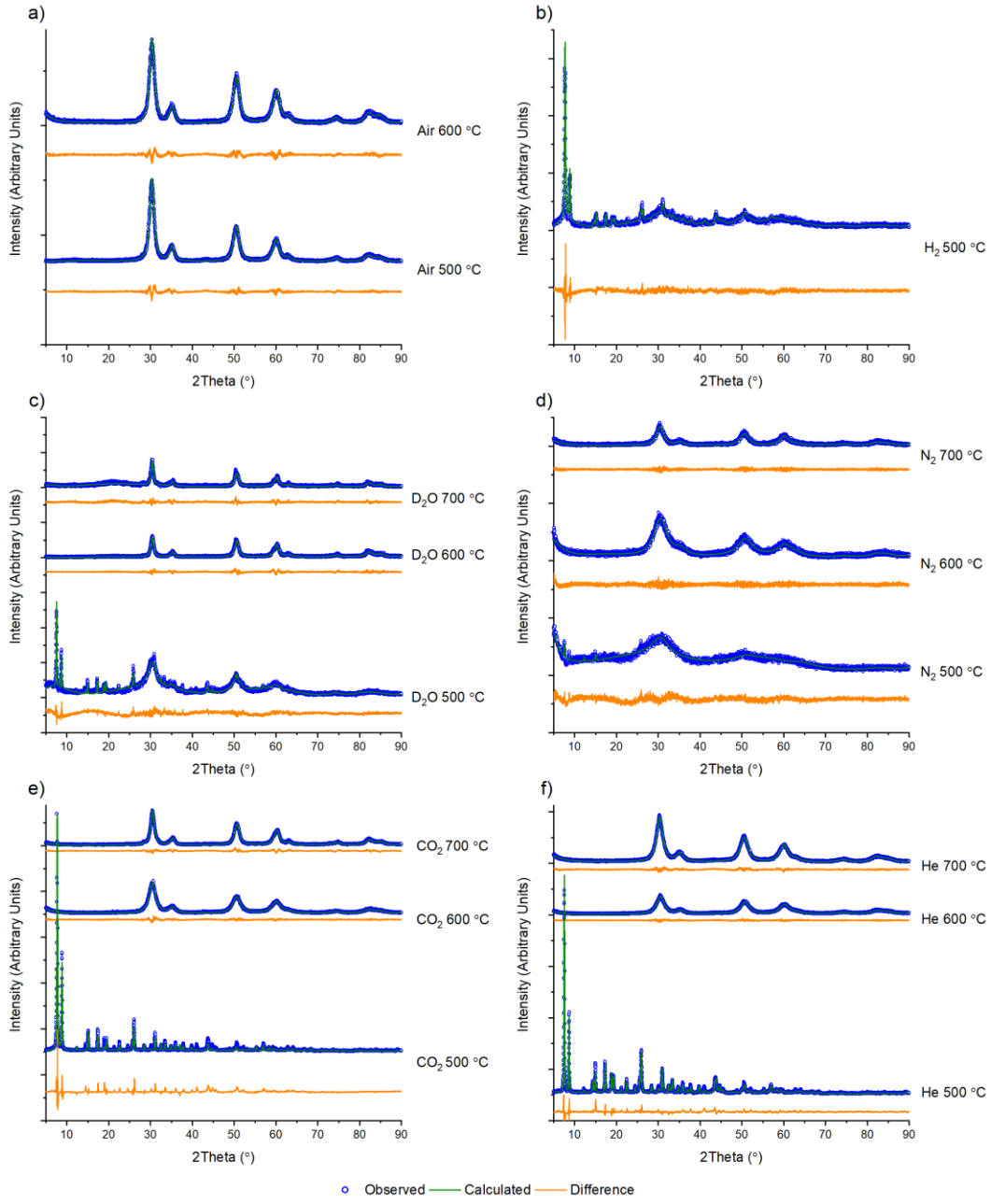

Figure 60. Rietveld Refinement results for UiO-66 calcined under a) air, b) H_2, c) 2% D_2O in N_2, d) N_2, e) CO_2, and f) He. All samples were refined to the structure of cubic zirconium dioxide (except for CO_2-500 °C), with the 500 °C samples also refined to the UiO-66 structure. The calcination temperatures are labeled next to the individual patterns.

Table 9. Porosity and Rietveld Refinement Results for UiO-66

Gas	Temperature (°C)	Surface area (m^2/g)	Pore Volume (cm^3/g)	Metal Oxide Domain Size (nm, X-ray)	Metal Oxide Domain Size (nm, neutron)
Air	500	8	0.011	13.7(4)	4.91(8)
Air	600	72	0.082	9.8(2)	---
H_2 (5% in N_2)	500	375	0.172	7(4)	---
D_2O (2% in N_2)	500	291	0.163	4.27(31)	8.7(4)
D_2O (2% in N_2)	600	39	0.056	29.2(21)	---
D_2O (2% in N_2)	700	19	0.051	94(25)	---
N_2	500	180	0.093	1.9(4)	4.0(7)
N_2	600	138	0.062	2.20(6)	---
N_2	700	235	0.175	6.2(3)	7.2(5)
CO_2	500	1026	0.451	N/A	---
CO_2	600	113	0.096	6.80(16)	---
CO_2	700	69	0.083	15.2(5)	---
He	500	974	0.434	20(9) (10.3(17)% phase fraction)	---
He	600	157	0.105	5.82(15)	---
He	700	194	0.108	7.47(16)	---

The Zn-MOF-74 samples all calcined to the hexagonal wurtzite structure of zinc oxide (ZnO).[300] Calcination at increasing temperatures results in a steady increase in the zinc oxide domain size (**Figure 61**, **Table 10**). This increase in zinc oxide domain size can be confirmed via transmission electron microscopy (TEM) of the 500 °C calcined samples compared to the 700 °C calcined samples (**Figure 62**). The D_2O 500 °C calcined sample shows the presence of well-dispersed, nanometer-sized metal oxide phases (**Figure 62b**). In contrast, the 700 °C calcined sample shows an exterior surface that is

entirely composed of ZnO (**Figure 62d**). Based on the TEM and Rietveld analysis, it appears that the ZnO nanoparticles are sintered together at 700 °C,[301] forming a bulk domain on the surface of the MOFdC. Sintering in solid materials is typically known to occur in temperature regions slightly above half the melting point. However, the onset temperature is known to decrease with nanoscale particles.[302]

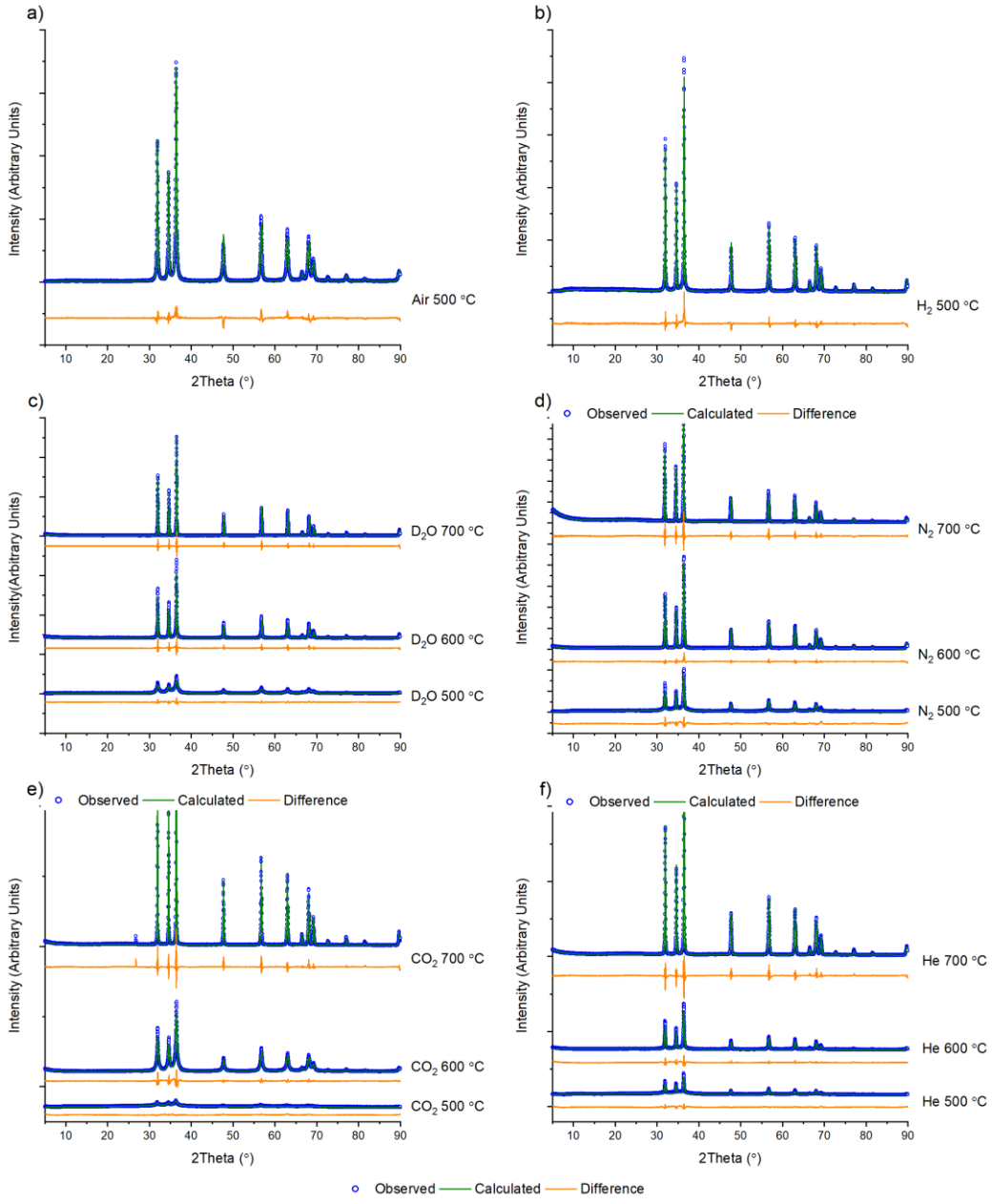

Figure 61. Rietveld Refinement results for Zn-MOF-74 calcined under a) air, b) H_2, c) 2% D_2O in N_2, d) N_2, e) CO_2, and f) He. All samples were refined to the structure of Zinc Oxide. The calcination temperatures are labeled next to the individual patterns.

Table 10. Porosity and Rietveld Refinement Results for Zn-MOF-74

Gas	Temperature (°C)	Surface area (m^2/g)	Pore Volume (cm^3/g)	Metal Oxide Domain Size (nm, X-ray)	Metal Oxide Domain Size (nm, neutron)
Air	500	8	0.018	106(4)	115(2)
H_2 (5% in N_2)	500	277	0.204	194(9)	---
D_2O (2% in N_2)	500	248	0.134	15.1(4)	25.0(2)
D_2O (2% in N_2)	600	291	0.197	127(5)	176(26)
D_2O (2% in N_2)	700	292	0.229	289(11)	230(30)
N_2	500	187	0.087	37.6(17)	68.0(18)
N_2	600	418	0.198	100.5(18)	250(80)
N_2	700	646	0.370	318(24)	260(190)
CO_2	500	169	0.142	5.95(19)	---
CO_2	600	194	0.127	25.6(5)	---
CO_2	700	185	0.251	478(31)	---
He	500	173	0.108	33(15)	---
He	600	274	0.143	57.4(18)	---
He	700	317	0.188	390(40)	---

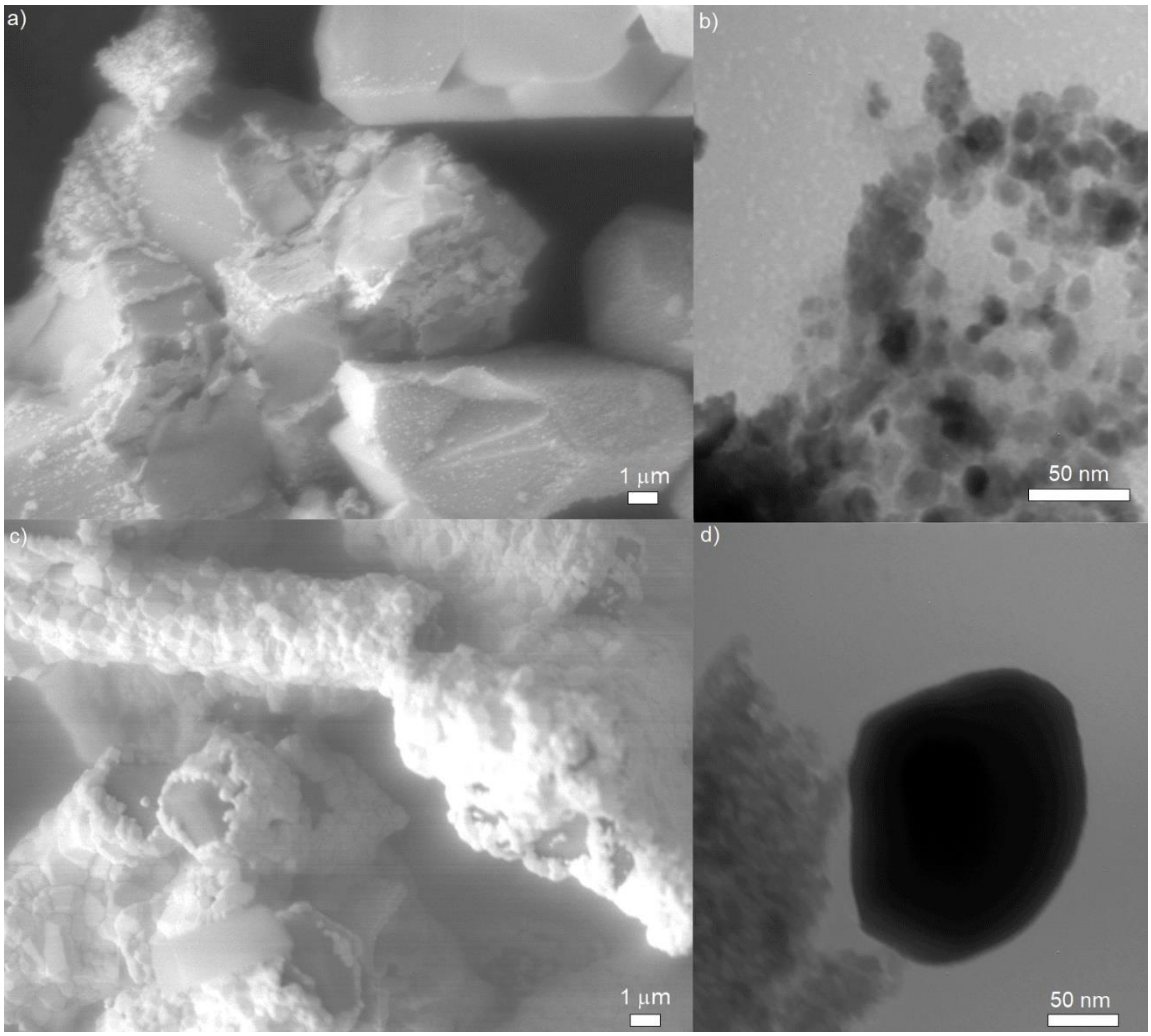

Figure 62. a) SEM image of Zn-MOF-74 calcined under D_2O at 500 °C showing the minimal surface formation of ZnO, b) TEM image of 500 °C D_2O calcined Zn-MOF-74 showing nanoscale metal oxides. c) 700 °C D_2O calcined Zn-MOF-74 showing the ZnO sintering that is occurring on the surface, the TEM image d) appear to mainly be ZnO.

With a melting point of almost 2000 °C, ZnO would be considered to sinter around ~1000 °C, although it is still not unusual for ZnO to begin sintering as low as 700 °C.[301] This same sintering effect is also observed in the TEM images of the N_2 calcined sample (**Figure 63**), matching well with the general domain size trend observed via Rietveld refinement.

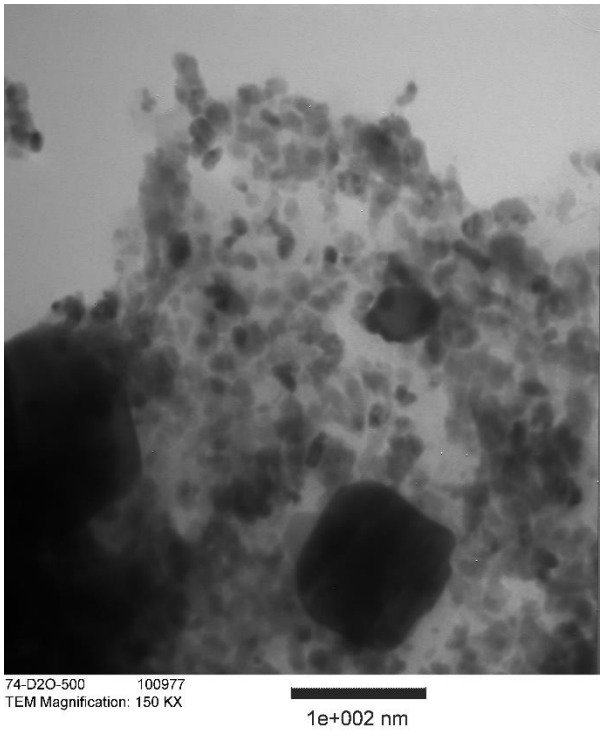

Figure 63. TEM image of 500 °C D_2O calcined Zn-MOF-74.

Interestingly, despite the formation of the large domain ZnO, there is no reduction in the total carbon content of the materials. In contrast, many of the samples show a higher total carbon weight percentage upon calcination at higher temperatures (**Table 7**), and they exhibit larger surface areas (**Table 10**). The data suggests that this sintering behavior mainly occurs on the surface of the material, leaving a significant degree of internal porosity. These findings can be corroborated by the scanning electron microscopy images (SEM). The 700 °C D_2O calcined Zn-MOF-74 sample showed a large number of fused solids forming around the exterior diameter of bulk rods (**Figures 62d**) while still maintaining an interior carbon phase. Similar behavior is observed for the 700 °C N_2 (**Figure 64**) sample as well as the 600 °C N_2, CO_2, and He calcined samples.

Interestingly a few of the samples, 600 °C D_2O, 700 °C CO_2, and 700 °C He (**Figure 65**), instead show large surface nodules of ZnO on top of a carbon rod. These surface nodules are noticeably thicker than the thin ZnO walls on the 700 °C D_2O samples, which suggests that a similar sintering mechanism is occurring, but that the ZnO is migrating into more confined areas during calcination. Meanwhile, the 500 °C calcined samples have a smattering of unaffiliated surface oxides on top of the bulk framework (**Figure 66**), suggesting that the onset of sintering does not occur at this temperature, which correlates with the lower crystallite sizes determined from Rietveld refinement.

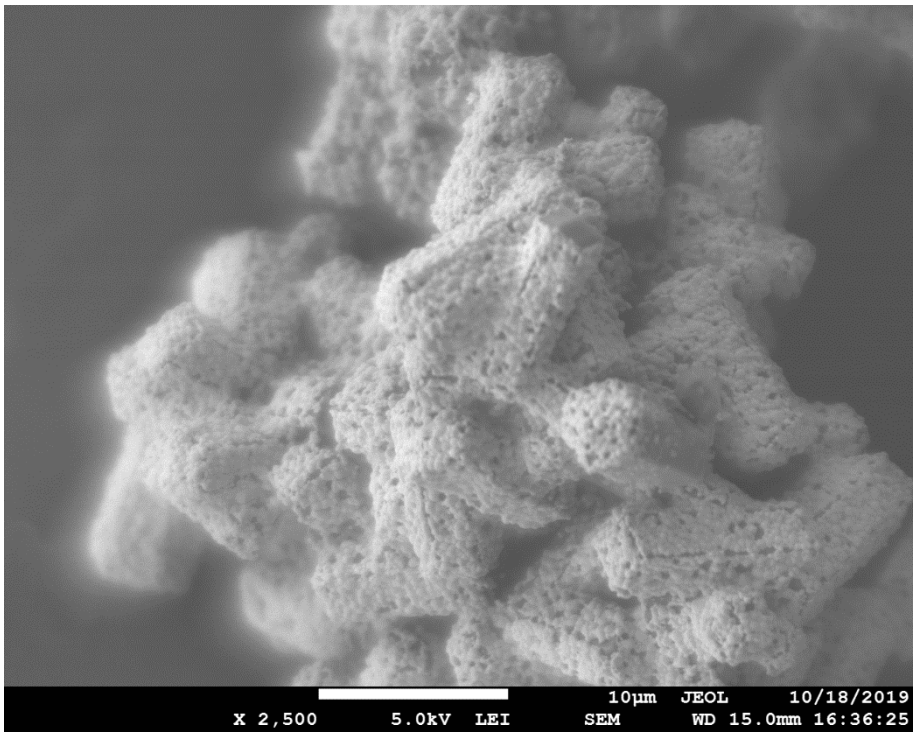

Figure 64. SEM image of the 700 °C N_2 calcined Zn-MOF-74.

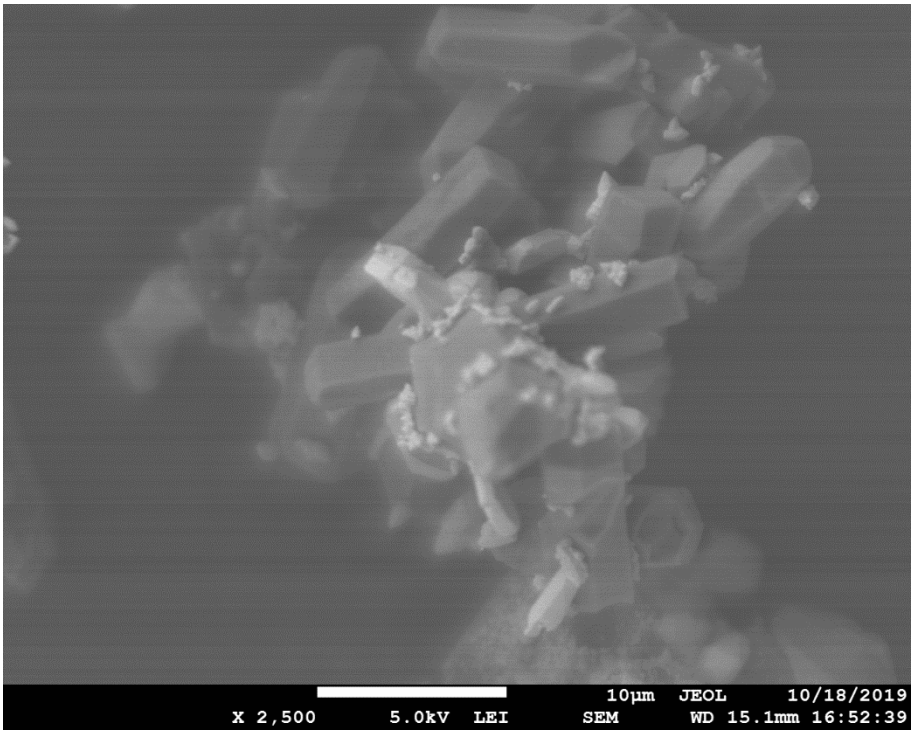

Figure 65. SEM image of the 700 °C He calcined Zn-MOF-74.

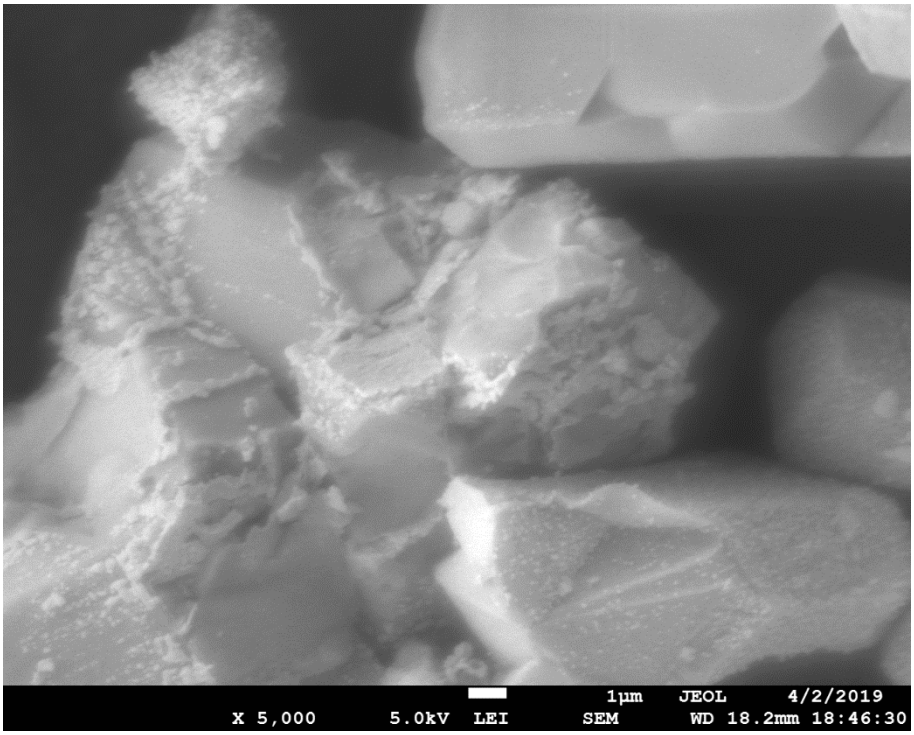

Figure 66. SEM image of the 500 °C D_2O calcined Zn-MOF-74.

In general, the UiO-66 crystals are noticeably smaller than Zn-MOF-74, with individual UiO-66 particles being on the order of 0.1 to 1 microns depending on the batch. This small size is typically maintained upon calcination. However, many of the smaller particles tend to agglomerate, and this agglomeration is still observed in the SEM of the MOFdCs products (**Figure 67**). The particles observed are all generally uniform, maintaining structural cohesion during calcination, similar to Zn-MOF-74. Due to the much higher melting point of ZrO_2 (> 2700 °C), about 3.85 times greater than the highest calcination temperature utilized, there is no noticeable sintering or metal oxide migration observed in the SEM. Additionally, the TEM of the 700 °C N_2 calcined sample (given as representative samples for the UiO-66 calcination) also generally still show nanoscale metal oxide features, with a carbonaceous matrix (**Figure 68**). These results fit well with the Rietveld refinement, suggesting minimal sintering in the UiO-66 derived samples.

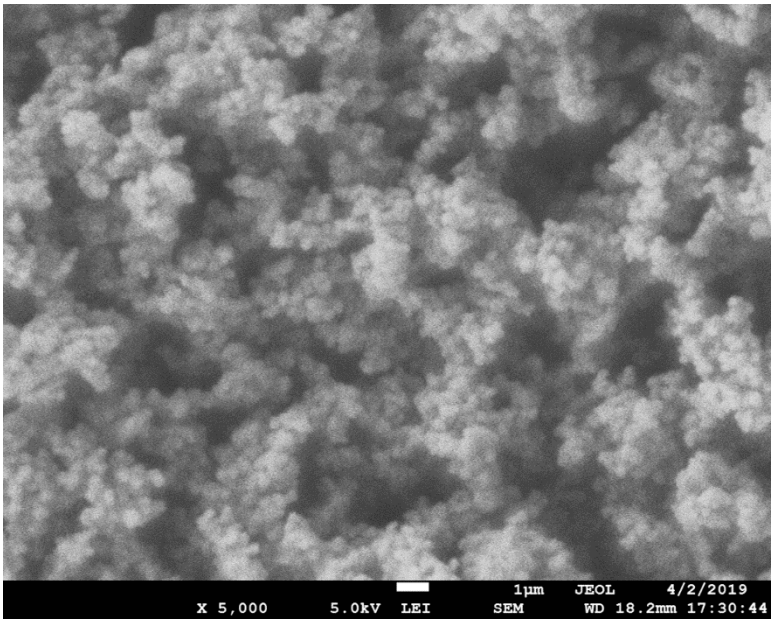

Figure 67. SEM image of the 500 °C N_2 calcined UiO-66.

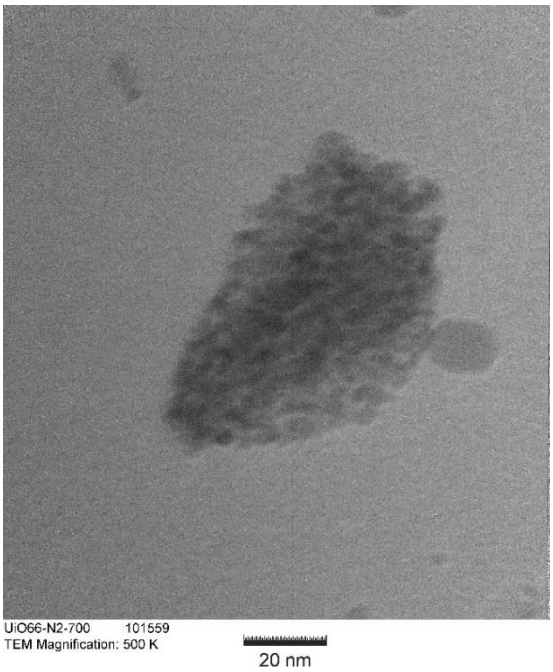

Figure 68. TEM image of the 700 °C N_2 calcined UiO-66.

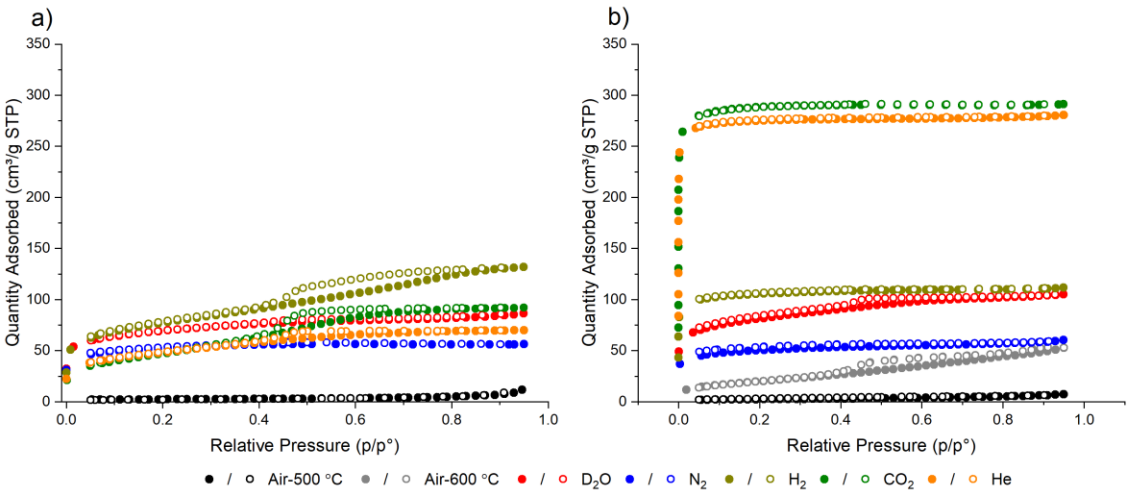

Figure 69. N_2 adsorption isotherms for a) Zn-MOF-74 and b) UiO-66 samples calcined at 500 °C under different gas environments. The 600 °C air calcined UiO-66 is included for comparison.

The N_2 adsorption analysis of both Zn-MOF-74 and UiO-66 calcined at 500 °C shows that each sample appears to maintain some degree of porosity, with each gas environment resulting in difference total uptake (**Figure 69**). The samples calcined at 500 °C showed total N_2 adsorption uptakes less than 150 cm^3/g, with a broad mix of microporosity and mesoporosity. The two apparent outliers, UiO-66 calcined under CO_2 and He showed distinctive microporous isotherms that are similar to isotherms observed for UiO-66.[303] This corroborates the Rietveld analysis of both samples, which are mainly (89.3%, He) or entirely (CO_2) comprised of the parent UiO-66 material. The surface areas of the Zn-MOF-74 based MOFdCs tend to be low, with only the H_2 calcined sample showing a surface area greater than 250 m^2/g (**Table 8**). For comparison, a typical example of Zn-MOF-74 had a surface area around 500 m^2/g.[294] Interestingly, there is a distinct difference in shape for each individual isotherm, with only the H_2, CO_2, and He calcined samples showing noticeable hysteresis. The He samples show a minor hysteresis, but the N_2 and the D_2O samples tend to have flat adsorption uptakes at higher pressures, indicating minimal mesoporosity.

Calcination of Zn-MOF-74 at higher temperatures (600 °C and 700 °C) appears to result in a general increase in the level of microporosity with the samples. In particular, the sample calcined under N_2 at 700 °C results in a surface area of 646 m^2/g, generally higher than the parent MOF (**Figure 61c**, **Table 8**).[294] The samples calcined under other conditions also usually show an increase in surface area with temperature. However, this is not as apparent for the samples calcined under N_2. The D_2O calcined samples at 600 °C and 700 °C show similar surface areas (291 and 292 m^2/g), but have noticeably different

behavior at higher pressures, indicative of an increase in mesoporosity. This is likely related to changes in the total pore volume of the materials, going from 0.134 cm^2/g for the 500 °C calcined sample to 0.197 and 0.229 cm^2/g for the 600 °C and 700 °C calcined samples respectively (**Figure 61b**, **Table 8**). This increase in porosity can be visualized through the noticeable hysteresis that is observed for the 600 °C and 700 °C samples (**Figure 61b**) which results in an increase in the differential pore volume in the 30-40 Å region according to BJH (Barrett, Joyner, and Halenda)[304] pore size distribution modeling (**Figure 70**). In general, the four different gas environments each show an increase in mesoporosity upon calcination at higher temperatures, resulting in a general trend of an increasing pore volume with temperature (**Table 10**). This is potentially related to the sintering effect observed in the SEM of these materials. As the sintering primarily occurs on the outer edge of the material, there is likely some migration of ZnO centers away from the interior channel of the MOFdC. Hence, this would result in an increase in internal mesoporous void spaces.

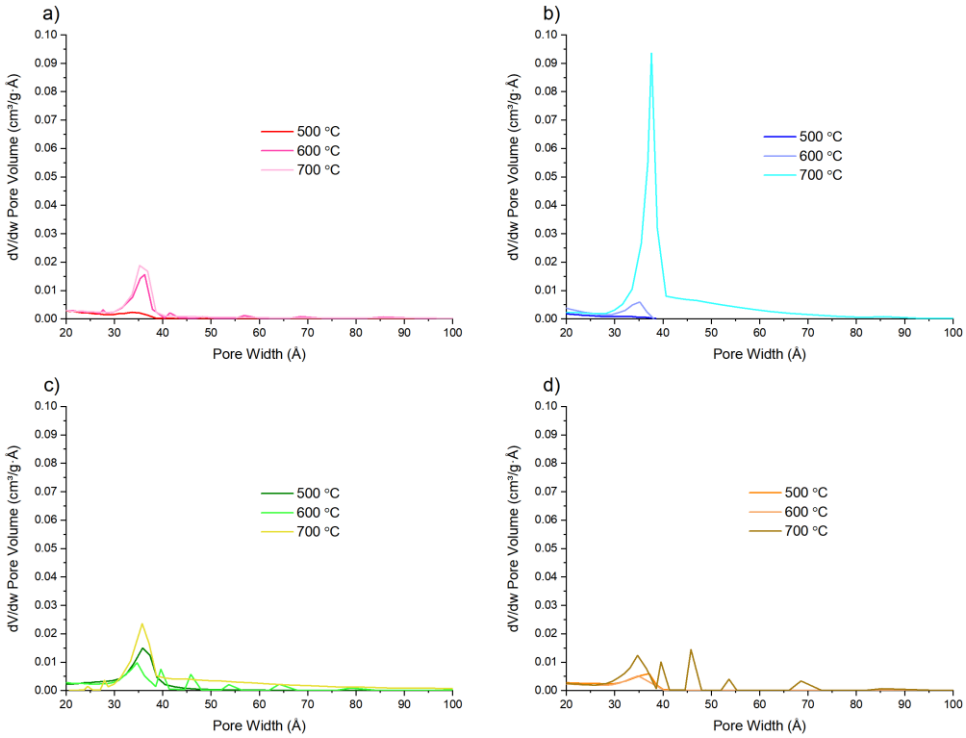

Figure 70. BJH model mesopore size distribution for Zn-MOF-74 calcined under a) D_2O in N_2, b) N_2, c) CO_2, and d) He. In general, the increase in temperature leads to an increase in mesoporosity, typically in the 30-40 Å range.

Calcination of UiO-66 at 500 °C results in a mixture of phase purities, with a significant amount of UiO-66 remaining in most of the materials. As such, the surface areas of several of these products remains relatively high, with samples in both CO_2 and He calcination conditions displaying surface areas near 1000 m^2/g (**Figure 69b**, **Table 9**). However, when the samples were calcined at higher temperatures, there is a significant drop in the surface areas. In particular, the 600 °C and 700 °C D_2O calcined samples show almost no porosity, with surface areas of 39 and 19 m^2/g respectively, with the CO_2 samples having only slightly larger surface areas, 113 and 69 m^2/g for 600 °C and 700 °C respectively. These four samples are unique in that the residual carbon weight percentages are also quite low, 2.47%, 2.69%, 7.66%, and 7.45% for D_2O 600 °C, D_2O 700 °C, CO_2

600 °C, and CO_2 700 °C, respectively. Both Zn-MOF-74 and UiO-66 MOFdCs show a broad trend towards an increased surface area with increased residual carbon content (**Figure 71-72**), suggesting that the loss of surface area is due to the combustion and subsequent loss of the ligand from the UiO-66 scaffold.

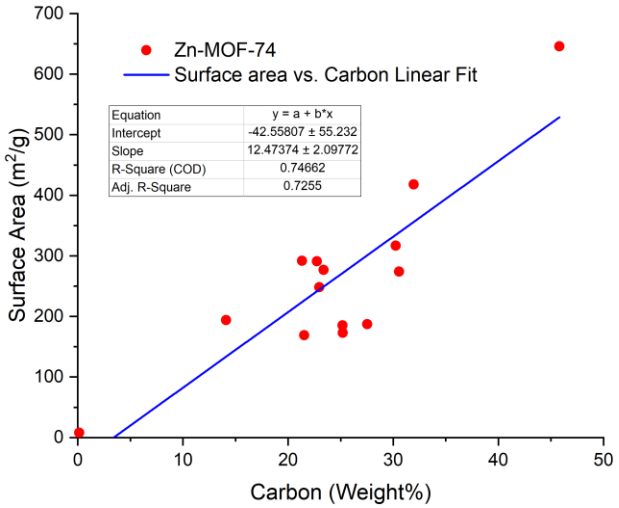

Figure 71. Relationship between surface area and total carbon content for calcined Zn-MOF-74 samples.

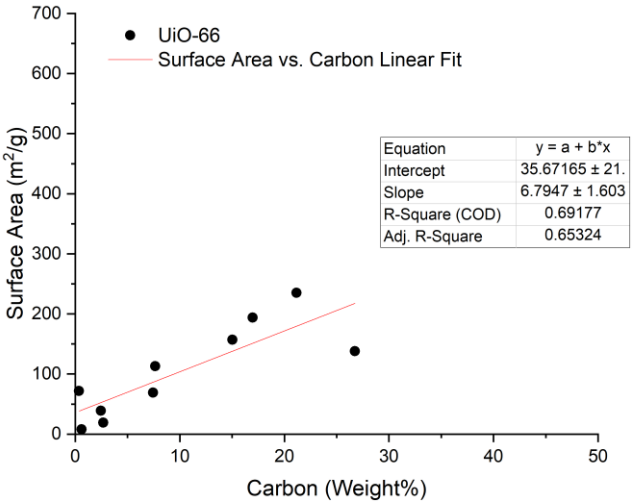

Figure 72. Relationship between surface area and total carbon content for calcined UiO-66 samples, the 500 °C calcined samples have been omitted due to their residual UiO-66 content.

In general, the UiO-66 MOFdCs show lower surface areas, as well as the correlated carbon content, as compared to Zn-MOF-74. This suggests that the ligand in UiO-66, benzenedicarboxylate (BDC), is more readily lost from the scaffold than the 2,5-dihydroxyterephthalate (DOBDC) ligand in Zn-MOF-74. Terephthalic acid is a simple dicarboxylate that binds to the metal centers in UiO-66 by bridging between two Zr centers in the MOF cluster.[160] Meanwhile, the hydroxy groups in 2,5-dihydroxyterephthalic acid assist in binding to the metal centers in Zn-MOF-74, with one carboxylate oxygen and the hydroxy oxygen both bound to a single metal. The second carboxylate oxygen in the structure interacts with a different metal in the metal chain.[293] As such, even though zirconium carboxylate bonds are generally understood to be thermodynamically strong, due to being a combination of a hard Lewis acid and a hard Lewis base according to Pearson's principle,[305] the bonds in UiO-66 are potentially kinetically labile, with a lower rate of recombination with the metal center due to lower individual connectivity. Essentially, when there is enough thermal energy to dissociate the metal-ligand interactions, the only driving force available to reform the metal-ligand interaction is the geometric constraints of the MOF. There is only a little kinetic driving force directed from the ligand itself due to the secondary binding site. However, as the temperature increases and the equilibrium shifts more towards the unbound state, there is also an increased chance of other ligands interacting with the coordination sphere of the zirconium. In addition, while both terephthalic acid and 2,5-dihydroxyterephthalic acid have an initial decomposition temperature of around 275 °C, caused by decarboxylation, 2,5-dihydroxyterephthalic acid also has a secondary decomposition event around 410 °C

caused by the degradation of the residual phenolic material (**Figure 73**). Due to the formation of this phenolic species, 2,5-dihydroxyterephthalic acid residues can still be found within the MOF-74 framework even after decarboxylation. However, at that same point, terephthalic acid undergoes complete combustion. This suggests that during carbonization, when terephthalic acid disassociates from the cluster, it starts to decarboxylate and thus completely degrade, causing a significant drop in the residual carbon. In the case of the D_2O and CO_2, this is exacerbated, with both gases potentially coordinating to the newly open metal centers. This competition is also partially enabled by the excess of both gases, which forces the equilibrium towards the gas coordinated, and thus the uncoordinated ligand state.

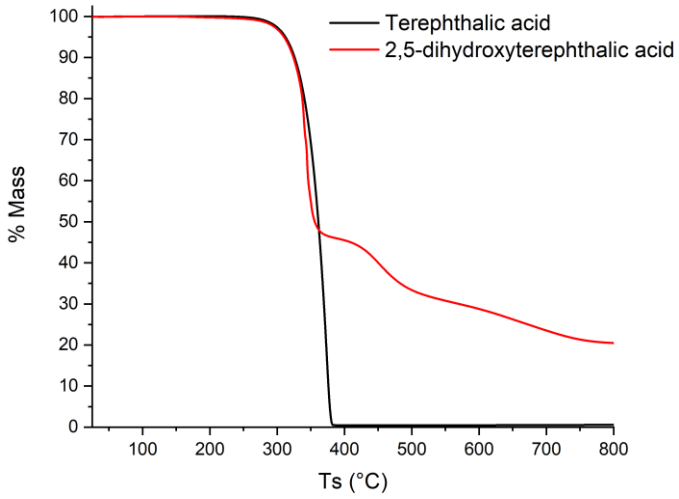

Figure 73. TGA curves for terephthalic acid and 2,5-dihydroxyterephthalic acid heated under an N_2 flow.

While this same gas coordination occurs with Zn-MOF-74, the MOF itself already has available open metal sites. With the interaction time frame at 500-700 °C being reasonably low for each individual gas molecule, there is less incentive for the ligand to

decoordinate, resulting in less gas interaction. The one exception to this is the case of CO_2, due to its known affinity towards open metal sites.[204] Tellingly, CO_2 calcined Zn-MOF-74 shows the lowest surface area of all Zn-MOF-74 MOFdCs, and also shows a small drop in surface area when temperatures are shifted from 600 °C (194 m^2/g) to 700 °C (185 m^2/g). Interestingly, despite having the lowest adsorption affinity of the gases tested, He typically does not have the highest surface area. N_2 shows the highest surface areas at 700 °C for both Zn-MOF-74 and UiO-66. Notably, N_2 typically has a low binding affinity for both Zn and Zr, likely interacting with the MOFs only through Van der Waals interactions, which could potentially be templating the increased surface area.

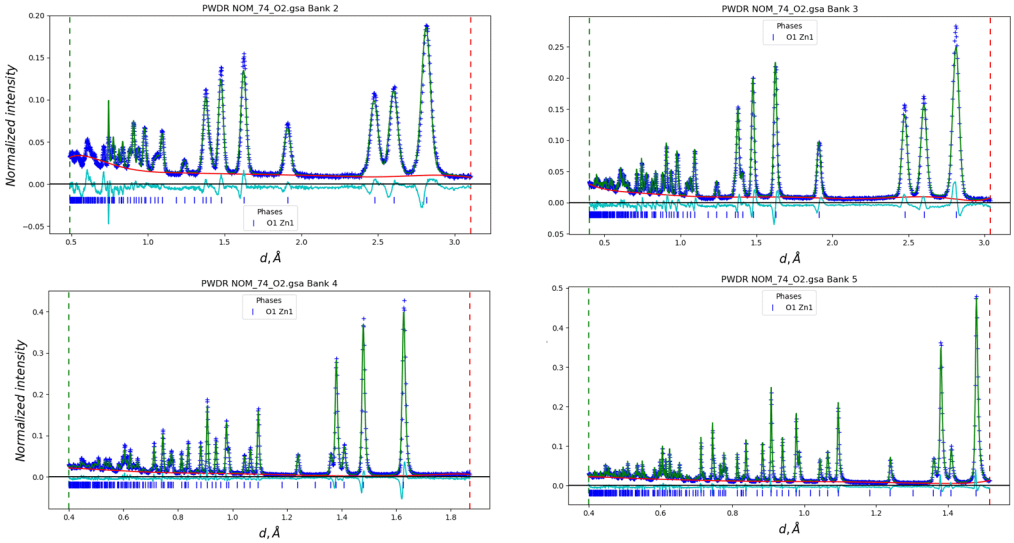

Figure 74. Rietveld refinement on the Bragg peaks from the neutron total scattering data for Zn-MOF-74 calcined under air at 500 °C.

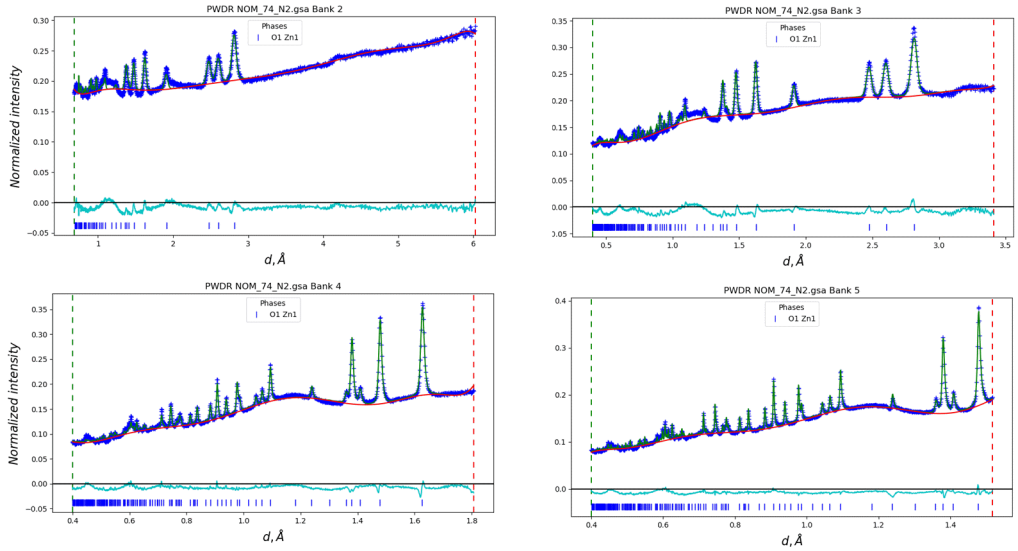

Figure 75. Rietveld refinement on the Bragg peaks from the neutron total scattering data for Zn-MOF-74 calcined under N_2 at 500 °C.

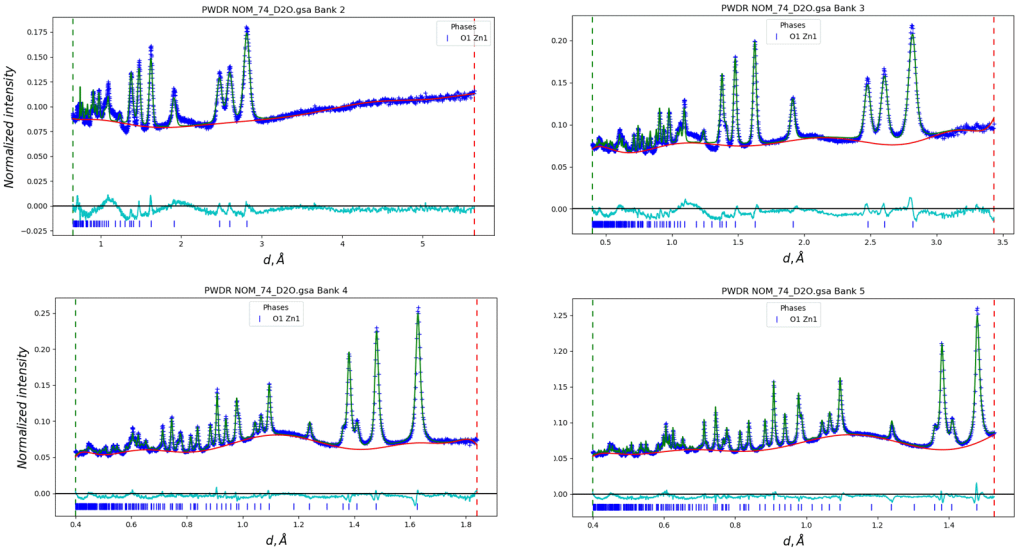

Figure 76. Rietveld refinement on the Bragg peaks from the neutron total scattering data for Zn-MOF-74 calcined under D_2O at 500 °C.

Neutron total scattering data was collected at the Nanoscale Ordered Materials Diffractometer (NOMAD) at the Spallation Neutron Source (SNS) at Oak Ridge National Laboratory (ORNL).[279] Data was collected for the 500 °C air, D_2O, and N_2 calcined

samples for both Zn-MOF-74 and UiO-66, as well as the 600 °C and 700 °C D_2O and N_2 calcined Zn-MOF-74 and the 700 °C N_2 calcined UiO-66. The Bragg diffraction data for the samples were analyzed using GSAS-II,[277] via refinement on the same parameters as the X-ray data. The domain size parameters calculated from the Rietveld refinement of the Zn-MOF-74 samples results in a trend similar to that of the X-ray data. Amongst the 500 °C calcined samples the air calcined sample (**Figure 74**)) having the largest size (115 nm), followed by the N_2 calcined samples (**Figure 75**) (6.0 nm), and the D_2O calcined samples (**Figure 76**) (25.0 nm) having the smallest size (**Table 10**). Additionally, increasing the temperature of calcination for the D_2O and N_2 calcined Zn-MOF-74 resulted in an increase in refined domain size, similar to the X-ray data (**Table 10**, **Figure 77-80**).

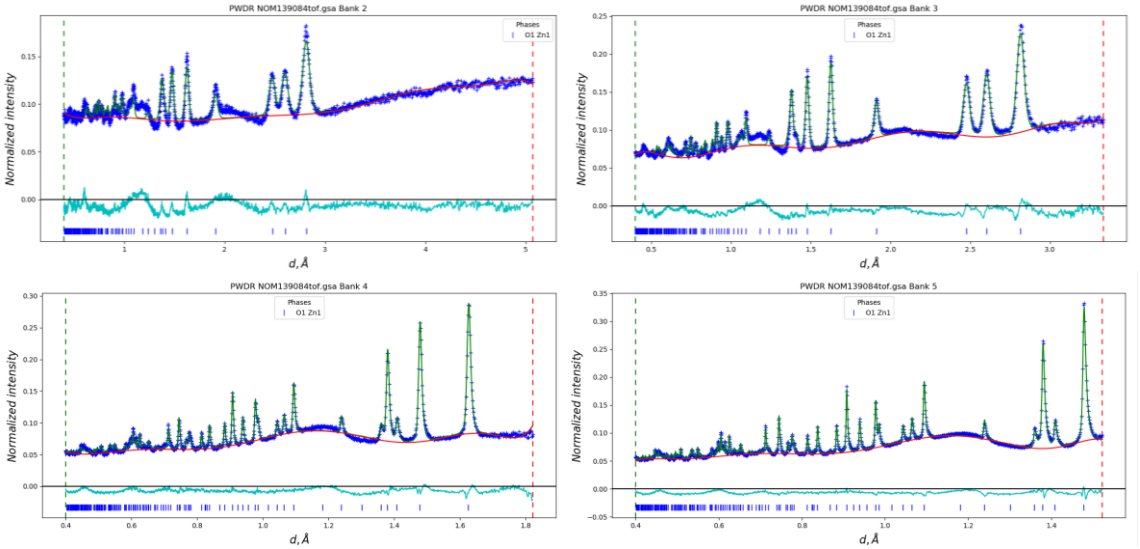

Figure 77. Rietveld refinment on the Bragg peaks from the neutron total scattering data for Zn-MOF-74 calcined under D_2O at 600 °C.

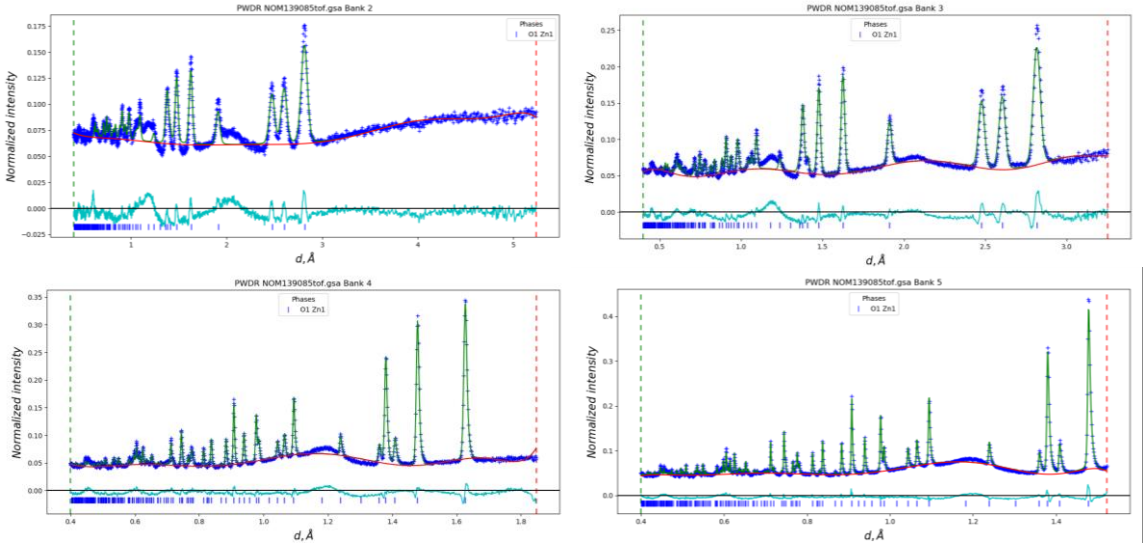

Figure 78. Rietveld refinment on the Bragg peaks from the neutron total scattering data for Zn-MOF-74 calcined under D_2O at 700 °C.

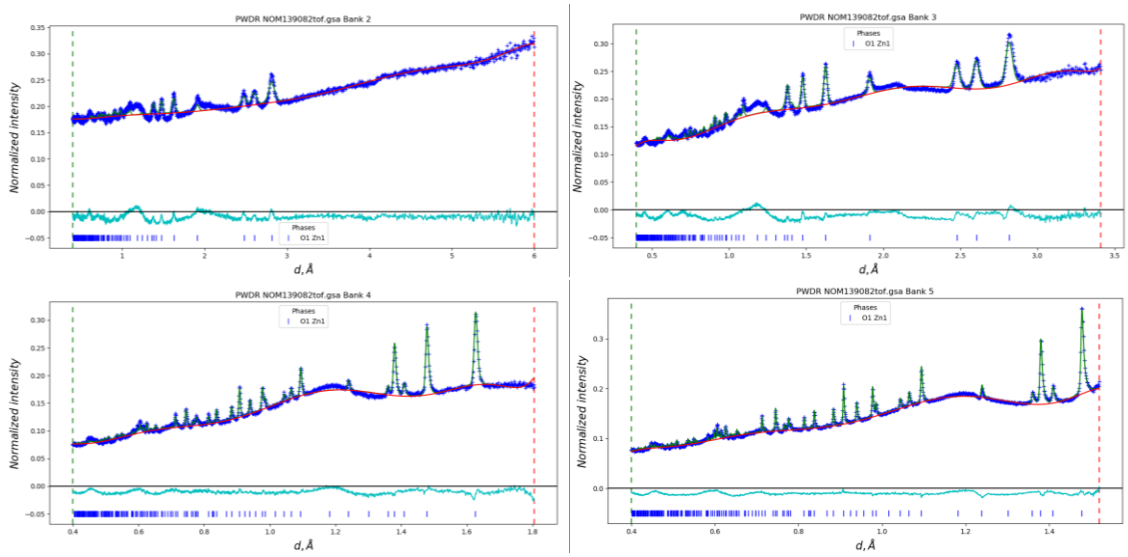

Figure 79. Rietveld refinment on the Bragg peaks from the neutron total scattering data for Zn-MOF-74 calcined under N_2 at 600 °C.

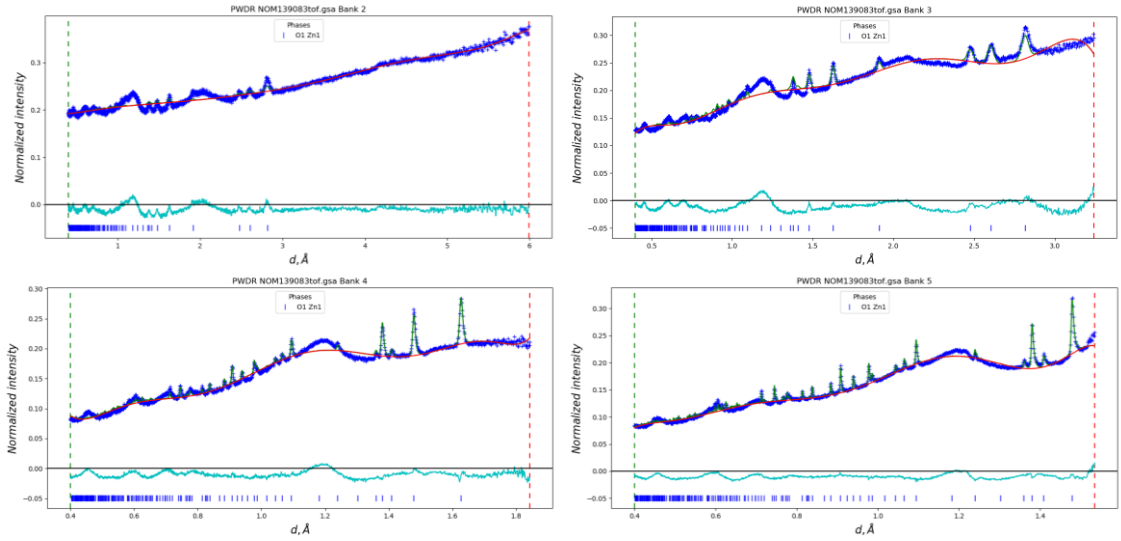

Figure 80. Rietveld refinment on the Bragg peaks from the neutron total scattering data for Zn-MOF-74 calcined under N_2 at 700 °C.

The UiO-66 calcined samples were refined only as cubic ZrO_2. The neutron diffraction data of the 500 °C calcined data exhibited no noticeable diffraction peaks representative of UiO-66. However, much of this is due to the large hydrogen content of UiO-66, which caused significant incoherent scattering from the residual UiO-66 material in the sample. The three samples all generally showed nanoscale ZrO_2 (**Table 9, Figure 81-83**). However, the N_2 sample in particle had a strong background signal due to the large hydrogen content of the sample. As this sample also contained limited ZrO_2 content, the information that can be gleaned from this data set is limited. For comparison, the 700 °C N_2 calcined sample shows a large improvement in scattering intensity due to zirconium oxide fit to the cubic phase, similar to the laboratory scale data (**Figure 84**). The refined particle size for the neutron data is similar to the X-ray data (7.2 vs. 6.2 nm), further confirming the rough scale for the material.

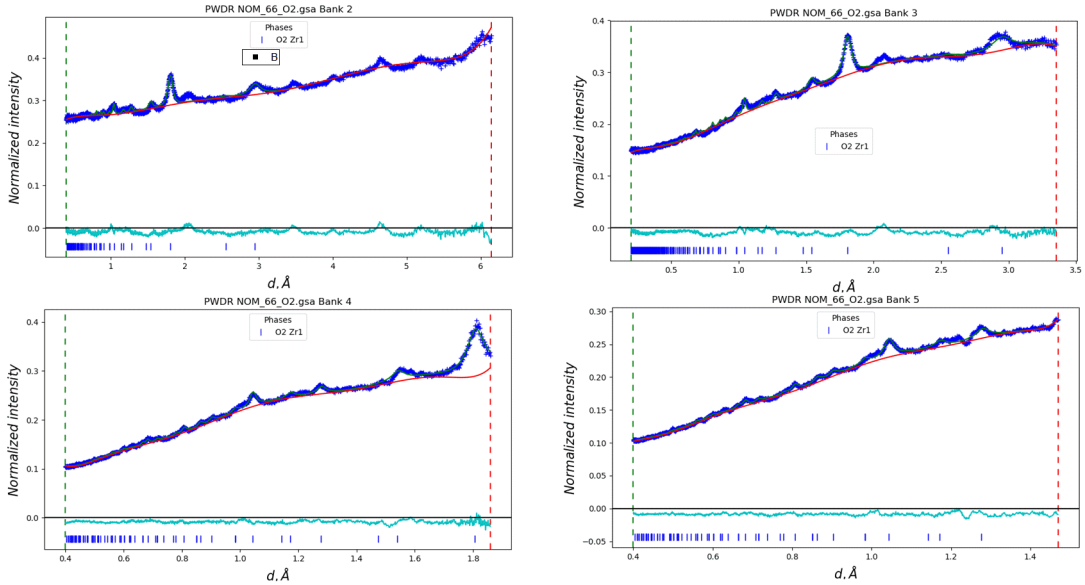

Figure 81. Rietveld refinement on the Bragg peaks from the neutron total scattering data for UiO-66 calcined under air at 500 °C

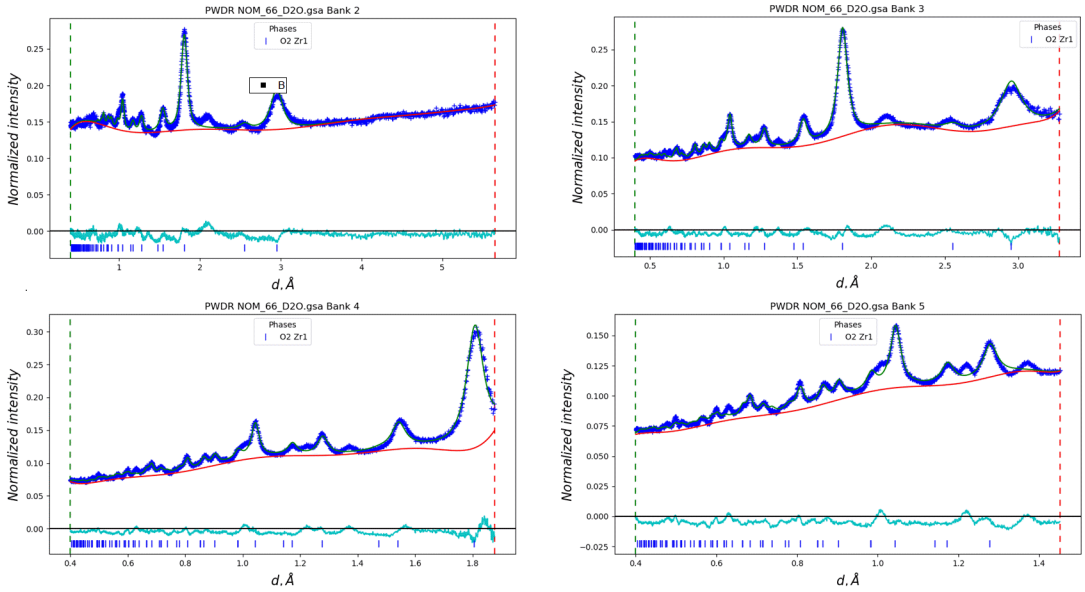

Figure 82. Rietveld refinement on the Bragg peaks from the neutron total scattering data for UiO-66 calcined under D_2O at 500 °C. The data was fit solely to ZrO_2 (cubic) as the leftover UiO-66 Bragg peaks could not be resolved due to the incoherent scattering of the large amount of residual hydrogen.

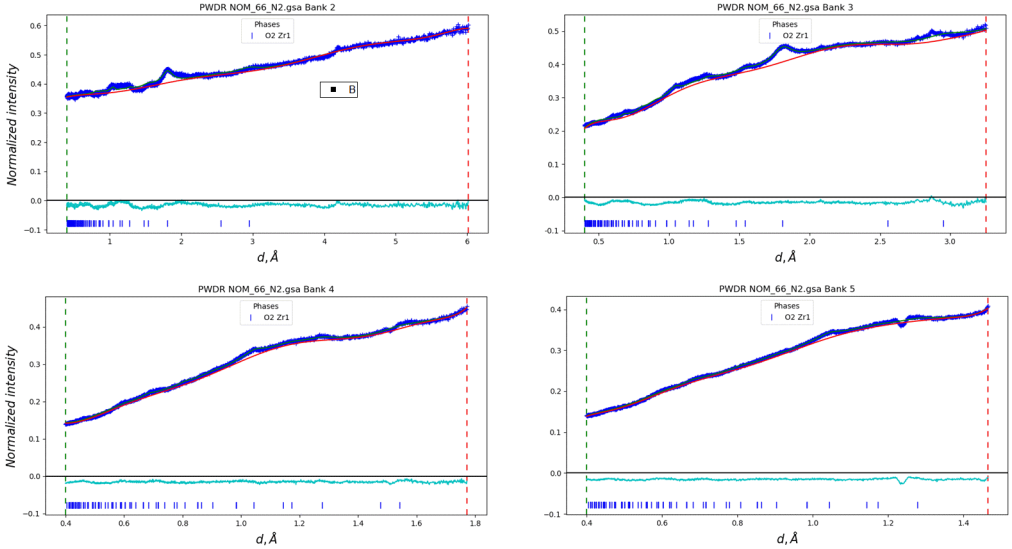

Figure 83. Rietveld refinement on the Bragg peaks from the neutron total scattering data for UiO-66 calcined under N_2 at 500 °C. The data was fit solely to ZrO_2 (cubic) as the leftover UiO-66 Bragg peaks could not be resolved due to the incoherent scattering of the large amount of residual hydrogen.

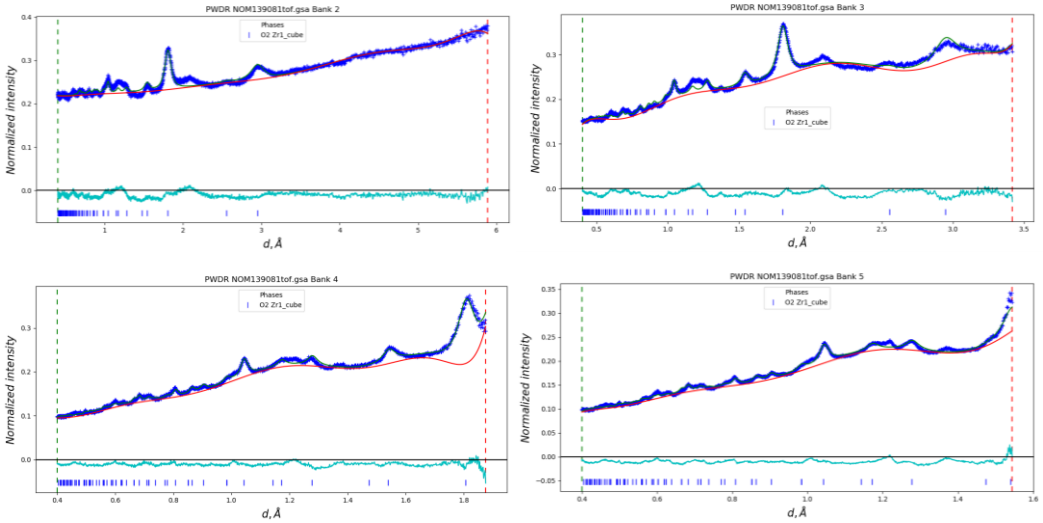

Figure 84. Rietveld refinement on the Bragg peaks from the neutron total scattering data for UiO-66 calcined under N_2 at 700 °C. The refinement is fit to cubic phase zirconia, the same as the X-ray data.

The total scattering results were analyzed via PDF methods using the software PDFgui (**Figure 85**).[280] The fits for the Zn-MOF-74 based samples were refined using the

known structure of ZnO, with the D_2O and N_2 calcined samples were refined against graphitic carbon. In addition, two model structures, one containing O-D bonds constructed in a cube and the other containing C-H bonds in the same arrangement, were used to simulate surface-bound deuteroxides (D_2O sample only) and residual hydrogen respectively. These models were constructed with C or O atoms at the vertices of a cube and with H or D atoms along the edge of the cube. The lattice lengths of the cubes were set to twice the length of an O-D or C-H bond to simulate the correct bond distances. Both structures were truncated to 1.5 Å in the PDF fit. All structures were refined by their scale factor, their unit cell parameters, and the atomic displacement parameters for all atoms in the system. The ZnO and graphitic carbon samples were also refined on a linear atomic correlation factor, and their symmetry restrained atomic positions. Also, the domain sizes of the ZnO and the graphitic carbon were modeled using an empirical spherical shape function.[288]

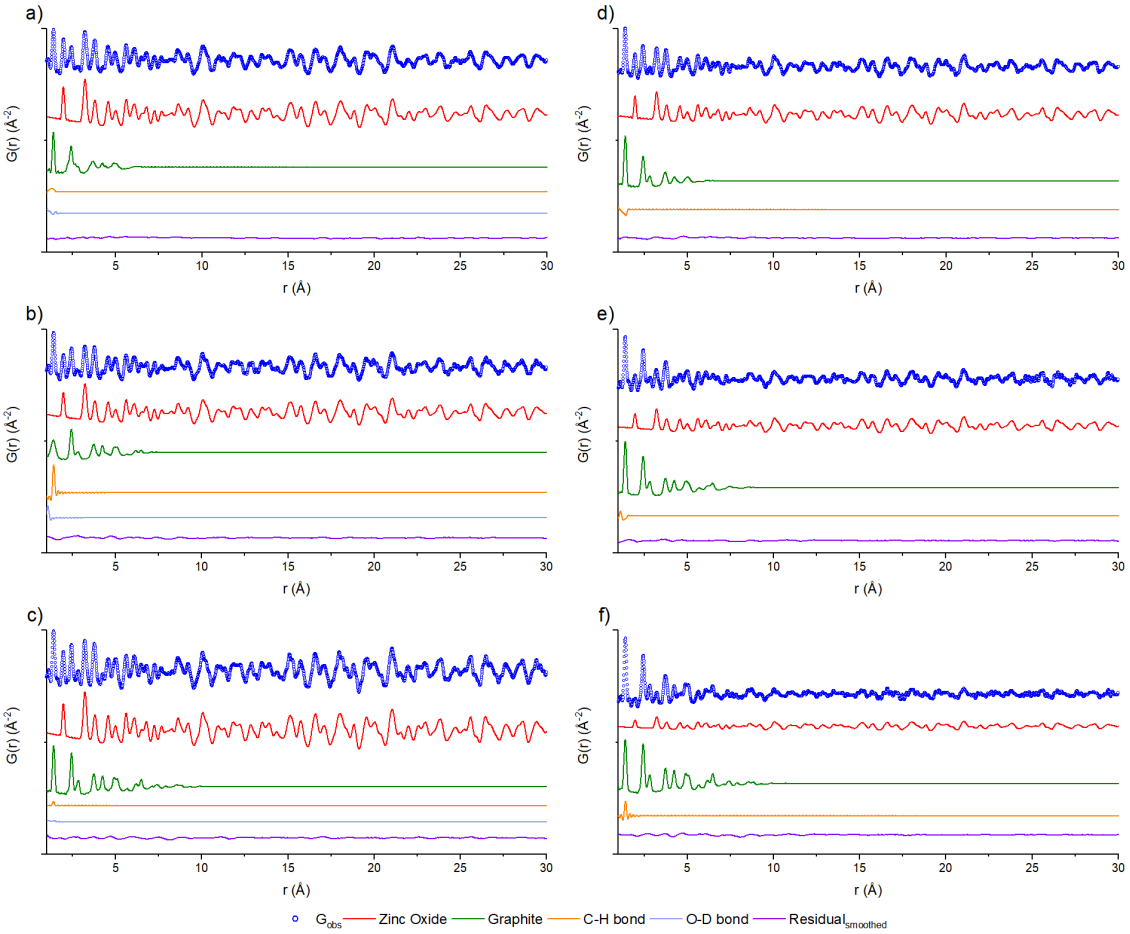

Figure 85. Pair Distribution function (PDF) fits for Zn-MOF-74 calcined under D_2O at a) 500 °C, b) 600 °C, and c) 700 °C alongside Zn-MOF-74 calcined under N_2 at d) 500 °C, e) 600 °C, and f) 700 °C. The fits were performed using ZnO, graphite, as well as model structures containing O-D (for D_2O) and C-H (for D_2O and N_2) to account for adsorbed D_2O as well as uncombusted C-H bonds within the materials.

The air calcined sample, consisting solely of ZnO, was refined to a domain size of 45.7 nm, which is relatively consistent with the Rietveld refinement results of 106 nm. Although, as the PDF fits are only to 3 nm, the exact value afforded by the spherical shape function is of limited use for this specific ZnO fit. Meanwhile, the 500 °C D_2O and the N_2 calcined samples were both refined to 11.6 and 26.9 nm, respectively. By increasing the

calcination temperatures to 600 °C and 700 °C, we were able to increase the ZnO domain size to 16.60 and 46.61 nm, respectively for D_2O, and 24.62 and 29.40 nm for N_2 (**Table 11**). The general increase in ZnO domain size is likely due to the sintering process occurring during calcination that was observed in the SEM. Based on SEM imaging, there is a general increase in the uniformity of the ZnO tube developing on the surface of the calcined Zn-MOF-74, which suggests that the ZnO is starting to transition from distinct nanoparticles into a bulk tube. The ZnO fits generally showed a minimal difference between the different samples, suggesting that there was only little local structural variation between the three samples and the average ZnO structure.

Table 11. Spherical Domain Size Parameters for Zn-MOF-74 Based MOFdCs

Gas	Temperature (°C)	Zinc Oxide Size (Å)	Graphite Size (Å)
Air	500	570.2	---
D_2O	500	116.1	7.4
D_2O	600	166.0	8.3
D_2O	700	466.1	11.5
N_2	500	268.8	7.0
N_2	600	246.2	10.2
N_2	700	294.0	11.9

Both the D_2O and the N_2 calcined samples had a secondary phase that consisted of graphitic carbon. This can be easily observed in the PDF results due to the presence of the distinct 1.4 Å peak, which is indicative of the sp^2 hybridized C-C bond in the graphene ring.[287] For the most part, the graphitic domains for all of the Zn-MOF-74 samples are sub-nanoscale, likely the result of limited interactions between the different ligands during the carbonization process. Interestingly, the domain size increases as a function of calcination temperature, with the 700 °C calcined Zn-MOF-74 samples having graphitic

domains greater than 1 nm (**Table 10**). This increase in graphitic order with temperature was also matched by an increase in surface area as a function of temperature for both the D_2O and N_2 calcined samples. Interestingly, despite the general trend of surface area being linearly related to the residual carbon content, the 500 °C N_2 sample had a higher residual carbon content compared to the 500 °C D_2O sample (27.53% versus 22.97%) (**Table 7**), suggesting some correlation between the ordering of the porous carbon domains and the surface area of the MOFdCs. This corroborated our previous observations for PCN-250 (an iron-based MOF), where a higher carbon content, within a lower carbon ordered material, still had reduced porosity.[184] While the general trend of surface area increasing with graphitic carbon ordering holds true for the samples calcined at higher temperatures, with the highest degree of ordering observed in the 700 °C N_2 calcined sample, which also had the highest surface area, it does not appear to be a linear relationship. The 700 °C D_2O calcined sample exhibits a graphitic carbon domain size of 11.5 Å, only 0.4 Å below that of the 700 °C N_2 calcined sample despite having a surface area of only 292 m^2/g as opposed to the 646 m^2/g surface area of the 700 °C N_2 calcined sample. However, the D_2O samples show a significant jump in graphitic ordering going from 600 °C to 700 °C, which could suggest that at that temperature, there is a noticeable change in the processes governing graphite growth, such as a sintering type effect or a more efficient dehydrogenation. It should be noted that UiO-66 calcined under N_2 at 700 °C also exhibits a >1 nm graphite domain size (10.7 Å), even though the generally low surface area of the UiO-66 derived carbons.

The variation in ordering as a function of temperature for both D_2O (a) and N_2 (b) can be observed in **Figure 86**. There is a general similarity in the intensity of the graphitic carbon peaks between the two different calcination gases. The 500 °C D_2O sample, despite having a lower carbon content (4.56%) compared to the 500 °C N_2 sample, has only a slightly higher (3%) intensity at the 1.4 Å peak, suggesting that there was a significant amount of carbon atoms that did not contribute to the graphitic ordering. This could in part be attributed to the higher hydrogen content of the N_2 calcined samples (1.31% versus 1.06%), which was also captured in the fit of the C-H bonds, where the N_2 calcined samples have a noticeably higher scale factor as compared to the D_2O calcined samples (0.0195 versus 0.00660).

However, while going to higher temperatures under D_2O does not result in any significant changes in total carbon content, only a slight decrease from 22.97% to 21.34% is observed going from 500 to 700 °C, there is a significant increase in total carbon content for the N_2 calcined samples, 27.53% to 31.96% to 45.81% for 500, 600, and 700 °C respectively. This corresponds strongly with an increase in surface area for these samples. However, the correlation between graphitic carbon domain size and surface area, while present, is much weaker (**Figure 87a**). Despite this, there is a still a stronger correlation between graphitic carbon domain size and surface area, than there is with total residual carbon content (**Figure 87b**), which suggests that a higher degree of carbon ordering does play some role, in addition to the general total carbon content, on the bulk porosity of these materials. Interestingly, despite the generally low ordering of these graphitic domains, with only a few examples greater than 1 nm, the domain sizes are still larger than what we

would expect for materials only ordered through templating from individual organic ligands. Even amongst the 500 C calcined samples, there is still significant ordering in the 5 to 7 Å range, which corresponds to the ordering of multiple C_6 graphitic rings, with each ring fitting to approximately 2.85 Å in diameter.[289] This is potentially due to some degree of longer range templating effect from the MOF. While there is a potential for a sintering or general long-distance bulk graphitization, those processes typically do not occur below 1000 °C, with many processes not occurring until 2000 or even 3000 °C, suggesting that some of this ordering is indeed due to the MOF structure.[306]

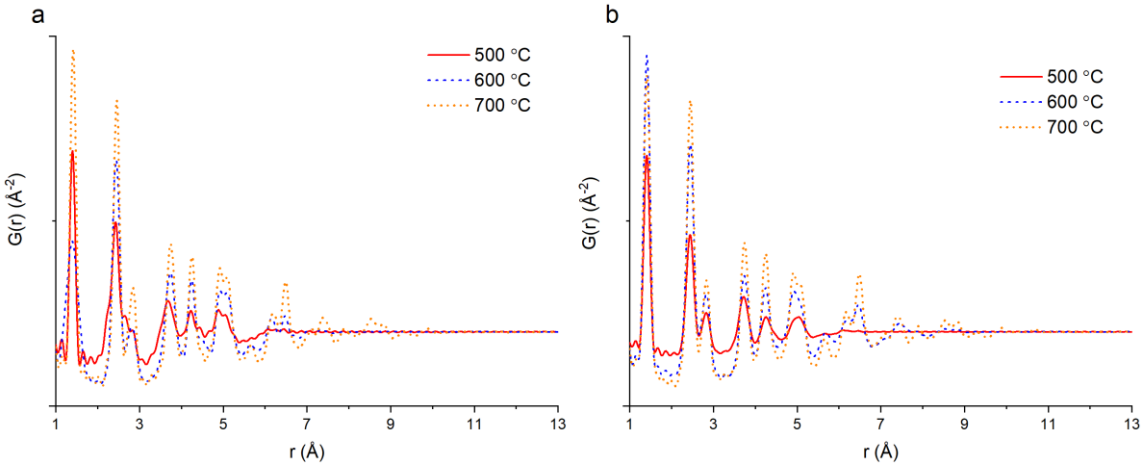

Figure 86. Comparison of the PDF graphitic carbon fits for the Zn-MOF-74 samples calcined under a) D_2O and b) N_2 at 500 °C (red line) 600 °C (blue dashes) and 700 °C (orange dots). There is a noticeable increase in graphitic carbon ordering as the calcination temperature increases.

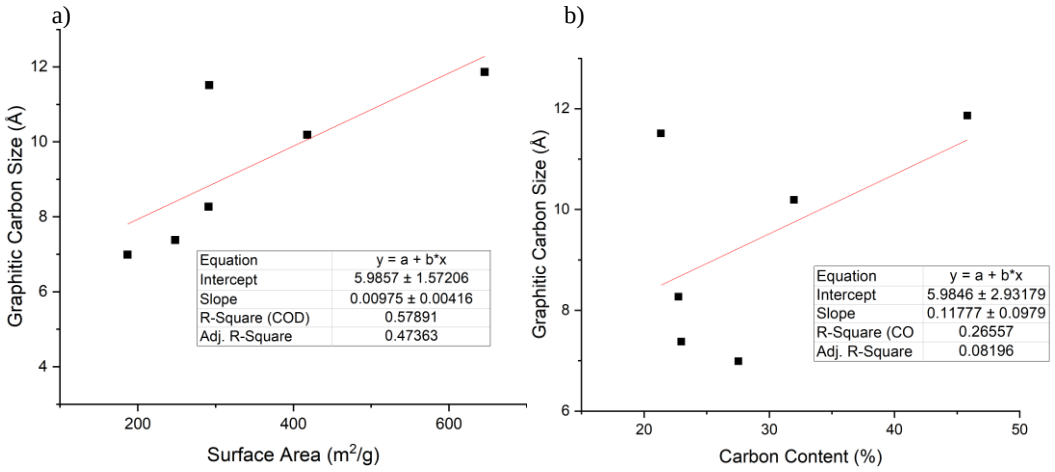

Figure 87. a) Surface area versus graphitic carbon domain size for Zn-MOF-74 derived carbons, b) Total carbon content versus graphitic carbon domain size for Zn-MOF-74 derived carbons.

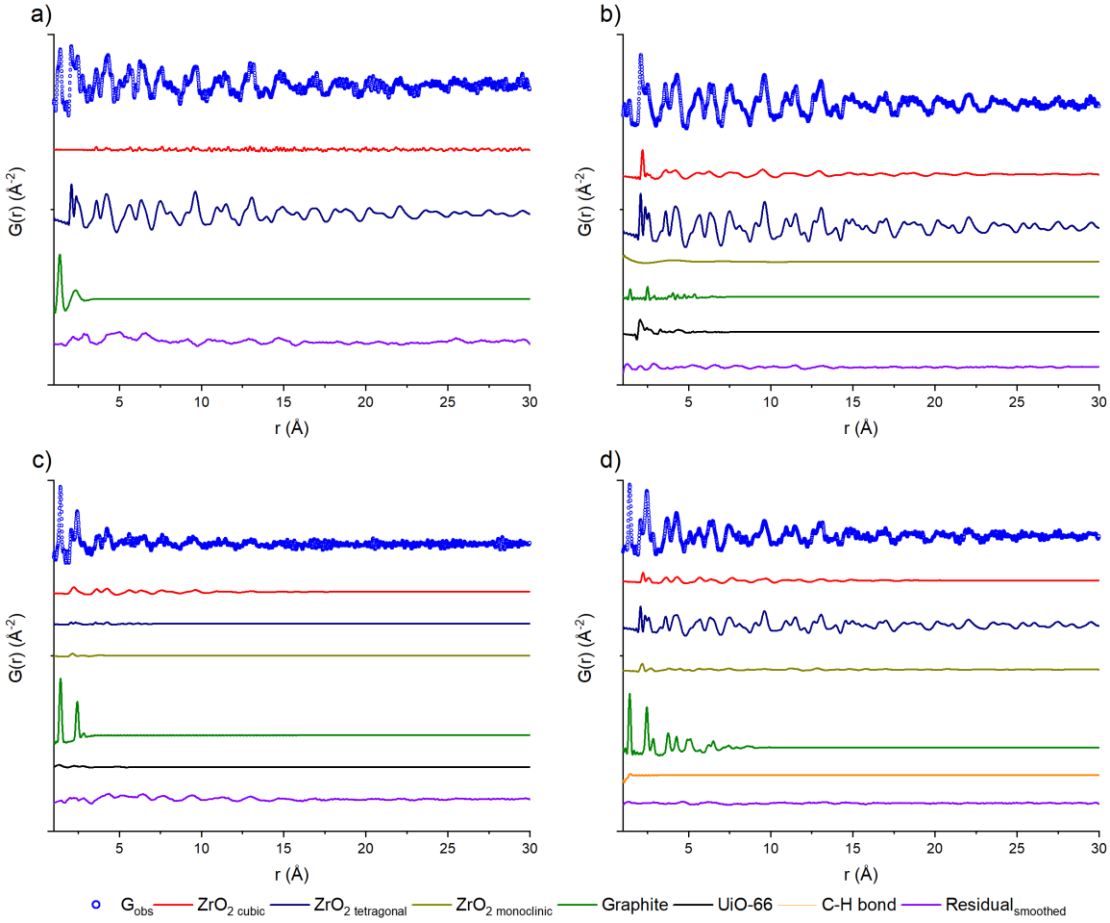

Figure 88. PDF fitting of UiO-66 calcined at 500 °C under a) air, b) D_2O, c) N_2 as well as UiO-66 calcined under N_2 at 700 °C.

The PDF fittings of the 500 °C calcined UiO-66 samples, as well as the 700 °C N_2 calcined sample, were mainly used for the determination of the composition of the zirconium oxide species that was formed. Specifically, the local structural order was determined to see if it matched that of the cubic phase. The samples matched the long-range Bragg diffraction ordering of the cubic phase. Still, the potential for contributions from the tetragonal or the monoclinic phase in the local structure was also tested to ensure the fit in the data was indeed not from these phases (**Figure 88**). A full PDF fit for each of the four samples was performed using a combination of 6 phases, cubic, tetragonal, and monoclinic zirconia, graphite, as well a dehydroxylated UiO-66 phase (for the 500 °C calcined samples) or a C-H bond phase (for the 700 °C calcined sample). The air calcined sample, despite only having 0.6%wt carbon, still showed the distinctive graphitic structure. However, it was generally broad and did not extend beyond 3 Å (**Table 12**). The graphitic carbon phases of both the D_2O and the 500 °C N_2 calcined samples were slightly better defined. However, the N_2 sample only showed ordering out to about 2.4 Å, which corresponds most readily to a 3-carbon interaction in a graphitic unit (**Table 12**). The D_2O calcined sample showed ordering out to slightly higher r value. However, the overall scale, especially relative to the other phases in this data set, is quite low, suggesting that there is only a small degree of graphitic carbon in the D_2O calcined sample system. Of the three ZrO_2 phases, the monoclinic phase showed the smallest contribution to the overall structures of the sample. There was no contribution of this phase in the air calcined sample and only minor contributions of this phase in the other three samples. This result was consistent with the high symmetry system evident from the Bragg diffraction peaks in the

samples. The tetragonal phase appeared to give the highest contribution to the structure for the air, D_2O, and 700 °C N_2 calcined samples, with only a minor contribution from the cubic phase of these samples. However, as the two phases mainly differ in the lower r region (below 5 Å, **Figure 89**), the fitting likely showed a preference for the tetragonal phase due to the better low range r fit for this phase, reducing the potential contribution from the other phases. The 500 °C N_2 calcined sample shows a generally weak signal, which corresponds well with the high hydrogen background inferred from the reciprocal space data, making proper real space analysis difficult at best.

Table 12. Spherical Domain Size Parameters for UiO-66 Based MOFdCs

Gas	Temperature (°C)	Cubic Zirconia Size (Å)	Tetragonal Zirconia Size (Å)	Monoclinic Zirconia Size (Å)	Graphite Size (Å)	UiO-66-dehydroxylated Size (Å)
Air	500	223.8	45.3	---	3.2	---
D_2O	500	42.3	47.5	12.3	8.1	8.5
N_2	500	18.7	9.9	11.3	3.7	10.6
N_2	700	25.6	52.8	41.1	10.7	---

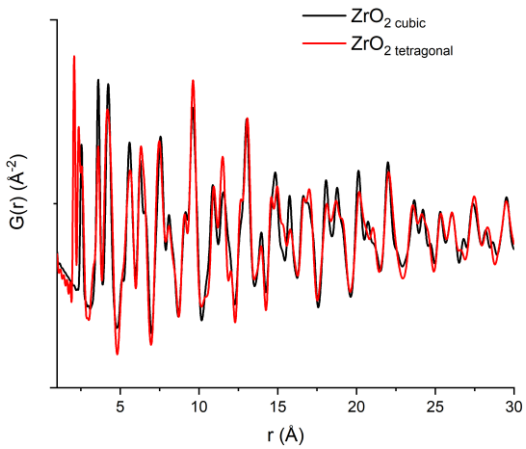

Figure 89. Calculated PDF for cubic phase (black) and tetragonal phase (red) ZrO_2, showing minimal differences at high r.

Conclusions

This work shows the variation in MOFdC structure formation as a function of both the calcination gas environment and temperature. As part of this work, two common MOF materials, Zn-MOF-74 and UiO-66, were calcined at various temperatures under multiple gas environments. The resulting MOFdCs exhibited varying degrees of residual carbon content, with the amount of carbon being partially correlated to the surface area of the resulting material. In general, the surface areas of the derived carbons tend to decrease when gases with a higher coordination affinity towards the metal centers are used. Samples calcined under CO_2 and D_2O atmospheres typically resulted in lower surface areas, especially at higher temperatures. By increasing the calcination temperature, we also observed an increase in the metal oxide domain size. This was especially apparent in the study of Zn-MOF-74, wherein the nanoscale ZnO centers began to sinter together at temperatures above 500 °C. This sintering process mainly occurred on the surface of the rod-shaped Zn-MOF-74, resulting in the production of unusual ZnO tubes filled with a porous carbon interior. This process was observed to occur, despite being performed at temperatures below the $T_m/2$ cutoff, the typical cutoff for powder sintering, due to the nanoscale nature of the metal oxide species. Additionally, it was observed that the calcination of UiO-66 resulted in the formation of cubic zirconia, despite the lower stability of the cubic phase relative to the tetragonal or monoclinic at these temperatures. This data suggests that MOFdCs could potentially provide a means for using templated synthesis to stabilize unusual structural or chemical phases.

Analysis of the nanoscale features of these materials was performed via neutron total scattering and PDF analysis. The PDF analysis was utilized to investigate the relative degree of ordering within the graphitic carbon scaffolds. These results suggested that the surface area of the MOFdC materials is related to the local scale graphitic ordering, in addition to the total carbon content. The more highly ordered materials showed a higher surface area. The results described herein are currently being utilized to generate tunable porous carbon materials with well-controlled nanoscale metal oxides for their use in catalytic applications.

CHAPTER V

CONCLUSIONS AND OUTLOOK

Conclusions

The research discussed herein focused on a few aspects of amorphous porous material development. In the first project, Improving Alkylamine Incorporation in Porous Polymer Networks Through Dopant Incorporation,[88] I focused on the synthetic control of an amorphous porous polymer network through the addition of dopant molecules. I focused on how the interaction and subsequent structural alteration brought upon by the incorporation of cyanuric acid, resulted in an improved CO_2 capture performance. Within this work, I mainly focused on how the structure affected the application properties, mainly CO_2 cycling and amine loss. However, one of the major issues associated with the project was a challenging analysis of the material. The bulk amorphous nature of the material prohibited investigation into its structure, and even solid-state spectroscopic techniques could only give broad, undetailed information on the potential mechanisms of this material's CO_2 capture capabilities.

The development of PPN-151-DETA mainly focused on the synthesis of robust and scalable material for CO_2 capture applications. To that end, the project was successful, and we were able to synthesize the material at the 200 g scale. Indeed, scaling the material provided some added opportunity to investigate the structure to a greater degree, as we were able to study the reaction conditions for the parent PPN in more detail. Additionally, the use of CO_2 isotherm analysis and *in situ* IR spectroscopy allowed for the investigation into both the strength of the CO_2-sorbent interaction, as well as how the addition of the

dopant cyanuric acid altered the mechanism of adsorption from a primarily a physisorption mechanism to a chemisorption one.

The limited options available for the structural characterization of PPN-151-DETA led directly to my investigation of PDF methodologies as a means of elucidating structural information of amorphous materials. The carbon, nitrogen, and oxygen-based structure of PPN-151 made it ill-suited for PDF analysis via X-ray scattering. In contrast, the high hydrogen content of the material made it unsuitable for investigation via neutron scattering. Additionally, the structural collapse of MOFs under different conditions, exemplified by our investigation of decarboxylation mechanisms in PCN-250,[169] instilled an interest in controlled decomposition pathways of MOFs. This combination of factors resulted in the investigation into the MOFdCs, the decomposed framework materials derived from MOF thermolysis through the use of neutron total scattering.

While it was well understood that the metal phases within MOFdCs tend to form into nanoscale metal oxides,[189] there was less of an understanding regarding the structure of the residual carbon scaffold. To that end, neutron total scattering was utilized, as the neutron scattering length for carbon is relatively large compared to that for the heavier metal ions embedded within the structure. The resulting manuscript, "Metal Oxide Decorated Porous Carbons from Controlled Calcination of a Metal-Organic Framework," [184] showcased the analysis of this carbon scaffold. This provided both phase information, showing that the structure is graphitic in nature, as well as graphitic carbon domain sizes, both of which are typically lacking in descriptions of MOFdCs.[184] In particular, I showed that there is a positive correlation between residual carbon content and surface area, with

the ordering of the graphitic carbon also playing a role in determining the material surface area. Additionally, the use of neutron scattering allowed us to better understand how nanoscale effects alter the magnetic properties of iron-based nanoparticles, with the total scattering data showing some perturbations of the spins in the nanoscale iron (II,III) oxide phase.

The final piece of work in this thesis, Using Metal-Organic Frameworks as Templates for Shape and Phase Controlled Carbons, is an extension of my interest in the structural elucidation of these materials. Here the focus was on the effect of not only the gas environment but also temperature. Additionally, the investigation of two different MOFs with different connectivities and decomposition temperatures showed the difficulty in assigning universal descriptors to MOFdC formation, with the parameters being heavily dependent on the chemical structure of the parent material. In addition, similar to PCN-250, the results showed that oxidation states and phases could be altered through calcination conditions. This work showed that different phases can be observed in the non-redox active zirconia when formed from MOF calcination. The well segregated and geometrically defined zirconium oxo clusters in UiO-66 helped stabilize the formation of tetragonal ZrO_2, showing the benefits of MOF scaffolding in stabilizing distinct structural forms.

Outlook

The development of a PPN-based material for CO_2 capture is a promising area of research. While the non-covalent tethering was shown to improve the cycling performance at the laboratory scale, testing at a larger scale showed that there was still some amine

loss. Therefore, we will continue to investigate methods to further improve the tethering process. The core plan to keep costs low by limiting the number of synthetic steps will still be utilized for future optimization of the target sorbent, with the focus shifting more towards improved ionic interactions between the amine and the PPN through the incorporation of sulfonic acid groups at the melamine nitrogen sites. The acidic sulfonic acids can then engage in an acid-base interaction with the active amine component. Ionic interactions have the benefit of improving not only the interaction efficiency of the amine but also having some degree of CO_2 affinity themselves through anion-CO_2 interactions.

The research in the area of MOFdCs will expand to mixed-metal-based PCN-250 and templated zirconia-based species through the use of Zr/Ti clusters. The work will determine the effect of templating when using altered cluster geometries. The tri-nuclear iron cluster of PCN-250 can be made in mixed-metal variants, typically in the form of Fe_2M.[168] Hence, future work on these materials will focus on the generation of the mixed-valent M_3O_4 phases through calcination under weakly oxidative conditions, such as CO_2 and D_2O, as these appear to stabilize the formation of the nanoscale phases. These materials have potentially interesting magnetic properties due to both their mixed-metal and nanoscale nature. Analysis of these materials through neutron scattering techniques will continue, as neutrons are particularly suited for determining how the different metal species are organized within the nanoparticles. We are particularly interested in investigating if the templating approach allows for an ordered mixed-metal phase, or if there is any partial segregation of the metal centers. The analysis should be relatively straightforward to determine due to the different neutron scattering lengths of the target

metal centers. There is also the potential to investigate these materials as catalysts for aqueous phase pollutant degradation, where the ability to separate the active species could be highly valuable.

Final Comments

The overarching theme of this body of work is best described as an attempt to characterize amorphous porous materials. Through the first project, characterization was mainly focused on the application side of material development. While this provided us with opportunities to rationalize potential structures based upon the material's behavior, it did not offer much in the way of conclusive evidence. Meanwhile, investigation of MOFdCs, well-known in the literature for applications, had the potential for structural characterization via neutron total scattering and PDF methodologies. The use of these techniques allowed us to bridge some of the gaps between the structure and property relationship in amorphous porous materials. Future work will expand upon the use of PDF methodologies, both neutron and X-ray based, to investigate even further varieties of amorphous materials.

REFERENCES

1. Bryan, C. P., *Ancient Egyptian medicine: the papyrus ebers*. Ares Chicago: 1974.

2. Partington, J. R., *Origins and Development of Applied Chemistry*. Longmans, Green & Co.: 1935.

3. Çeçen, F.; Aktaş, Ö., Water and Wastewater Treatment: Historical Perspective of Activated Carbon Adsorption and its Integration with Biological Processes. In *Activated Carbon for Water and Wastewater Treatment*, 2011; pp 1-11.

4. Diamond, E. M.; Farrer, K. T. H., WATERING THE FLEET AND THE INTRODUCTION OF DISTILLATION. *The Mariner's Mirror* **2005,** *91* (4), 548-553.

5. Struhsaker, T. T.; Cooney, D. O.; Siex, K. S., Charcoal Consumption by Zanzibar Red Colobus Monkeys: Its Function and Its Ecological and Demographic Consequences. *International Journal of Primatology* **1997,** *18* (1), 61-72.

6. Scheele, C. W.; Johnson, J.; Forster, J. R.; Priestley, J.; Kirwan, R.; Bergman, T., *Chemical observations and experiments on air and fire*. printed for J. Johnson: 1780.

7. Beck, C. W., Georg Ernst Stahl, 1660-1734. *Journal of Chemical Education* **1960,** *37* (10), 506.

8. Browne, C. A., The origins of sugar manufacture in America. II. A sketch of the history of sugar refining in America. *Journal of Chemical Education* **1933,** *10* (7), 421.

9. Leicester, H. M., Tobias Lowitz—Discoverer of basic laboratory methods. *Journal of Chemical Education* **1945,** *22* (3), 149.

10. Deitz, V. R.; Standards, U. S. N. B. o., *Bibliography of Solid Adsorbents: An Annotative Bibliographical Survey of the Scientific Literature on Bone Char, Activated Carbons, and Other Technical Solid Adsorbents, for the Years 1900 to 1942 Inclusive*. National Bureau of Standards: 1944.

11. *The Repertory of Patent Inventions: And Other Discoveries and Improvements in Arts, Manufactures, and Agriculture*. T. and G. Underwood: 1812.

12. Andersen, A. H., Experimental Studies on the Pharmacology of Activated Charcoal. *Acta Pharmacologica et Toxicologica* **1946,** *2* (1), 69-78.

13. Juurlink, D. N., Activated charcoal for acute overdose: a reappraisal. *Br J Clin Pharmacol* **2016,** *81* (3), 482-487.

14. Woodhead, G. S.; Wood, G. E. C., An Inquiry Into The Relative Efficiency Of Water Filters In The Prevention Of Infective Disease. *The British Medical Journal* **1894,** *2* (1767), 1053-1059.

15. *English Patents of Inventions, Specifications: 1862 (1863), 2858 - 2931*. H.M. Stationery Office: 1863.

16. Spiers, E. M. In *The Gas War, 1915–1918: If not a War Winner, Hardly a Failure*, One Hundred Years of Chemical Warfare: Research, Deployment, Consequences, Cham, 2017//; Friedrich, B.; Hoffmann, D.; Renn, J.; Schmaltz, F.; Wolf, M., Eds. Springer International Publishing: Cham, 2017; pp 153-168.

17. Derlet, R. W.; Albertson, T. E., Activated charcoal--past, present and future. *West J Med* **1986,** *145* (4), 493-496.

18. Flanigen, E. M.; Broach, R. W.; Wilson, S. T., Introduction. *Zeolites in Industrial Separation and Catalysis* **2010**, 1-26.

19. Gusenius, E. M., Beginnings of Greatness in Swedish Chemistry (II) Axel Fredrick Cronstedt (1722-1765). *Transactions of the Kansas Academy of Science (1903-)* **1969,** *72* (4), 476-485.

20. Cronstedt, A. F.; Schlenker, J. L.; Kühl, G. H., OBSERVATIONS AND DESCRIPTIONS: On an Unknown Mineral-Species Called Zeolites. In *Proceedings from the Ninth International Zeolite Conference*, von Ballmoos, R.; Higgins, J. B.; Treacy, M. M. J., Eds. Butterworth-Heinemann: 1993; pp 3-9.

21. Colella, C.; Gualtieri, A. F., Cronstedt's zeolite. *Microporous and Mesoporous Materials* **2007,** *105* (3), 213-221.

22. Gottardi, G., The genesis of zeolites. *European Journal of Mineralogy* **1989**, 479-488.

23. Bish, D. L.; Ming, D. W., *Natural Zeolites: Occurrence, Properties, Applications*. De Gruyter: 2018.

24. Sherman, J. D., Synthetic zeolites and other microporous oxide molecular sieves. *Proceedings of the National Academy of Sciences* **1999,** *96* (7), 3471.

25. Bragg, W. H.; Bragg, W. L., The Structure of the Diamond. *Nature* **1913,** *91* (2283), 557-557.

26. Pauling, L., THE STRUCTURE OF SOME SODIUM AND CALCIUM ALUMINOSILICATES. *Proceedings of the National Academy of Sciences* **1930,** *16* (7), 453.

27. Leonard, R. J., The hydrothermal alteration of certain silicate minerals. *Economic Geology* **1927,** *22* (1), 18-43.

28. Sainte-Claire-Deville, M. H., Chimie Minéralogique - Reproduction de la Lévyne. *Comptes Rendus de l'Académie des Sciences* **1862,** *54*, 324-327.

29. Lamb, A. B.; Woodhouse, J. C., Adsorption by Dehydrated Chabasite as a Function of the Water Content. *Journal of the American Chemical Society* **1936,** *58* (12), 2637-2646.

30. Barrer, R. M., 33. Synthesis of a zeolitic mineral with chabazite-like sorptive properties. *Journal of the Chemical Society (Resumed)* **1948,** (0), 127-132.

31. Barrer, R. M., 435. Syntheses and reactions of mordenite. *Journal of the Chemical Society (Resumed)* **1948,** (0), 2158-2163.

32. Milton, R. M., Molecular Sieve Science and Technology. In *Zeolite Synthesis*, American Chemical Society: 1989; Vol. 398, pp 1-10.

33. Milton, R. M., Molecular sieve adsorbents. Google Patents: 1959.

34. Bukata, S. W.; Castor, C. R.; Milton, R. M., Catalytic materials. Google Patents: 1961.

35. Flanigen, E. M., Chapter 2 Zeolites and molecular sieves: An historical perspective. In *Studies in Surface Science and Catalysis*, van Bekkum, H.; Flanigen, E. M.; Jacobs, P. A.; Jansen, J. C., Eds. Elsevier: 2001; Vol. 137, pp 11-35.

36. Gesser, H. D.; Goswami, P. C., Aerogels and related porous materials. *Chemical Reviews* **1989,** *89* (4), 765-788.

37. Beck, J. S.; Vartuli, J. C.; Roth, W. J.; Leonowicz, M. E.; Kresge, C. T.; Schmitt, K. D.; Chu, C. T. W.; Olson, D. H.; Sheppard, E. W.; McCullen, S. B.; Higgins, J. B.; Schlenker, J. L., A new family of mesoporous molecular sieves prepared with liquid crystal templates. *Journal of the American Chemical Society* **1992,** *114* (27), 10834-10843.

38. Kistler, S. S., Coherent Expanded Aerogels and Jellies. *Nature* **1931,** *127* (3211), 741-741.

39. Barron, R. F.; Nellis, G. F., *Cryogenic Heat Transfer*. CRC Press: 2017.

40. Gash, A. E.; Tillotson, T. M.; Satcher Jr, J. H.; Hrubesh, L. W.; Simpson, R. L., New sol–gel synthetic route to transition and main-group metal oxide aerogels using inorganic salt precursors. *Journal of Non-Crystalline Solids* **2001,** *285* (1), 22-28.

41. Cantin, M.; Casse, M.; Koch, L.; Jouan, R.; Mestreau, P.; Roussel, D.; Bonnin, F.; Moutel, J.; Teichner, S. J., Silica aerogels used as Cherenkov radiators. *Nuclear Instruments and Methods* **1974,** *118* (1), 177-182.

42. Yoldas, B. E.; Annen, M. J.; Bostaph, J., Chemical Engineering of Aerogel Morphology Formed under Nonsupercritical Conditions for Thermal Insulation. *Chemistry of Materials* **2000,** *12* (8), 2475-2484.

43. Jones, S. M., Aerogel: Space exploration applications. *Journal of Sol-Gel Science and Technology* **2006,** *40* (2), 351-357.

44. Brownlee, D., The Stardust Mission: Analyzing Samples from the Edge of the Solar System. *Annual Review of Earth and Planetary Sciences* **2014,** *42* (1), 179-205.

45. mars.nasa.gov The Rover's Temperature Controls. https://mars.nasa.gov/mer/mission/rover/temperature/.

46. Severn, J. R., Methylaluminoxane (MAO), Silica and a Complex: The "Holy Trinity" of Supported Single-Site Catalyst. *Tailor-Made Polymers* **2008**, 95-138.

47. Kresge, C. T.; Leonowicz, M. E.; Roth, W. J.; Vartuli, J. C.; Beck, J. S., Ordered mesoporous molecular sieves synthesized by a liquid-crystal template mechanism. *Nature* **1992,** *359* (6397), 710-712.

48. Zhao, D.; Feng, J.; Huo, Q.; Melosh, N.; Fredrickson, G. H.; Chmelka, B. F.; Stucky, G. D., Triblock Copolymer Syntheses of Mesoporous Silica with Periodic 50 to 300 Angstrom Pores. *Science* **1998,** *279* (5350), 548.

49. Katiyar, A.; Yadav, S.; Smirniotis, P. G.; Pinto, N. G., Synthesis of ordered large pore SBA-15 spherical particles for adsorption of biomolecules. *Journal of Chromatography A* **2006,** *1122* (1), 13-20.

50. Zhao, J.; Gao, F.; Fu, Y.; Jin, W.; Yang, P.; Zhao, D., Biomolecule separation using large pore mesoporous SBA-15 as a substrate in high performance liquid chromatography. *Chemical Communications* **2002,** (7), 752-753.

51. Pelrine, B. P.; Schmitt, K. D.; Vartuli, J. C., Olefin oligomerization catalyst. Google Patents: 1993.

52. Dosseh, G.; Xia, Y.; Alba-Simionesco, C., Cyclohexane and Benzene Confined in MCM-41 and SBA-15: Confinement Effects on Freezing and Melting. *The Journal of Physical Chemistry B* **2003,** *107* (26), 6445-6453.

53. Yamaguchi, T.; Yoshida, K.; Smirnov, P.; Takamuku, T.; Kittaka, S.; Takahara, S.; Kuroda, Y.; Bellissent-Funel, M. C., Structure and dynamic properties of liquids confined in MCM-41 mesopores. *The European Physical Journal Special Topics* **2007,** *141* (1), 19-27.

54. Yaghi, O. M.; Li, G.; Li, H., Selective binding and removal of guests in a microporous metal–organic framework. *Nature* **1995,** *378* (6558), 703-706.

55. Li, H.; Eddaoudi, M.; Groy, T. L.; Yaghi, O. M., Establishing Microporosity in Open Metal−Organic Frameworks: Gas Sorption Isotherms for Zn(BDC) (BDC = 1,4-Benzenedicarboxylate). *Journal of the American Chemical Society* **1998,** *120* (33), 8571-8572.

56. Lu, W.; Yuan, D.; Zhao, D.; Schilling, C. I.; Plietzsch, O.; Muller, T.; Bräse, S.; Guenther, J.; Blümel, J.; Krishna, R.; Li, Z.; Zhou, H.-C., Porous Polymer Networks: Synthesis, Porosity, and Applications in Gas Storage/Separation. *Chemistry of Materials* **2010,** *22* (21), 5964-5972.

57. Zhang, Y.; Riduan, S. N., Functional porous organic polymers for heterogeneous catalysis. *Chemical Society Reviews* **2012,** *41* (6), 2083-2094.

58. Bauman, W. C.; Eichhorn, J., Fundamental Properties of a Synthetic Cation Exchange Resin. *Journal of the American Chemical Society* **1947,** *69* (11), 2830-2836.

59. Abrams, I. M., High Porosity Polystyrene Cation Exchange Resins. *Industrial & Engineering Chemistry* **1956,** *48* (9), 1469-1472.

60. Pedersen, S.; Berge, A.; Jacobsen, H.; Leth-Olsen, K.-A.; Sæthre, B.; Ugelstad, J., Two-stage seed swelling procedure for producing monodisperse PVC particles. Google Patents: 2001.

61. Wang, Q. C.; Švec, F.; Fréchet, J. M. J., Fine control of the porous structure and chromatographic properties of monodisperse macroporous poly(styrene-co-divinylbenzene) beads prepared using polymer porogens. *Journal of Polymer Science Part A: Polymer Chemistry* **1994,** *32* (13), 2577-2588.

62. Geise, G. M.; Lee, H.-S.; Miller, D. J.; Freeman, B. D.; McGrath, J. E.; Paul, D. R., Water purification by membranes: The role of polymer science. *Journal of Polymer Science Part B: Polymer Physics* **2010,** *48* (15), 1685-1718.

63. Glater, J., The early history of reverse osmosis membrane development. *Desalination* **1998,** *117* (1), 297-309.

64. Lodish, H.; Berk, A.; Zipursky, S. L.; Matsudaira, P.; Baltimore, D.; Darnell, J., Osmosis, Water channels, and the regulation of cell volume. In *Molecular Cell Biology. 4th edition*, WH Freeman: 2000.

65. Hassler, G. L.; McCutchan, J. W., Osmosis through a Vapor Gap Supported by Capillarity. In *SALINE WATER CONVERSION*, American Chemical Society: 1960; Vol. 27, pp 192-205.

66. Ulbricht, M., Advanced functional polymer membranes. *Polymer* **2006,** *47* (7), 2217-2262.

67. Combe, C.; Molis, E.; Lucas, P.; Riley, R.; Clark, M. M., The effect of CA membrane properties on adsorptive fouling by humic acid. *Journal of Membrane Science* **1999,** *154* (1), 73-87.

68. Zhang, J.; Schott, J. A.; Mahurin, S. M.; Dai, S., Porous Structure Design of Polymeric Membranes for Gas Separation. *Small Methods* **2017,** *1* (5), 1600051.

69. Dechnik, J.; Gascon, J.; Doonan, C. J.; Janiak, C.; Sumby, C. J., Mixed-Matrix Membranes. *Angewandte Chemie International Edition* **2017,** *56* (32), 9292-9310.

70. Chen, J.-T.; Shih, C.-C.; Fu, Y.-J.; Huang, S.-H.; Hu, C.-C.; Lee, K.-R.; Lai, J.-Y., Zeolite-Filled Porous Mixed Matrix Membranes for Air Separation. *Industrial & Engineering Chemistry Research* **2014,** *53* (7), 2781-2789.

71. Lin, R.; Ge, L.; Hou, L.; Strounina, E.; Rudolph, V.; Zhu, Z., Mixed Matrix Membranes with Strengthened MOFs/Polymer Interfacial Interaction and Improved Membrane Performance. *ACS Applied Materials & Interfaces* **2014,** *6* (8), 5609-5618.

72. Wu, X.; Tian, Z.; Wang, S.; Peng, D.; Yang, L.; Wu, Y.; Xin, Q.; Wu, H.; Jiang, Z., Mixed matrix membranes comprising polymers of intrinsic microporosity and covalent organic framework for gas separation. *Journal of Membrane Science* **2017,** *528*, 273-283.

73. Slater, A. G.; Cooper, A. I., Function-led design of new porous materials. *Science* **2015,** *348* (6238), aaa8075.

74. Thomas, A., Functional Materials: From Hard to Soft Porous Frameworks. *Angewandte Chemie International Edition* **2010,** *49* (45), 8328-8344.

75. Yu, S.-B.; Lyu, H.; Tian, J.; Wang, H.; Zhang, D.-W.; Liu, Y.; Li, Z.-T., A polycationic covalent organic framework: a robust adsorbent for anionic dye pollutants. *Polymer Chemistry* **2016,** *7* (20), 3392-3397.

76. Li, B.; Zhang, Y.; Ma, D.; Shi, Z.; Ma, S., Mercury nano-trap for effective and efficient removal of mercury(II) from aqueous solution. *Nature Communications* **2014,** *5* (1), 5537.

77. Sun, Q.; Dai, Z.; Meng, X.; Xiao, F.-S., Porous polymer catalysts with hierarchical structures. *Chemical Society Reviews* **2015,** *44* (17), 6018-6034.

78. McKeown, N. B., Polymers of intrinsic microporosity. *ISRN Materials Science* **2012,** *2012*.

79. McKeown, N. B.; Gahnem, B.; Msayib, K. J.; Budd, P. M.; Tattershall, C. E.; Mahmood, K.; Tan, S.; Book, D.; Langmi, H. W.; Walton, A., Towards Polymer-Based Hydrogen Storage Materials: Engineering Ultramicroporous Cavities within Polymers of Intrinsic Microporosity. *Angewandte Chemie International Edition* **2006,** *45* (11), 1804-1807.

80. Ben, T.; Ren, H.; Ma, S.; Cao, D.; Lan, J.; Jing, X.; Wang, W.; Xu, J.; Deng, F.; Simmons, J. M.; Qiu, S.; Zhu, G., Targeted Synthesis of a Porous Aromatic Framework with High Stability and Exceptionally High Surface Area. *Angewandte Chemie International Edition* **2009,** *48* (50), 9457-9460.

81. Lu, W.; Yuan, D.; Sculley, J.; Zhao, D.; Krishna, R.; Zhou, H.-C., Sulfonate-Grafted Porous Polymer Networks for Preferential CO2 Adsorption at Low Pressure. *Journal of the American Chemical Society* **2011,** *133* (45), 18126-18129.

82. Lu, W.; Sculley, J. P.; Yuan, D.; Krishna, R.; Wei, Z.; Zhou, H.-C., Polyamine-Tethered Porous Polymer Networks for Carbon Dioxide Capture from Flue Gas. *Angewandte Chemie International Edition* **2012,** *51* (30), 7480-7484.

83. Huang, N.; Day, G.; Yang, X.; Drake, H.; Zhou, H.-C., Engineering porous organic polymers for carbon dioxide capture. *Science China Chemistry* **2017,** *60* (8), 1007-1014.

84. Lu, W.; Bosch, M.; Yuan, D.; Zhou, H.-C., Cost-Effective Synthesis of Amine-Tethered Porous Materials for Carbon Capture. *ChemSusChem* **2015,** *8* (3), 433-438.

85. Lu, W.; Sculley, J. P.; Yuan, D.; Krishna, R.; Zhou, H.-C., Carbon Dioxide Capture from Air Using Amine-Grafted Porous Polymer Networks. *The Journal of Physical Chemistry C* **2013,** *117* (8), 4057-4061.

86. Cohen, S. M., Postsynthetic Methods for the Functionalization of Metal–Organic Frameworks. *Chemical Reviews* **2012,** *112* (2), 970-1000.

87. Ratvijitvech, T.; Dawson, R.; Laybourn, A.; Khimyak, Y. Z.; Adams, D. J.; Cooper, A. I., Post-synthetic modification of conjugated microporous polymers. *Polymer* **2014,** *55* (1), 321-325.

88. Day, G. S.; Drake, H. F.; Joseph, E. A.; Bosch, M.; Tan, K.; Willman, J. A.; Carretier, V.; Perry, Z.; Burtner, W.; Banerjee, S.; Ozdemir, O. K.; Zhou, H. C., Improving Alkylamine Incorporation in Porous Polymer Networks through Dopant Incorporation. *Advanced Sustainable Systems* **2019,** *3* (12), 1900051.

89. Dantas, S.; Struckhoff, K. C.; Thommes, M.; Neimark, A. V., Phase Behavior and Capillary Condensation Hysteresis of Carbon Dioxide in Mesopores. *Langmuir* **2019,** *35* (35), 11291-11298.

90. Li, H.; Wang, K.; Sun, Y.; Lollar, C. T.; Li, J.; Zhou, H.-C., Recent advances in gas storage and separation using metal–organic frameworks. *Materials Today* **2018,** *21* (2), 108-121.

91. Feng, L.; Wang, Y.; Yuan, S.; Wang, K.-Y.; Li, J.-L.; Day, G. S.; Qiu, D.; Cheng, L.; Chen, W.-M.; Madrahimov, S. T.; Zhou, H.-C., Porphyrinic Metal–Organic Frameworks Installed with Brønsted Acid Sites for Efficient Tandem Semisynthesis of Artemisinin. *ACS Catalysis* **2019,** *9* (6), 5111-5118.

92. Keskin, S.; Kızılel, S., Biomedical Applications of Metal Organic Frameworks. *Industrial & Engineering Chemistry Research* **2011,** *50* (4), 1799-1812.

93. Kauffman, G. B., Coordination Chemistry: History. *Encyclopedia of Inorganic and Bioinorganic Chemistry* **2011**.

94. Buser, H. J.; Schwarzenbach, D.; Petter, W.; Ludi, A., The crystal structure of Prussian Blue: Fe4[Fe(CN)6]3.xH2O. *Inorganic Chemistry* **1977,** *16* (11), 2704-2710.

95. Werner, A., Contribution to the Constitution of Inorganic Compounds,'. *Z Anorg Allg Chem* **1893,** *3*, 267.

96. Constable, E. C.; Housecroft, C. E., Coordination chemistry: the scientific legacy of Alfred Werner. *Chemical Society Reviews* **2013,** *42* (4), 1429-1439.

97. Chernyaev, I. y. I. i., Mononitrates of Divalent Platinum. *Izvestiia Intituta po izucheniiu planiny* **1926,** *4*, 243.

98. Kauffman, G. B., Il'ya Il'ich Chernyaev (1893-1966) and the trans effect. *Journal of Chemical Education* **1977,** *54* (2), 86.

99. Coe, B. J.; Glenwright, S. J., Trans-effects in octahedral transition metal complexes. *Coordination Chemistry Reviews* **2000,** *203* (1), 5-80.

100. Pearson, R. G., Hard and Soft Acids and Bases. *Journal of the American Chemical Society* **1963,** *85* (22), 3533-3539.

101. Lewis, G. N., *Valence and the Structure of Atoms and Molecules*. Chemical Catalog Company, Incorporated: 1923.

102. Labinger, J. A., *Up from Generality: How Inorganic Chemistry Finally Became a Respectable Field*. Springer: 2013.

103. Wilkinson, G. The Nobel Prize in Chemistry 1973. https://www.nobelprize.org/prizes/chemistry/1973/wilkinson/lecture/.

104. Bailar Jr, J. C.; Martin, K.; Judd, M. L.; McLean, J. *Polymerization Through Coordination*; ILLINOIS UNIV AT URBANA DEPT OF CHEMISTRY AND CHEMICAL ENGINEERING: 1958.

105. Kauffman, G. B.; Girolami, G. S.; Busch, D. H., John C. Bailar, Jr. (1904–1991): father of coordination chemistry in the United States. *Coordination Chemistry Reviews* **1993,** *128* (1), 1-48.

106. Goodwin, H. A.; Bailar, J. C., Coördination Compounds Derived from Polymeric Schiff's Bases1. *Journal of the American Chemical Society* **1961,** *83* (11), 2467-2471.

107. Klein, R. M.; Bailar, J. C., Reactions of Coordination Compounds. Polymers from 3-Substituted Bis-(β-diketone)-beryllium Complexes. *Inorganic Chemistry* **1963,** *2* (6), 1190-1194.

108. Oh, J. S.; Bailar, J. C., Some co-ordination polymers prepared from bis-(β-diketones). *Journal of Inorganic and Nuclear Chemistry* **1962,** *24* (10), 1225-1234.

109. Leong, W. L.; Vittal, J. J., One-Dimensional Coordination Polymers: Complexity and Diversity in Structures, Properties, and Applications. *Chemical Reviews* **2011,** *111* (2), 688-764.

110. Li, C.-H.; Zuo, J.-L., Self-Healing Polymers Based on Coordination Bonds. *Advanced Materials* **2019,** *n/a* (n/a), 1903762.

111. Batten Stuart, R.; Champness Neil, R.; Chen, X.-M.; Garcia-Martinez, J.; Kitagawa, S.; Öhrström, L.; O'Keeffe, M.; Paik Suh, M.; Reedijk, J., Terminology of metal–organic frameworks and coordination polymers (IUPAC Recommendations 2013). In *Pure and Applied Chemistry*, 2013; Vol. 85, p 1715.

112. Robson, R.; Abrahams, B. F.; Batten, S. R.; Gable, R. W.; Hoskins, B. F.; Liu, J., Crystal Engineering of Novel Materials Composed of Infinite Two- and Three-Dimensional Frameworks. In *Supramolecular Architecture*, American Chemical Society: 1992; Vol. 499, pp 256-273.

113. Fujita, M.; Kwon, Y. J.; Washizu, S.; Ogura, K., Preparation, Clathration Ability, and Catalysis of a Two-Dimensional Square Network Material Composed of Cadmium(II) and 4,4'-Bipyridine. *Journal of the American Chemical Society* **1994,** *116* (3), 1151-1152.

114. Holland, D., The Man Who Built a Whole New Field of Chemistry. *Pursuit* 2019/10/15, https://pursuit.unimelb.edu.au/articles/the-man-who-built-a-whole-new-field-of-chemistry.

115. Zheng, C.; Greer, H. F.; Chiang, C.-Y.; Zhou, W., Microstructural study of the formation mechanism of metal–organic framework MOF-5. *CrystEngComm* **2014,** *16* (6), 1064-1070.

116. Lee, Y.-R.; Kim, J.; Ahn, W.-S., Synthesis of metal-organic frameworks: A mini review. *Korean Journal of Chemical Engineering* **2013,** *30* (9), 1667-1680.

117. Smith, J. V., Topochemistry of zeolites and related materials. 1. Topology and geometry. *Chemical Reviews* **1988,** *88* (1), 149-182.

118. O'Keeffe, M.; Peskov, M. A.; Ramsden, S. J.; Yaghi, O. M., The Reticular Chemistry Structure Resource (RCSR) Database of, and Symbols for, Crystal Nets. *Accounts of Chemical Research* **2008,** *41* (12), 1782-1789.

119. Gupta, S.; Saxena, A., A topological twist on materials science. *MRS Bulletin* **2014,** *39* (3), 265-279.

120. Contant, R.; Klemperer, W. G.; Yaghi, O., Potassium Octadecatungstodiphosphates(V) and Related Lacunary Compounds. *Inorganic Syntheses* **1990**, 104-111.

121. Klemperer, W. G.; Marquart, T. A.; Yaghi, O. M., New Directions in Polyvanadate Chemistry: From Cages and Clusters to Baskets, Belts, Bowls, and Barrels. *Angewandte Chemie International Edition in English* **1992,** *31* (1), 49-51.

122. Park, K. S.; Ni, Z.; Côté, A. P.; Choi, J. Y.; Huang, R.; Uribe-Romo, F. J.; Chae, H. K.; O'Keeffe, M.; Yaghi, O. M., Exceptional chemical and thermal stability of zeolitic imidazolate frameworks. *Proceedings of the National Academy of Sciences* **2006,** *103* (27), 10186.

123. Yaghi, O. M.; Li, H., Hydrothermal Synthesis of a Metal-Organic Framework Containing Large Rectangular Channels. *Journal of the American Chemical Society* **1995,** *117* (41), 10401-10402.

124. Masuda, H.; Machida, K.; Munakata, M.; Kitagawa, S.; Shimono, H., Synthesis and structural study of (2,2′-bipyridine)perchlorato(styrene)-copper(I). *Journal of the Chemical Society, Dalton Transactions* **1988,** (7), 1907-1910.

125. Kondo, M.; Yoshitomi, T.; Matsuzaka, H.; Kitagawa, S.; Seki, K., Three-Dimensional Framework with Channeling Cavities for Small Molecules: {[M2(4, 4′-bpy)3(NO3)4]·xH2O}n (M □ Co, Ni, Zn). *Angewandte Chemie International Edition in English* **1997,** *36* (16), 1725-1727.

126. Hoskins, B. F.; Robson, R., Design and construction of a new class of scaffolding-like materials comprising infinite polymeric frameworks of 3D-linked molecular rods. A reappraisal of the zinc cyanide and cadmium cyanide structures and the synthesis and structure of the diamond-related frameworks [N(CH3)4][CuIZnII(CN)4] and CuI[4,4',4",4"'-tetracyanotetraphenylmethane]BF4.xC6H5NO2. *Journal of the American Chemical Society* **1990,** *112* (4), 1546-1554.

127. Kitagawa, S.; Matsuyama, S.; Munakata, M.; Emori, T., Synthesis and crystal structures of novel one-dimensional polymers, [{M(bpen)X}∞][M = Cu, X = PF6–; M = Ag, X = ClO4–; bpen =trans-1,2-bis(2-pyridyl)ethylene] and [{Cu(bpen)(CO)(CH3CN)(PF6)}∞]. *Journal of the Chemical Society, Dalton Transactions* **1991,** (11), 2869-2874.

128. Munakata, M.; Kuroda-Sowa, T.; Maekawa, M.; Honda, A.; Kitagawa, S., Building a two-dimensional co-ordination polymer having a multilayered arrangement. A molecular assembly comprising hanging phenazine molecules between polymeric stair frameworks of copper(I) halides. *Journal of the Chemical Society, Dalton Transactions* **1994,** (19), 2771-2775.

129. Kitagawa, S.; Kondo, M., Functional Micropore Chemistry of Crystalline Metal Complex-Assembled Compounds. *Bulletin of the Chemical Society of Japan* **1998,** *71* (8), 1739-1753.

130. Yaghi, O. M.; Li, H.; Davis, C.; Richardson, D.; Groy, T. L., Synthetic Strategies, Structure Patterns, and Emerging Properties in the Chemistry of Modular Porous Solids. *Accounts of Chemical Research* **1998,** *31* (8), 474-484.

131. Li, H.; Eddaoudi, M.; O'Keeffe, M.; Yaghi, O. M., Design and synthesis of an exceptionally stable and highly porous metal-organic framework. *Nature* **1999,** *402* (6759), 276-279.

132. Eddaoudi, M.; Kim, J.; Rosi, N.; Vodak, D.; Wachter, J.; Keeffe, M.; Yaghi, O. M., Systematic Design of Pore Size and Functionality in Isoreticular MOFs and Their Application in Methane Storage. *Science* **2002,** *295* (5554), 469.

133. Férey, G.; Mellot-Draznieks, C.; Serre, C.; Millange, F.; Dutour, J.; Surblé, S.; Margiolaki, I., A Chromium Terephthalate-Based Solid with Unusually Large Pore Volumes and Surface Area. *Science* **2005,** *309* (5743), 2040.

134. Loiseau, T.; Serre, C.; Huguenard, C.; Fink, G.; Taulelle, F.; Henry, M.; Bataille, T.; Férey, G., A Rationale for the Large Breathing of the Porous Aluminum Terephthalate (MIL-53) Upon Hydration. *Chemistry – A European Journal* **2004,** *10* (6), 1373-1382.

135. Yuan, S.; Qin, J.-S.; Lollar, C. T.; Zhou, H.-C., Stable Metal–Organic Frameworks with Group 4 Metals: Current Status and Trends. *ACS Central Science* **2018,** *4* (4), 440-450.

136. Zhang, J.-P.; Zhang, Y.-B.; Lin, J.-B.; Chen, X.-M., Metal Azolate Frameworks: From Crystal Engineering to Functional Materials. *Chemical Reviews* **2012,** *112* (2), 1001-1033.

137. Zhang, J.-P.; Lin, Y.-Y.; Huang, X.-C.; Chen, X.-M., Copper(I) 1,2,4-Triazolates and Related Complexes: Studies of the Solvothermal Ligand Reactions, Network Topologies, and Photoluminescence Properties. *Journal of the American Chemical Society* **2005,** *127* (15), 5495-5506.

138. Tian, Y.-Q.; Cai, C.-X.; Ren, X.-M.; Duan, C.-Y.; Xu, Y.; Gao, S.; You, X.-Z., The Silica-Like Extended Polymorphism of Cobalt(II) Imidazolate Three-Dimensional Frameworks: X-ray Single-Crystal Structures and Magnetic Properties. *Chemistry – A European Journal* **2003,** *9* (22), 5673-5685.

139. Chen, B.; Yang, Z.; Zhu, Y.; Xia, Y., Zeolitic imidazolate framework materials: recent progress in synthesis and applications. *Journal of Materials Chemistry A* **2014,** *2* (40), 16811-16831.

140. Rosi, N. L.; Eckert, J.; Eddaoudi, M.; Vodak, D. T.; Kim, J.; Keeffe, M.; Yaghi, O. M., Hydrogen Storage in Microporous Metal-Organic Frameworks. *Science* **2003,** *300* (5622), 1127.

141. Beckner, M.; Dailly, A., Adsorbed methane storage for vehicular applications. *Applied Energy* **2015,** *149*, 69-74.

142. Peng, Y.; Krungleviciute, V.; Eryazici, I.; Hupp, J. T.; Farha, O. K.; Yildirim, T., Methane Storage in Metal–Organic Frameworks: Current Records, Surprise Findings, and Challenges. *Journal of the American Chemical Society* **2013,** *135* (32), 11887-11894.

143. Gómez-Gualdrón, D. A.; Wilmer, C. E.; Farha, O. K.; Hupp, J. T.; Snurr, R. Q., Exploring the Limits of Methane Storage and Delivery in Nanoporous Materials. *The Journal of Physical Chemistry C* **2014,** *118* (13), 6941-6951.

144. Wu, H.; Zhou, W.; Yildirim, T., High-Capacity Methane Storage in Metal−Organic Frameworks M2(dhtp): The Important Role of Open Metal Sites. *Journal of the American Chemical Society* **2009,** *131* (13), 4995-5000.

145. Vitillo, J. G.; Regli, L.; Chavan, S.; Ricchiardi, G.; Spoto, G.; Dietzel, P. D. C.; Bordiga, S.; Zecchina, A., Role of Exposed Metal Sites in Hydrogen Storage in MOFs. *Journal of the American Chemical Society* **2008,** *130* (26), 8386-8396.

146. Yang, Q.-Y.; Lama, P.; Sen, S.; Lusi, M.; Chen, K.-J.; Gao, W.-Y.; Shivanna, M.; Pham, T.; Hosono, N.; Kusaka, S.; Perry Iv, J. J.; Ma, S.; Space, B.; Barbour, L. J.; Kitagawa, S.; Zaworotko, M. J., Reversible Switching between Highly Porous and Nonporous Phases of an Interpenetrated Diamondoid Coordination Network That Exhibits

Gate-Opening at Methane Storage Pressures. *Angewandte Chemie International Edition* **2018,** *57* (20), 5684-5689.

147. Yilmaz, B.; Trukhan, N.; MÜLler, U., Industrial Outlook on Zeolites and Metal Organic Frameworks. *Chinese Journal of Catalysis* **2012,** *33* (1), 3-10.

148. McMahon, M. M. NuMat Brings First MOF-Enabled Gas Storage Product to Market | Institute for Sustainability and Energy at Northwestern (ISEN) 2017. https://isen.northwestern.edu/numat-brings-first-mof-enabled-gas-storage-product-to-market.

149. Hu, Z.; Zhao, D., Metal–organic frameworks with Lewis acidity: synthesis, characterization, and catalytic applications. *CrystEngComm* **2017,** *19* (29), 4066-4081.

150. Schlichte, K.; Kratzke, T.; Kaskel, S., Improved synthesis, thermal stability and catalytic properties of the metal-organic framework compound Cu3(BTC)2. *Microporous and Mesoporous Materials* **2004,** *73* (1), 81-88.

151. Seo, J. S.; Whang, D.; Lee, H.; Jun, S. I.; Oh, J.; Jeon, Y. J.; Kim, K., A homochiral metal–organic porous material for enantioselective separation and catalysis. *Nature* **2000,** *404* (6781), 982-986.

152. Wang, Z.; Cohen, S. M., Postsynthetic modification of metal–organic frameworks. *Chemical Society Reviews* **2009,** *38* (5), 1315-1329.

153. Wang, Z.; Cohen, S. M., Postsynthetic Covalent Modification of a Neutral Metal−Organic Framework. *Journal of the American Chemical Society* **2007,** *129* (41), 12368-12369.

154. Oh, M.; Mirkin, C. A., Ion Exchange as a Way of Controlling the Chemical Compositions of Nano- and Microparticles Made from Infinite Coordination Polymers. *Angewandte Chemie International Edition* **2006,** *45* (33), 5492-5494.

155. Hwang, Y. K.; Hong, D.-Y.; Chang, J.-S.; Jhung, S. H.; Seo, Y.-K.; Kim, J.; Vimont, A.; Daturi, M.; Serre, C.; Férey, G., Amine Grafting on Coordinatively Unsaturated Metal Centers of MOFs: Consequences for Catalysis and Metal Encapsulation. *Angewandte Chemie International Edition* **2008,** *47* (22), 4144-4148.

156. Ingleson, M. J.; Perez Barrio, J.; Guilbaud, J.-B.; Khimyak, Y. Z.; Rosseinsky, M. J., Framework functionalisation triggers metal complex binding. *Chemical Communications* **2008,** (23), 2680-2682.

157. Lee, J.; Farha, O. K.; Roberts, J.; Scheidt, K. A.; Nguyen, S. T.; Hupp, J. T., Metal–organic framework materials as catalysts. *Chemical Society Reviews* **2009,** *38* (5), 1450-1459.

158. Chui, S. S.; Lo, S. M.; Charmant, J. P.; Orpen, A. G.; Williams, I. D., A chemically functionalizable nanoporous material. *Science* **1999,** *283* (5405), 1148-50.

159. Férey, G.; Serre, C.; Mellot-Draznieks, C.; Millange, F.; Surblé, S.; Dutour, J.; Margiolaki, I., A Hybrid Solid with Giant Pores Prepared by a Combination of Targeted Chemistry, Simulation, and Powder Diffraction. *Angewandte Chemie International Edition* **2004,** *43* (46), 6296-6301.

160. Cavka, J. H.; Jakobsen, S.; Olsbye, U.; Guillou, N.; Lamberti, C.; Bordiga, S.; Lillerud, K. P., A New Zirconium Inorganic Building Brick Forming Metal Organic

Frameworks with Exceptional Stability. *Journal of the American Chemical Society* **2008,** *130* (42), 13850-13851.

161. Elmas Kimyonok, A. B.; Ulutürk, M., Determination of the Thermal Decomposition Products of Terephthalic Acid by Using Curie-Point Pyrolyzer. *Journal of Energetic Materials* **2016,** *34* (2), 113-122.

162. Lucchesi, C. A.; Lewis, W. T., Latent heat of sublimation of terephthalic acid from differential thermal analysis data. *Journal of Chemical & Engineering Data* **1968,** *13* (3), 389-391.

163. Mcmakin, J. L. E.; Bryant, J. H. S., Method for fractional sublimation. Google Patents: 1968.

164. Millange, F.; Serre, C.; Férey, G., Synthesis, structure determination and properties of MIL-53as and MIL-53ht: the first Criii hybrid inorganic–organic microporous solids: Criii(OH)·{O2C–C6H4–CO2}·{HO2C–C6H4–CO2H}x. *Chemical Communications* **2002,** (8), 822-823.

165. Patil, D. V.; Rallapalli, P. B. S.; Dangi, G. P.; Tayade, R. J.; Somani, R. S.; Bajaj, H. C., MIL-53(Al): An Efficient Adsorbent for the Removal of Nitrobenzene from Aqueous Solutions. *Industrial & Engineering Chemistry Research* **2011,** *50* (18), 10516-10524.

166. Taylor-Pashow, K. M. L.; Della Rocca, J.; Xie, Z.; Tran, S.; Lin, W., Postsynthetic Modifications of Iron-Carboxylate Nanoscale Metal−Organic Frameworks for Imaging and Drug Delivery. *Journal of the American Chemical Society* **2009,** *131* (40), 14261-14263.

167. Pérez, N.; López-Calahorra, F.; Labarta, A.; Batlle, X., Reduction of iron by decarboxylation in the formation of magnetite nanoparticles. *Physical Chemistry Chemical Physics* **2011,** *13* (43), 19485-19489.

168. Vrubel, H.; Hasegawa, T.; Oliveira, E. d.; Nunes, F. S., A new facile high yield preparative route for mixed-trinuclear acetate clusters. *Inorganic Chemistry Communications* **2006,** *9* (2), 208-211.

169. Drake, H. F.; Day, G. S.; Vali, S. W.; Xiao, Z.; Banerjee, S.; Li, J.; Joseph, E. A.; Kuszynski, J. E.; Perry, Z. T.; Kirchon, A.; Ozdemir, O. K.; Lindahl, P. A.; Zhou, H.-C., The thermally induced decarboxylation mechanism of a mixed-oxidation state carboxylate-based iron metal–organic framework. *Chemical Communications* **2019,** *55* (85), 12769-12772.

170. Maton, C.; De Vos, N.; Stevens, C. V., Ionic liquid thermal stabilities: decomposition mechanisms and analysis tools. *Chemical Society Reviews* **2013,** *42* (13), 5963-5977.

171. Ranninger, M. C. N.; Andrade, M. G.; Franco, M. A. A., Thermal decomposition of some imidazole and N-methyl substituted imidazole complexes of palladium(II). *Journal of thermal analysis* **1978,** *14* (3), 281-290.

172. Gomm, P. S.; Underhill, A. E.; Oliver, R. W. A., Thermal decomposition of imidazole complexes of the type MIm6X2 (where M = Co or Ni; X = Cl, Br, or I; Im = C3H4N2 and M = Co; X = NO3). *Journal of Inorganic and Nuclear Chemistry* **1972,** *34* (6), 1879-1883.

173. Zohari, N.; Abrishami, F.; Zeynali, V., Prediction of decomposition temperature of azole-based energetic compounds in order to assess of their thermal stability. *Journal of Thermal Analysis and Calorimetry* **2019**.

174. Zhang, S.; Yang, Q.; Liu, X.; Qu, X.; Wei, Q.; Xie, G.; Chen, S.; Gao, S., High-energy metal–organic frameworks (HE-MOFs): Synthesis, structure and energetic performance. *Coordination Chemistry Reviews* **2016,** *307*, 292-312.

175. Qu, X.-N.; Zhang, S.; Wang, B.-Z.; Yang, Q.; Han, J.; Wei, Q.; Xie, G.; Chen, S.-P., An Ag(i) energetic metal–organic framework assembled with the energetic combination of furazan and tetrazole: synthesis, structure and energetic performance. *Dalton Transactions* **2016,** *45* (16), 6968-6973.

176. Pan, Y.; Liu, Y.; Zeng, G.; Zhao, L.; Lai, Z., Rapid synthesis of zeolitic imidazolate framework-8 (ZIF-8) nanocrystals in an aqueous system. *Chemical Communications* **2011,** *47* (7), 2071-2073.

177. James, J. B.; Lin, Y. S., Kinetics of ZIF-8 Thermal Decomposition in Inert, Oxidizing, and Reducing Environments. *The Journal of Physical Chemistry C* **2016,** *120* (26), 14015-14026.

178. Salunkhe, R. R.; Kaneti, Y. V.; Yamauchi, Y., Metal–Organic Framework-Derived Nanoporous Metal Oxides toward Supercapacitor Applications: Progress and Prospects. *ACS Nano* **2017,** *11* (6), 5293-5308.

179. Wang, Y.; Lü, Y.; Zhan, W.; Xie, Z.; Kuang, Q.; Zheng, L., Synthesis of porous Cu2O/CuO cages using Cu-based metal–organic frameworks as templates and their gas-sensing properties. *Journal of Materials Chemistry A* **2015,** *3* (24), 12796-12803.

180. Yang, P.; Zhang, Z.-W.; Zou, G.-D.; Huang, Y.; Li, N.; Fan, Y., Template Thermolysis to Create a Carbon Dots-Embedded Mesoporous Titanium-Oxo Sulfate Framework for Visible-Light Photocatalytic Applications. *Inorganic Chemistry* **2020,** *59* (3), 2062-2069.

181. Lu, N.; Zhang, X.; Yan, X.; Pan, D.; Fan, B.; Li, R., Synthesis of novel mesoporous sulfated zirconia nanosheets derived from Zr-based metal–organic frameworks. *CrystEngComm* **2020,** *22* (1), 44-51.

182. Liu, B.; Shioyama, H.; Akita, T.; Xu, Q., Metal-Organic Framework as a Template for Porous Carbon Synthesis. *Journal of the American Chemical Society* **2008,** *130* (16), 5390-5391.

183. Liu, B.; Shioyama, H.; Jiang, H.; Zhang, X.; Xu, Q., Metal–organic framework (MOF) as a template for syntheses of nanoporous carbons as electrode materials for supercapacitor. *Carbon* **2010,** *48* (2), 456-463.

184. Day, G. S.; Li, J.; Joseph, E.; Metz, P. C.; Perry, Z.; Ryder, M. R.; Page, K.; Zhou, H.-C., Metal Oxide Decorated Porous Carbons from Controlled Calcination of a Metal-Organic Framework. *Nanoscale Advances* **2020**.

185. Liu, C.; Huang, X.; Wang, J.; Song, H.; Yang, Y.; Liu, Y.; Li, J.; Wang, L.; Yu, C., Hollow Mesoporous Carbon Nanocubes: Rigid-Interface-Induced Outward Contraction of Metal-Organic Frameworks. *Advanced Functional Materials* **2018,** *28* (6), 1705253.

186. Yang, S. J.; Kim, T.; Im, J. H.; Kim, Y. S.; Lee, K.; Jung, H.; Park, C. R., MOF-Derived Hierarchically Porous Carbon with Exceptional Porosity and Hydrogen Storage Capacity. *Chemistry of Materials* **2012,** *24* (3), 464-470.

187. Wu, C.; Xie, D.; Mei, Y.; Xiu, Z.; Poduska, K. M.; Li, D.; Xu, B.; Sun, D., Unveiling the thermolysis natures of ZIF-8 and ZIF-67 by employing in situ structural characterization studies. *Physical Chemistry Chemical Physics* **2019,** *21* (32), 17571-17577.

188. Panda, R.; Rahut, S.; Basu, J. K., Preparation of a Fe2O3/MIL-53(Fe) composite by partial thermal decomposition of MIL-53(Fe) nanorods and their photocatalytic activity. *RSC Advances* **2016,** *6* (84), 80981-80985.

189. Shen, K.; Chen, X.; Chen, J.; Li, Y., Development of MOF-Derived Carbon-Based Nanomaterials for Efficient Catalysis. *ACS Catalysis* **2016,** *6* (9), 5887-5903.

190. Han, A.; Wang, B.; Kumar, A.; Qin, Y.; Jin, J.; Wang, X.; Yang, C.; Dong, B.; Jia, Y.; Liu, J.; Sun, X., Recent Advances for MOF-Derived Carbon-Supported Single-Atom Catalysts. *Small Methods* **2019,** *3* (9), 1800471.

191. Ji, S.; Chen, Y.; Fu, Q.; Chen, Y.; Dong, J.; Chen, W.; Li, Z.; Wang, Y.; Gu, L.; He, W.; Chen, C.; Peng, Q.; Huang, Y.; Duan, X.; Wang, D.; Draxl, C.; Li, Y., Confined Pyrolysis within Metal–Organic Frameworks To Form Uniform Ru3 Clusters for Efficient Oxidation of Alcohols. *Journal of the American Chemical Society* **2017,** *139* (29), 9795-9798.

192. Deng, Y.; Chi, B.; Li, J.; Wang, G.; Zheng, L.; Shi, X.; Cui, Z.; Du, L.; Liao, S.; Zang, K.; Luo, J.; Hu, Y.; Sun, X., Atomic Fe-Doped MOF-Derived Carbon Polyhedrons

with High Active-Center Density and Ultra-High Performance toward PEM Fuel Cells. *Advanced Energy Materials* **2019,** *9* (13), 1802856.

193. Gregory S., D.; Jialuo, L.; Elizabeth A., J.; Peter, M.; Zachary, P.; Matthew R., R.; Katharine, P.; Hong-Cai, Z., *Metal Oxide Decorated Porous Carbons from Controlled Calcination of a Metal-Organic Framework*. 2019.

194. Everett, D. H., Manual of Symbols and Terminology for Physicochemical Quantities and Units, Appendix II: Definitions, Terminology and Symbols in Colloid and Surface Chemistry. *Pure and Applied Chemistry* **1972,** *31* (4), 577-638.

195. Rouquerol, J.; Avnir, D.; Fairbridge, C. W.; Everett, D. H.; Haynes, J. M.; Pernicone, N.; Ramsay, J. D. F.; Sing, K. S. W.; Unger, K. K., Recommendations for the characterization of porous solids (Technical Report). *Pure and Applied Chemistry* **1994,** *66* (8), 1739-1758.

196. Webb, P., An Introduction To The Physical Characterization of Materials by Mercury Intrusion Porosimetry with Emphasis On Reduction And Presentation of Experimental Data 2 CONTENTS. *Pharm Online* **2001**.

197. Calvert, J. G., Glossary of atmospheric chemistry terms (Recommendations 1990). *Pure and Applied Chemistry* **1990,** *62* (11), 2167-2219.

198. Sing, K. S. W., Characterization of porous materials: past, present and future. *Colloids and Surfaces A: Physicochemical and Engineering Aspects* **2004,** *241* (1), 3-7.

199. Langmuir, I., THE CONSTITUTION AND FUNDAMENTAL PROPERTIES OF SOLIDS AND LIQUIDS. PART I. SOLIDS. *Journal of the American Chemical Society* **1916,** *38* (11), 2221-2295.

200. Langmuir, I., THE CONSTITUTION AND FUNDAMENTAL PROPERTIES OF SOLIDS AND LIQUIDS. II. LIQUIDS.1. *Journal of the American Chemical Society* **1917,** *39* (9), 1848-1906.

201. Langmuir, I., THE ADSORPTION OF GASES ON PLANE SURFACES OF GLASS, MICA AND PLATINUM. *Journal of the American Chemical Society* **1918,** *40* (9), 1361-1403.

202. Kayser, H., Ueber die Verdichtung von Gasen an Oberflächen in ihrer Abhängigkeit von Druck und Temperatur. *Annalen der Physik* **1881,** *250* (11), 450-468.

203. Swenson, H.; Stadie, N. P., Langmuir's Theory of Adsorption: A Centennial Review. *Langmuir* **2019,** *35* (16), 5409-5426.

204. Hu, Z.; Wang, Y.; Shah, B. B.; Zhao, D., CO2 Capture in Metal–Organic Framework Adsorbents: An Engineering Perspective. *Advanced Sustainable Systems* **2019,** *3* (1), 1800080.

205. Brunauer, S.; Emmett, P. H.; Teller, E., Adsorption of Gases in Multimolecular Layers. *Journal of the American Chemical Society* **1938,** *60* (2), 309-319.

206. Sing, K. S. W., Reporting physisorption data for gas/solid systems with special reference to the determination of surface area and porosity (Recommendations 1984). *Pure and Applied Chemistry* **1985,** *57* (4), 603-619.

207. Matthias, T.; Katsumi, K.; Alexander, V. N.; James, P. O.; Francisco, R.-R.; Jean, R.; Kenneth, S. W. S., Physisorption of gases, with special reference to the evaluation of surface area and pore size distribution (IUPAC Technical Report). *Pure and Applied Chemistry* **2015,** *87* (9-10), 1051-1069.

208. Rietveld, H., A profile refinement method for nuclear and magnetic structures. *Journal of Applied Crystallography* **1969,** *2* (2), 65-71.

209. McCusker, L. B.; Von Dreele, R. B.; Cox, D. E.; Louer, D.; Scardi, P., Rietveld refinement guidelines. *Journal of Applied Crystallography* **1999,** *32* (1), 36-50.

210. Scherrer, P., Bestimmung der Größe und der inneren Struktur von Kolloidteilchen mittels Röntgenstrahlen. *Nachrichten von der Gesellschaft der Wissenschaften zu Göttingen, Mathematisch-Physikalische Klasse* **1918,** *2*, 98-100.

211. Patterson, A. L., The Scherrer Formula for X-Ray Particle Size Determination. *Physical Review* **1939,** *56* (10), 978-982.

212. Billinge, S. J. L.; Kanatzidis, M. G., Beyond crystallography: the study of disorder, nanocrystallinity and crystallographically challenged materials with pair distribution functions. *Chemical Communications* **2004,** (7), 749-760.

213. Egami, T.; Billinge, S. J., *Underneath the Bragg peaks: structural analysis of complex materials*. Elsevier: 2003.

214. Billinge Simon, J. L., The atomic pair distribution function: past and present. In *Zeitschrift für Kristallographie - Crystalline Materials*, 2004; Vol. 219, p 117.

215. Billinge, S. J. L., The rise of the X-ray atomic pair distribution function method: a series of fortunate events. *Philosophical Transactions of the Royal Society A: Mathematical, Physical and Engineering Sciences* **2019,** *377* (2147), 20180413.

216. Toby, B. H.; Egami, T., Accuracy of pair distribution function analysis applied to crystalline and non-crystalline materials. *Acta Crystallographica Section A* **1992,** *48* (3), 336-346.

217. Bauer, G. S., Physics and technology of spallation neutron sources. *Nuclear Instruments and Methods in Physics Research Section A: Accelerators, Spectrometers, Detectors and Associated Equipment* **2001,** *463* (3), 505-543.

218. Bilderback, D. H.; Elleaume, P.; Weckert, E., Review of third and next generation synchrotron light sources. *Journal of Physics B: Atomic, Molecular and Optical Physics* **2005,** *38* (9), S773-S797.

219. Pynn, R., *Neutron Scattering, A Primer*. Los Alamo Science: 1990.

220. Litvin, D., Tables of crystallographic properties of magnetic space groups. *Acta Crystallographica Section A* **2008,** *64* (3), 419-424.

221. Neutron Scattering Methods in Chemistry. In *Handbook of Nuclear Chemistry: Basics of Nuclear Science; Elements and Isotopes: Formation, Transformation, Distribution; Chemical Applications of Nuclear Reactions and Radiations; Radiochemistry and Radiopharmaceutical Chemistry in Life Sciences; Instrumentation, Separation Techniques, Environmental Issues*, Springer US: Boston, MA, 2004; pp 1084-1124.

222. Russell, R. A.; Garvey, C. J.; Darwish, T. A.; Foster, L. J. R.; Holden, P. J., Chapter Five - Biopolymer Deuteration for Neutron Scattering and Other Isotope-Sensitive Techniques. In *Methods in Enzymology*, Kelman, Z., Ed. Academic Press: 2015; Vol. 565, pp 97-121.

223. Diffenbaugh, N. S.; Singh, D.; Mankin, J. S.; Horton, D. E.; Swain, D. L.; Touma, D.; Charland, A.; Liu, Y.; Haugen, M.; Tsiang, M., Quantifying the influence of global

warming on unprecedented extreme climate events. *Proceedings of the National Academy of Sciences* **2017,** *114* (19), 4881-4886.

224. Woodward, A. J.; Samet, J. M., Climate Change, Hurricanes, and Health. *American Journal of Public Health* **2017,** *108* (1), 33-35.

225. Hsiang, S.; Kopp, R.; Jina, A.; Rising, J.; Delgado, M.; Mohan, S.; Rasmussen, D.; Muir-Wood, R.; Wilson, P.; Oppenheimer, M., Estimating economic damage from climate change in the United States. *Science* **2017,** *356* (6345), 1362-1369.

226. Ahn, J.; Brook Edward, J.; Mitchell, L.; Rosen, J.; McConnell Joseph, R.; Taylor, K.; Etheridge, D.; Rubino, M., Atmospheric CO2 over the last 1000 years: A high-resolution record from the West Antarctic Ice Sheet (WAIS) Divide ice core. *Global Biogeochemical Cycles* **2012,** *26* (2).

227. Friščić, T., New opportunities for materials synthesis using mechanochemistry. *Journal of Materials Chemistry* **2010,** *20* (36), 7599-7605.

228. Klimakow, M.; Klobes, P.; Thünemann, A. F.; Rademann, K.; Emmerling, F., Mechanochemical synthesis of metal− organic frameworks: a fast and facile approach toward quantitative yields and high specific surface areas. *Chemistry of Materials* **2010,** *22* (18), 5216-5221.

229. Luis, P., Use of monoethanolamine (MEA) for CO2 capture in a global scenario: Consequences and alternatives. *Desalination* **2016,** *380*, 93-99.

230. Yang, W. C.; Hoffman, J., Exploratory Design Study on Reactor Configurations for Carbon Dioxide Capture from Conventional Power Plants Employing Regenerable Solid Sorbents. *Industrial & Engineering Chemistry Research* **2009,** *48* (1), 341-351.

231. Milner, P. J.; Siegelman, R. L.; Forse, A. C.; Gonzalez, M. I.; Runčevski, T.; Martell, J. D.; Reimer, J. A.; Long, J. R., A Diaminopropane-Appended Metal–Organic Framework Enabling Efficient CO2 Capture from Coal Flue Gas via a Mixed Adsorption Mechanism. *Journal of the American Chemical Society* **2017,** *139* (38), 13541-13553.

232. Nijem, N.; Thissen, P.; Yao, Y.; Longo, R. C.; Roodenko, K.; Wu, H.; Zhao, Y.; Cho, K.; Li, J.; Langreth, D. C., Understanding the preferential adsorption of CO2 over N2 in a flexible metal–organic framework. *Journal of the American Chemical Society* **2011,** *133* (32), 12849-12857.

233. Kong, Y.; Jiang, G.; Fan, M.; Shen, X.; Cui, S.; Russell, A. G., A new aerogel based CO2 adsorbent developed using a simple sol-gel method along with supercritical drying. *Chemical Communications* **2014,** *50* (81), 12158-12161.

234. Wang, X.; Li, H.; Liu, H.; Hou, X., AS-synthesized mesoporous silica MSU-1 modified with tetraethylenepentamine for CO2 adsorption. *Microporous and Mesoporous Materials* **2011,** *142* (2), 564-569.

235. Liang, J.; Liang, Z.; Zou, R.; Zhao, Y., Heterogeneous Catalysis in Zeolites, Mesoporous Silica, and Metal–Organic Frameworks. *Advanced Materials* **2017,** *29* (30), 1701139.

236. Siriwardane, R. V.; Shen, M.-S.; Fisher, E. P.; Losch, J., Adsorption of CO2 on Zeolites at Moderate Temperatures. *Energy & Fuels* **2005,** *19* (3), 1153-1159.

237. Cui, Y.; Du, J.; Liu, Y.; Yu, Y.; Wang, S.; Pang, H.; Liang, Z.; Yu, J., Design and synthesis of a multifunctional porous N-rich polymer containing s-triazine and Troger's

base for CO2 adsorption, catalysis and sensing. *Polymer Chemistry* **2018,** *9* (19), 2643-2649.

238. Kim, I.; Svendsen, H. F., Heat of Absorption of Carbon Dioxide (CO2) in Monoethanolamine (MEA) and 2-(Aminoethyl)ethanolamine (AEEA) Solutions. *Industrial & Engineering Chemistry Research* **2007,** *46* (17), 5803-5809.

239. Li, H.; Wang, K.; Feng, D.; Chen, Y. P.; Verdegaal, W.; Zhou, H. C., Incorporation of Alkylamine into Metal–Organic Frameworks through a Brønsted Acid–Base Reaction for CO2 Capture. *ChemSusChem* **2016,** *9* (19), 2832-2840.

240. Lu, W.; Sculley, J. P.; Yuan, D.; Krishna, R.; Wei, Z.; Zhou, H. C., Polyamine-tethered porous polymer networks for carbon dioxide capture from flue gas. *Angewandte Chemie International Edition* **2012,** *51* (30), 7480-7484.

241. Quang, D. V.; Soukri, M.; Tanthana, J.; Sharma, P.; Nelson, T. O.; Lail, M.; Coleman, L. J.; Abu-Zahra, M. R., Investigation of CO2 adsorption performance and fluidization behavior of mesoporous silica supported polyethyleneimine. *Powder Technology* **2016,** *301*, 449-462.

242. Zhu, X.; Do-Thanh, C.-L.; Murdock, C. R.; Nelson, K. M.; Tian, C.; Brown, S.; Mahurin, S. M.; Jenkins, D. M.; Hu, J.; Zhao, B., Efficient CO2 capture by a 3D porous polymer derived from Tröger's base. *ACS Macro Letters* **2013,** *2* (8), 660-663.

243. Li, T.; Liang, J.; Cao, M.; Guo, X.; Xie, X.; Du, G., Re-elucidation of the acid-catalyzed urea–formaldehyde reactions: A theoretical and 13C-NMR study. *Journal of Applied Polymer Science* **2016,** *133* (48).

244. Sangeetha, V.; Kanagathara, N.; Sumathi, R.; Sivakumar, N.; Anbalagan, G., Spectral and Thermal Degradation of Melamine Cyanurate. *Journal of Materials* **2013,** *2013*, 7.

245. Banerjee, R.; Phan, A.; Wang, B.; Knobler, C.; Furukawa, H.; O'Keeffe, M.; Yaghi, O. M., High-throughput synthesis of zeolitic imidazolate frameworks and application to CO2 capture. *Science* **2008,** *319* (5865), 939-943.

246. Sayari, A.; Belmabkhout, Y., Stabilization of Amine-Containing CO2 Adsorbents: Dramatic Effect of Water Vapor. *Journal of the American Chemical Society* **2010,** *132* (18), 6312-6314.

247. Chen, B.; Ma, Q.; Tan, C.; Lim, T.-T.; Huang, L.; Zhang, H., Carbon-Based Sorbents with Three-Dimensional Architectures for Water Remediation. *Small* **2015,** *11* (27), 3319-3336.

248. Sircar, S.; Golden, T. C.; Rao, M. B., Activated carbon for gas separation and storage. *Carbon* **1996,** *34* (1), 1-12.

249. Rodríguez-reinoso, F., The role of carbon materials in heterogeneous catalysis. *Carbon* **1998,** *36* (3), 159-175.

250. Yahya, M. A.; Al-Qodah, Z.; Ngah, C. W. Z., Agricultural bio-waste materials as potential sustainable precursors used for activated carbon production: A review. *Renewable and Sustainable Energy Reviews* **2015,** *46*, 218-235.

251. Hernandez, N.; Iniesta, J.; Leguey, V. M.; Armstrong, R.; Taylor, S. H.; Madrid, E.; Rong, Y.; Castaing, R.; Malpass-Evans, R.; Carta, M.; McKeown, N. B.; Marken, F.,

Carbonization of polymers of intrinsic microporosity to microporous heterocarbon: Capacitive pH measurements. *Applied Materials Today* **2017,** *9*, 136-144.

252. Teng, H.; Chang, Y.-J.; Hsieh, C.-T., Performance of electric double-layer capacitors using carbons prepared from phenol–formaldehyde resins by KOH etching. *Carbon* **2001,** *39* (13), 1981-1987.

253. Zhong, W.; Liu, H.; Bai, C.; Liao, S.; Li, Y., Base-Free Oxidation of Alcohols to Esters at Room Temperature and Atmospheric Conditions using Nanoscale Co-Based Catalysts. *ACS Catalysis* **2015,** *5* (3), 1850-1856.

254. Santos, V. P.; Wezendonk, T. A.; Jaén, J. J. D.; Dugulan, A. I.; Nasalevich, M. A.; Islam, H.-U.; Chojecki, A.; Sartipi, S.; Sun, X.; Hakeem, A. A.; Koeken, A. C. J.; Ruitenbeek, M.; Davidian, T.; Meima, G. R.; Sankar, G.; Kapteijn, F.; Makkee, M.; Gascon, J., Metal organic framework-mediated synthesis of highly active and stable Fischer-Tropsch catalysts. *Nature Communications* **2015,** *6*, 6451.

255. Chaikittisilp, W.; Torad, N. L.; Li, C.; Imura, M.; Suzuki, N.; Ishihara, S.; Ariga, K.; Yamauchi, Y., Synthesis of Nanoporous Carbon–Cobalt-Oxide Hybrid Electrocatalysts by Thermal Conversion of Metal–Organic Frameworks. *Chemistry – A European Journal* **2014,** *20* (15), 4217-4221.

256. Veerakumar, P.; Veeramani, V.; Chen, S.-M.; Madhu, R.; Liu, S.-B., Palladium Nanoparticle Incorporated Porous Activated Carbon: Electrochemical Detection of Toxic Metal Ions. *ACS Applied Materials & Interfaces* **2016,** *8* (2), 1319-1326.

257. Pérez-Mayoral, E.; Matos, I.; Bernardo, M.; Fonseca, M. I., New and Advanced Porous Carbon Materials in Fine Chemical Synthesis. Emerging Precursors of Porous Carbons. *Catalysts* **2019,** *9* (2).

258. Zhou, H.-C.; Long, J. R.; Yaghi, O. M., Introduction to Metal–Organic Frameworks. *Chemical Reviews* **2012,** *112* (2), 673-674.

259. Ryder, M. R.; Tan, J. C., Nanoporous metal organic framework materials for smart applications. *Materials Science and Technology* **2014,** *30* (13), 1598-1612.

260. Torad, N. L.; Hu, M.; Ishihara, S.; Sukegawa, H.; Belik, A. A.; Imura, M.; Ariga, K.; Sakka, Y.; Yamauchi, Y., Direct Synthesis of MOF-Derived Nanoporous Carbon with Magnetic Co Nanoparticles toward Efficient Water Treatment. *Small* **2014,** *10* (10), 2096-2107.

261. Banerjee, A.; Gokhale, R.; Bhatnagar, S.; Jog, J.; Bhardwaj, M.; Lefez, B.; Hannoyer, B.; Ogale, S., MOF derived porous carbon–Fe3O4 nanocomposite as a high performance, recyclable environmental superadsorbent. *Journal of Materials Chemistry* **2012,** *22* (37), 19694-19699.

262. Long, J.; Shen, K.; Chen, L.; Li, Y., Multimetal-MOF-derived transition metal alloy NPs embedded in an N-doped carbon matrix: highly active catalysts for hydrogenation reactions. *Journal of Materials Chemistry A* **2016,** *4* (26), 10254-10262.

263. Khare, P.; Talreja, N.; Deva, D.; Sharma, A.; Verma, N., Carbon nanofibers containing metal-doped porous carbon beads for environmental remediation applications. *Chemical Engineering Journal* **2013,** *229*, 72-81.

264. Chinthakindi, S.; Purohit, A.; Singh, V.; Tak, V.; Goud, D. R.; Dubey, D. K.; Pardasani, D., Iron oxide functionalized graphene nano-composite for dispersive solid phase extraction of chemical warfare agents from aqueous samples. *Journal of Chromatography A* **2015,** *1394*, 9-17.

265. Bhattacharyya, S.; Konkena, B.; Jayaramulu, K.; Schuhmann, W.; Maji, T. K., Synthesis of nano-porous carbon and nitrogen doped carbon dots from an anionic MOF: a trace cobalt metal residue in carbon dots promotes electrocatalytic ORR activity. *Journal of Materials Chemistry A* **2017,** *5* (26), 13573-13580.

266. Oar-Arteta, L.; Wezendonk, T.; Sun, X.; Kapteijn, F.; Gascon, J., Metal organic frameworks as precursors for the manufacture of advanced catalytic materials. *Materials Chemistry Frontiers* **2017,** *1* (9), 1709-1745.

267. Alcañiz-Monge, J.; Lozano-Castelló, D.; Cazorla-Amorós, D.; Linares-Solano, A., Fundamentals of methane adsorption in microporous carbons. *Microporous and Mesoporous Materials* **2009,** *124* (1), 110-116.

268. Konstas, K.; Osl, T.; Yang, Y.; Batten, M.; Burke, N.; Hill, A. J.; Hill, M. R., Methane storage in metal organic frameworks. *Journal of Materials Chemistry* **2012,** *22* (33), 16698-16708.

269. Kim, H. S.; Kang, M. S.; Yoo, W. C., Highly Enhanced Gas Sorption Capacities of N-Doped Porous Carbon Spheres by Hot NH3 and CO2 Treatments. *The Journal of Physical Chemistry C* **2015,** *119* (51), 28512-28522.

270. Bhattacharyya, S.; Das, C.; Maji, T. K., MOF derived carbon based nanocomposite materials as efficient electrocatalysts for oxygen reduction and oxygen and hydrogen evolution reactions. *RSC Advances* **2018,** *8* (47), 26728-26754.

271. Feng, D.; Wang, K.; Wei, Z.; Chen, Y.-P.; Simon, C. M.; Arvapally, R. K.; Martin, R. L.; Bosch, M.; Liu, T.-F.; Fordham, S.; Yuan, D.; Omary, M. A.; Haranczyk, M.; Smit, B.; Zhou, H.-C., Kinetically tuned dimensional augmentation as a versatile synthetic route towards robust metal–organic frameworks. *Nature Communications* **2014,** *5*, 5723.

272. Dhakshinamoorthy, A.; Alvaro, M.; Chevreau, H.; Horcajada, P.; Devic, T.; Serre, C.; Garcia, H., Iron(iii) metal–organic frameworks as solid Lewis acids for the isomerization of α-pinene oxide. *Catalysis Science & Technology* **2012,** *2* (2), 324-330.

273. Tang, J.-J.; Liu, B., Reactivity of the Fe2O3(0001) Surface for Methane Oxidation: A GGA + U Study. *The Journal of Physical Chemistry C* **2016,** *120* (12), 6642-6650.

274. Munoz, M.; de Pedro, Z. M.; Casas, J. A.; Rodriguez, J. J., Preparation of magnetite-based catalysts and their application in heterogeneous Fenton oxidation – A review. *Applied Catalysis B: Environmental* **2015,** *176-177*, 249-265.

275. Fang, Y.; Banerjee, S.; Joseph, E. A.; Day, G. S.; Bosch, M.; Li, J.; Wang, Q.; Drake, H.; Ozdemir, O. K.; Ornstein, J. M.; Wang, Y.; Lu, T.-B.; Zhou, H.-C., Incorporating Heavy Alkanes in Metal–Organic Frameworks for Optimizing Adsorbed Natural Gas Capacity. *Chemistry – A European Journal* **2018,** *24* (64), 16977-16982.

276. Barton, D.; Hodgett, M.; Skirving, P.; Whelton, M.; Winter, K.; Vardy, C., The thermal decomposition of azobenzene. *Canadian Journal of Chemistry* **1983,** *61* (8), 1712-1718.

277. Toby, B. H.; Von Dreele, R. B., GSAS-II: the genesis of a modern open-source all purpose crystallography software package. *Journal of Applied Crystallography* **2013,** *46* (2), 544-549.

278. Okudera, H., Single crystal X-ray studies of cation-deficient magnetite. In *Zeitschrift für Kristallographie - Crystalline Materials*, 1997; Vol. 212, p 458.

279. Neuefeind, J.; Feygenson, M.; Carruth, J.; Hoffmann, R.; Chipley, K. K., The Nanoscale Ordered MAterials Diffractometer NOMAD at the Spallation Neutron Source SNS. *Nuclear Instruments and Methods in Physics Research Section B: Beam Interactions with Materials and Atoms* **2012,** *287*, 68-75.

280. Farrow, C. L.; Juhas, P.; Liu, J. W.; Bryndin, D.; Božin, E. S.; Bloch, J.; Proffen, T.; Billinge, S. J. L., PDFfit2 and PDFgui: computer programs for studying nanostructure in crystals. *Journal of Physics: Condensed Matter* **2007,** *19* (33), 335219.

281. Frandsen, B. A.; Yang, X.; Billinge, S. J. L., Magnetic pair distribution function analysis of local magnetic correlations. *Acta Crystallographica Section A* **2014,** *70* (1), 3-11.

282. Frandsen, B. A.; Billinge, S. J. L., Magnetic structure determination from the magnetic pair distribution function (mPDF): ground state of MnO. *Acta Crystallographica Section A* **2015,** *71* (3), 325-334.

283. Juhas, P.; Farrow, C. L.; Yang, X.; Knox, K. R.; Billinge, S. J. L., Complex modeling: a strategy and software program for combining multiple information sources to solve ill posed structure and nanostructure inverse problems. *Acta Crystallographica Section A* **2015,** *71* (6), 562-568.

284. Hill, A. H.; Jiao, F.; Bruce, P. G.; Harrison, A.; Kockelmann, W.; Ritter, C., Neutron Diffraction Study of Mesoporous and Bulk Hematite, α-Fe2O3. *Chemistry of Materials* **2008,** *20* (15), 4891-4899.

285. Banerjee, S. K.; Moskowitz, B. M., Ferrimagnetic Properties of Magnetite. In *Magnetite Biomineralization and Magnetoreception in Organisms: A New Biomagnetism*, Kirschvink, J. L.; Jones, D. S.; MacFadden, B. J., Eds. Springer US: Boston, MA, 1985; pp 17-41.

286. Yang, L.; Xu, G.; Ban, J.; Zhang, L.; Xu, G.; Lv, Y.; Jia, D., Metal-organic framework-derived metal-free highly graphitized nitrogen-doped porous carbon with a hierarchical porous structure as an efficient and stable electrocatalyst for oxygen reduction reaction. *Journal of Colloid and Interface Science* **2019,** *535*, 415-424.

287. Petkov, V.; Ren, Y.; Kabekkodu, S.; Murphy, D., Atomic pair distribution functions analysis of disordered low-Z materials. *Physical Chemistry Chemical Physics* **2013,** *15* (22), 8544-8554.

288. Kodama, K.; Iikubo, S.; Taguchi, T.; Shamoto, S.-i., Finite size effects of nanoparticles on the atomic pair distribution functions. *Acta Crystallographica Section A* **2006,** *62* (6), 444-453.

289. Trucano, P.; Chen, R., Structure of graphite by neutron diffraction. *Nature* **1975,** *258* (5531), 136-137.

290. Wu, H. B.; Wei, S.; Zhang, L.; Xu, R.; Hng, H. H.; Lou, X. W., Embedding Sulfur in MOF-Derived Microporous Carbon Polyhedrons for Lithium–Sulfur Batteries. *Chemistry – A European Journal* **2013,** *19* (33), 10804-10808.

291. Chapter 3 The method of total scattering and atomic pair distribution function analysis. In *Pergamon Materials Series*, Egami, T.; Billinge, S. J. L., Eds. Pergamon: 2003; Vol. 7, pp 55-99.

292. Walters, J. K.; Rigden, J. S.; Newport, R. J.; Parker, S. F.; Howells, W. S., The effect of temperature on the structure of amorphous hydrogenated carbon. *Physica Scripta* **1995,** *T57*, 142-145.

293. Rosi, N. L.; Kim, J.; Eddaoudi, M.; Chen, B.; O'Keeffe, M.; Yaghi, O. M., Rod Packings and Metal−Organic Frameworks Constructed from Rod-Shaped Secondary Building Units. *Journal of the American Chemical Society* **2005,** *127* (5), 1504-1518.

294. Grant Glover, T.; Peterson, G. W.; Schindler, B. J.; Britt, D.; Yaghi, O., MOF-74 building unit has a direct impact on toxic gas adsorption. *Chemical Engineering Science* **2011,** *66* (2), 163-170.

295. Wang, D.; Guo, Y.; Liang, K.; Tao, K., Crystal structure of zirconia by Rietveld refinement. *Science in China Series A: Mathematics* **1999,** *42* (1), 80.

296. Zavodinsky, V. G.; Chibisov, A. N., Stability of cubic zirconia and of stoichiometric zirconia nanoparticles. *Physics of the Solid State* **2006,** *48* (2), 363-368.

297. Tsunekawa, S.; Ito, S.; Kawazoe, Y.; Wang, J. T., Critical Size of the Phase Transition from Cubic to Tetragonal in Pure Zirconia Nanoparticles. *Nano Letters* **2003,** *3* (7), 871-875.

298. Kickelbick, G.; Schubert, U., Oxozirconium Methacrylate Clusters: Zr6(OH)4O4(OMc)12 and Zr4O2(OMc)12 (OMc = Methacrylate). *Chemische Berichte* **1997,** *130* (4), 473-478.

299. Guillerm, V.; Gross, S.; Serre, C.; Devic, T.; Bauer, M.; Férey, G., A zirconium methacrylate oxocluster as precursor for the low-temperature synthesis of porous zirconium(iv) dicarboxylates. *Chemical Communications* **2010,** *46* (5), 767-769.

300. Abrahams, S. C.; Bernstein, J. L., Remeasurement of the structure of hexagonal ZnO. *Acta Crystallographica Section B* **1969,** *25* (7), 1233-1236.

301. Roy, T. K.; Bhowmick, D.; Sanyal, D.; Chakrabarti, A., Sintering studies of nano-crystalline zinc oxide. *Ceramics International* **2008,** *34* (1), 81-87.

302. German, R. M., Sintering. In *Encyclopedia of Materials: Science and Technology*, Buschow, K. H. J.; Cahn, R. W.; Flemings, M. C.; Ilschner, B.; Kramer, E. J.; Mahajan, S.; Veyssière, P., Eds. Elsevier: Oxford, 2001; pp 8641-8643.

303. Yang, Q.; Wiersum, A. D.; Jobic, H.; Guillerm, V.; Serre, C.; Llewellyn, P. L.; Maurin, G., Understanding the Thermodynamic and Kinetic Behavior of the CO2/CH4 Gas Mixture within the Porous Zirconium Terephthalate UiO-66(Zr): A Joint Experimental and Modeling Approach. *The Journal of Physical Chemistry C* **2011,** *115* (28), 13768-13774.

304. Barrett, E. P.; Joyner, L. G.; Halenda, P. P., The Determination of Pore Volume and Area Distributions in Porous Substances. I. Computations from Nitrogen Isotherms. *Journal of the American Chemical Society* **1951,** *73* (1), 373-380.

305. Yuan, S.; Feng, L.; Wang, K.; Pang, J.; Bosch, M.; Lollar, C.; Sun, Y.; Qin, J.; Yang, X.; Zhang, P.; Wang, Q.; Zou, L.; Zhang, Y.; Zhang, L.; Fang, Y.; Li, J.; Zhou, H.-C., Stable Metal–Organic Frameworks: Design, Synthesis, and Applications. *Advanced Materials* **2018,** *30* (37), 1704303.

306. Gupta, A.; Dhakate, S. R.; Pal, P.; Dey, A.; Iyer, P. K.; Singh, D. K., Effect of graphitization temperature on structure and electrical conductivity of poly-acrylonitrile based carbon fibers. *Diamond and Related Materials* **2017,** *78*, 31-38.